Investigation of the Three-Dimensional Structure of a Rotating Magnetic Field Driven Field-Reversed Configuration using Internal Magnetic Field Measurements

Katherine M. Velas

A dissertation
submitted in partial fulfillment of the
requirements for the degree of

Doctor of Philosophy

University of Washington
2013

Reading Committee:
Richard Milroy, Chair
Alan Hoffman
Uri Shumlak

Program Authorized to Offer Degree:
Aeronautics and Astronautics

University of Washington

Abstract

Investigation of the Three-Dimensional Structure of a Rotating Magnetic Field Driven Field-Reversed Configuration using Internal Magnetic Field Measurements

Katherine M. Velas

Chair of the Supervisory Committee:
Professor Richard D. Milroy
Aeronautics and Astronautics

The Translation, Confinement, Sustainment Upgrade device (TCSU) used a rotating magnetic field (RMF) to form and sustain plasma in a field-reversed configuration (FRC). The physics of RMF current drive can be modeled in terms of the torque acting on the FRC. A fully translatable three-axis internal magnetic probe was built and used to generate a full r-z map of the magnetic field in the FRC and open field line region. Probe measurements are used to calculate the torques acting on the FRC formed using even-parity and odd-parity RMF antenna configurations. Odd-parity current drive was found to be more efficient and yields a plasma with lower resistivity than in even-parity current drive. An extrapolation method was developed to generate 3D magnetic field line plots which show that unlike in even-parity, field lines in odd-parity sustained FRCs make multiple transits of the FRC. Analysis using the three-axis probe data has greatly expanded our understanding of the physics of RMF driven FRCs.

TABLE OF CONTENTS

ACKNOWLEDGEMENTS

My deepest gratitude goes to my advisor Richard Milroy, who provided valuable insight and guidance in writing this thesis.

This work would not have been possible without the support of the entire RPPL staff who were always eager to share their knowledge and expertise. I thank Alan Hoffman for directing our research efforts; George Vlases, Bob Brooks, and Loren Steinhauer for teaching me all that they could; Jim Grossnickle for helping me operate the machine; Ken Miller and Terry DeHart for designing much of the complicated probe system; Mike Dellinger, Jon Hayward, and Scott Kimball for their amazing ability to build or fix anything; Kiyong Lee, Paul Melnick, and Chris Deards for teaching me how to be a grad student; and Matthew Fishburn for replicating RPPL in my office, ensuring that I could continue my research after the lab shut down.

I would like to thank the DOE and the ARCS foundation for their financial support; without the generous donation to ARCS from Anne Simpson and Charlie Conner, I may not have made it to Seattle.

A huge thank you to Sandra Fan, Fay Shaw, Nicole Nichols, Julie Medero, and Karen Studarus for providing the daily encouragement I needed to make it to the end.

Finally, thank you to Robert Talamantez, for everything.

DEDICATION

To Joe, Laura, Sara, and Karen

Chapter 1: **INTRODUCTION**

Harnessing the power of thermonuclear fusion will provide a solution to the worlds ever-increasing electricity demands. Fusion is the process where two light atoms combine to form a single heavier atom. In the sun, fusion occurs in the core of gravitationally confined plasma. On earth, there are two main types of plasma confinement: inertial and magnetic confinement. Inertially confined plasmas start as a pellet of fuel. The pellet is hit with high-energy lasers that initiate a shockwave, which compresses the fuel to the point of ignition. Magnetic confinement fusion entails confining a volume of plasma with magnetic fields and externally heating it to the point of ignition.

Research at the Redmond Plasma Physics Laboratory (RPPL) focuses on a magnetic confinement geometry called the Field Reversed Configuration (FRC)[**1,2**]. An FRC is an elongated plasma ellipsoid with an azimuthal current that reverses the direction of an applied magnetic field. In the Translation, Confinement, and Sustainment Upgrade (TCSU)[**3**] experiment at RPPL, a rotating magnetic field (RMF) is used to drive the azimuthal current. The RMF forms and sustains the FRC.

The RMF current drive has previously been described using a 2D analytical torque model in conjunction with numerical simulations. However, the physics of RMF current drive is fully 3D and the 3D effects have not been well described using the previous analysis. A fully translatable three-axis probe was installed in TCSU to map the internal magnetic field. The work described in this thesis includes the construction and calibration of the magnetic diagnostics, machine operation for the three-axis probe mapping, 3D magnetic field visualization, calculation of the torque acting on the FRC, and an investigation of a slowly rotating structure on the inner field lines. The internal magnetic field data collected in scans of TCSU is used to gain insight into complicated 3D nature of RMF current drive in even-parity and odd-parity operation.

Section 1.1: The field reversed configuration

The FRC is a type of compact torus with a simple linear geometry and little or no toroidal field. The FRC geometry shown in *figure 1.1* is described using (r, θ, z) cylindrical coordinates where the poloidal field at the midplane is $B_z(r)$. A toroidal current, J_θ, forms the FRC by reversing the applied bias field B_o. The FRC of length l_s is bounded by a separatrix of radius r_s, which marks the last closed flux surface; it separates the closed field line plasma from the open field lines.

The FRC compresses the applied bias field B_o against a flux conserver of radius r_c resulting in a higher external magnetic field at the midplane given by B_e. A basic geometric property of the FRC is the ratio of the separatrix radius at the midplane to the flux conserver radius, denoted as $x_s=r_s/r_c$. Flux conservation says the initial flux, $\phi_o = \pi r_c^2 B_o$, is equal to the external flux, $\phi_e = \pi(r_c^2 - r_s^2)B_e$, giving $B_e = B_o/(1 - x_s^2)$. There exists a field null at the midplane where $B_z(R) = 0$ given by $R = r_s/\sqrt{2}$.

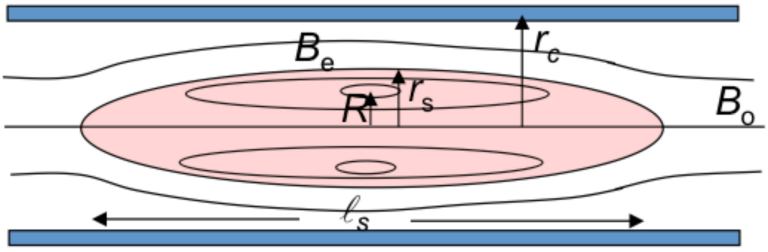

Figure 1.1: Schematic of FRC

The external magnetic field provides the confinement field for the plasma pressure. Assuming the FRC is elongated so that the magnetic field lines are straight at the midplane, we can write the ratio of the average plasma pressure to the magnetic field energy density as

$$\langle \beta \rangle \equiv \frac{\langle p \rangle}{B_e^2/2\mu_o} = 1 - \frac{x_s^2}{2}. \qquad (1.1)$$

The average β condition given in *equation 1.1* is a measure of the efficiency of the applied magnetic field at confining the plasma pressure.

Section 1.2: Rotating magnetic field current drive

Experiments with RMF were first proposed by Blevin and Thonemann 50 years ago[**4**]. Extensive RMF current drive experiments were performed by Ieuan Jones's group on the Flinders Rotamak[**5**].

The rotating magnetic field is a transverse field produced by two sets of antenna loops, as shown in *figure 1.2*. Each set is driven at a frequency ω with a phase different of 90^{o}. The resulting rotating magnetic field can be written as

$$B_{RMF} = B_{\omega}\cos(\omega t - \theta)\hat{\mathbf{e}}_r + B_{\omega}\sin(\omega t - \theta)\hat{\mathbf{e}}_{\theta} \qquad (1.2)$$

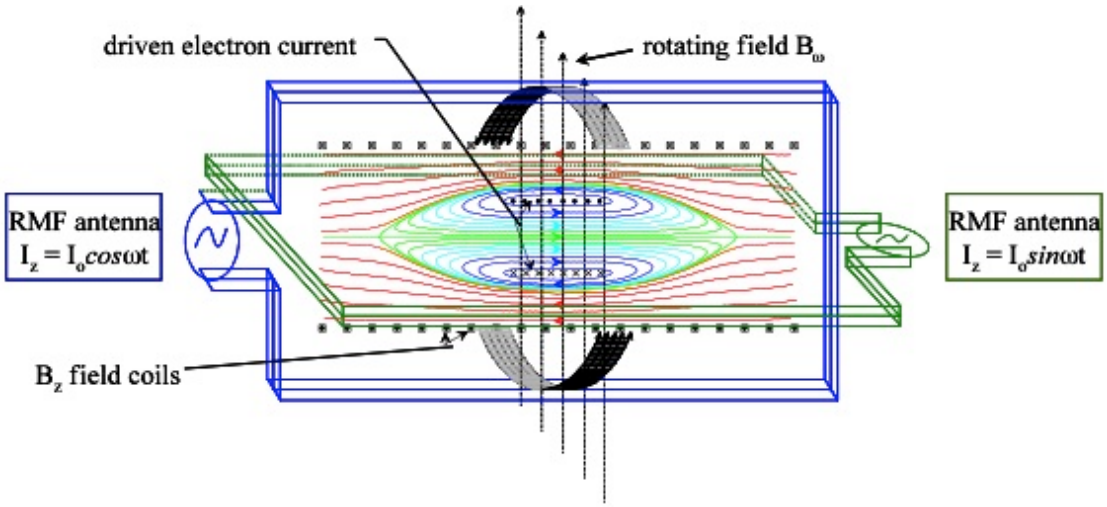

Figure 1.2: Schematic of the Rotating Magnetic Field

A simplified picture of RMF current drive has the electrons magnetized to the transverse field so they rotate synchronously with the RMF and create the azimuthal current that reverses the applied bias magnetic field. The RMF is operated such that $\omega_{ci} < \omega << \omega_{ce}$, where ω_c is the cyclotron frequency in the transverse field. The RMF rotates too fast for the ions to respond so they remain stationary but slow enough for the rotating field to act on the electrons. The RMF penetrates the plasma column by driving the electrons near the separatrix into near synchronous rotation.

The RMF antennas can have two different configurations. Even-parity has the transverse field in the same direction on either side of the z=0 midplane. In odd-parity the sign of the transverse field flips across the midplane. In either case, the transverse field

rotates in the positive theta direction. A schematic of one half of the RMF antenna is shown in *figure 1.3*. In the odd-parity configuration, the straps around the midplane create a component of the RMF field in the axial direction. In the case of even-parity, the current in the straps cancels and the field is transverse at the midplane. It has been theorized**[6]** that the odd-parity configuration could maintain closed field lines and increase electron confinement. However, prior to the work done on TCSU, the odd-parity configuration had not been well studied experimentally. Details of the RMF current drive process and the theory behind odd-parity drive are presented in *chapter 2*.

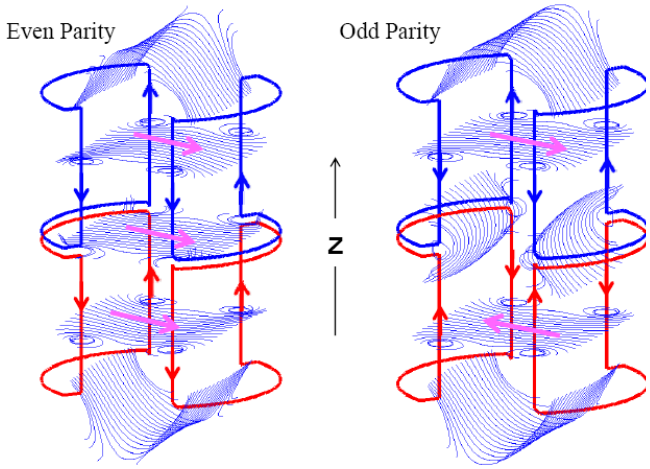

Figure 1.3: Schematic of one half of the RMF antenna showing the magnetic field

Section 1.3: Translation, Confinement, Sustainment—Upgrade Device.

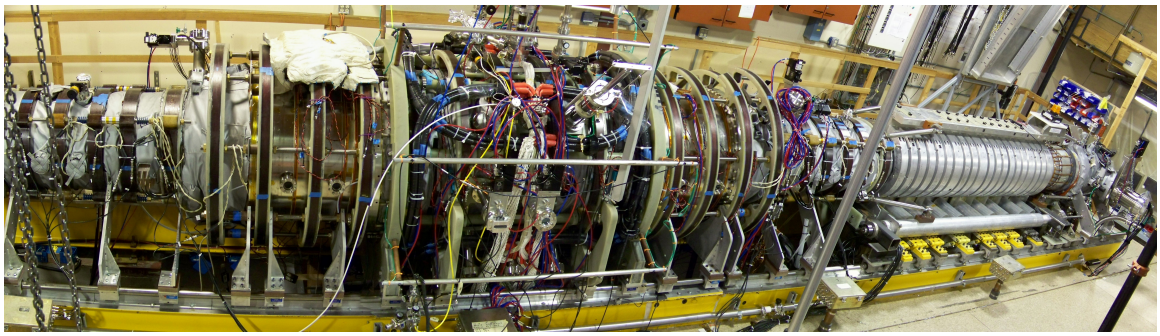

Figure 1.4: Photo of TCSU showing axial magnets

The TCSU device, shown in *figure 1.4*, is divided into two main sections: a central confinement section and a source section. The source section at the south end (at

right in photo) allowed for traditional θ-pinch FRC formation and translation into the main chamber; the θ-pinch source was not used in TCSU experiments and will not be discussed further. Instead, FRCs were formed by the RMF in the quartz confinement chamber. A scale schematic of the 10 m long machine is shown in *figure 1.5*. The central confinement section consists of a 1.25 m long, 0.8 m inner diameter (ID) quartz tube connected to a 0.62 m long 0.8 m ID stainless steel tube at each end. Each stainless steel section is connected to a 48 cm ID stainless tube via conical transition sections. A plasma gun at the north end of the machine (left side of *figure 1.5*) was used to initiate gas ionization.

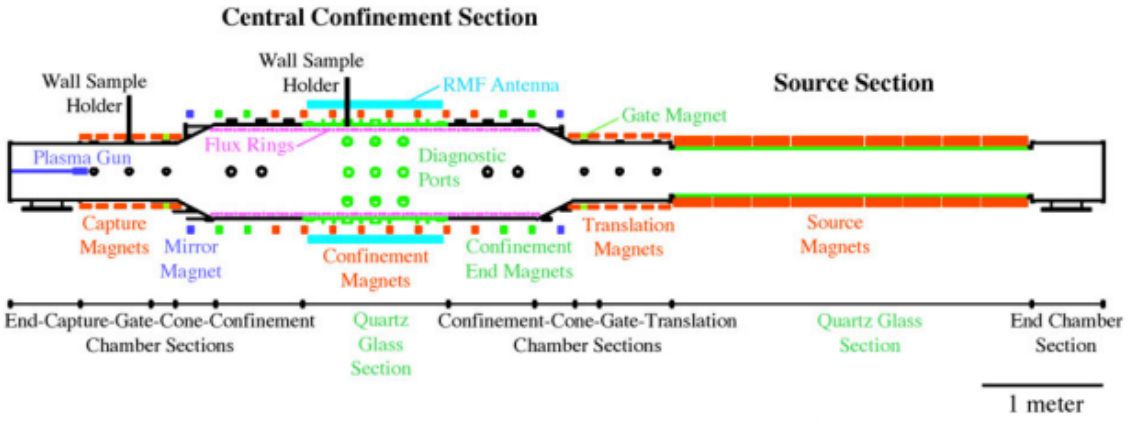

Figure 1.5: Drawing of TCSU showing axial magnets and diagnostic ports

Multi-turn magnetic field coils are arranged over the confinement section, as seen in *figure 1.6*. The first type in the 0.48 m ID end sections each have 6 60-turn 0.54 m ID copper coils. Each set of 6 coils is wired as two parallel sets of three magnets in series. These were referred to as 'end-north' (EN) or 'end-south' (ES) and were powered by the same capacitor bank called 'end-north-south-power' (ENSP). To create a strike zone for the exhaust plasma, the outer three magnets were wired with opposite polarity, creating a cusp in the magnetic field in the middle of the six magnets. A tantalum shield was installed here to act as the plasma-facing surface.

The 0.8 m ID and cone sections are surrounded by 14 1.05 m ID, 40-turn copper coils placed approximately 24 cm apart. The 14 coils were divided into three regions that were each powered with separate capacitor banks. The 'confinement-middle' (CM) section is powered by the CMP capacitor bank and consists of the six magnets over the

quartz section. These are wired as three parallel sets of two magnets in series. The ‘confinement-end’ (CE) section, powered by the CEP bank, consists of the two magnets over the stainless steel closest to the quartz section. The two magnets of the ‘confinement-end-north’ are wired in series and placed in parallel with the two series magnets in the ‘confinement-end-south.’ The ‘confinement-cone’ (CC) section, powered by the CCP bank, consists of the outer-most magnets over the cone sections. Again, two sets of two magnets in series on the north and two magnets in series on the south side, are wired in parallel. The CE and CC magnets are used to form the mirror configuration and control the axial extent of the FRC.

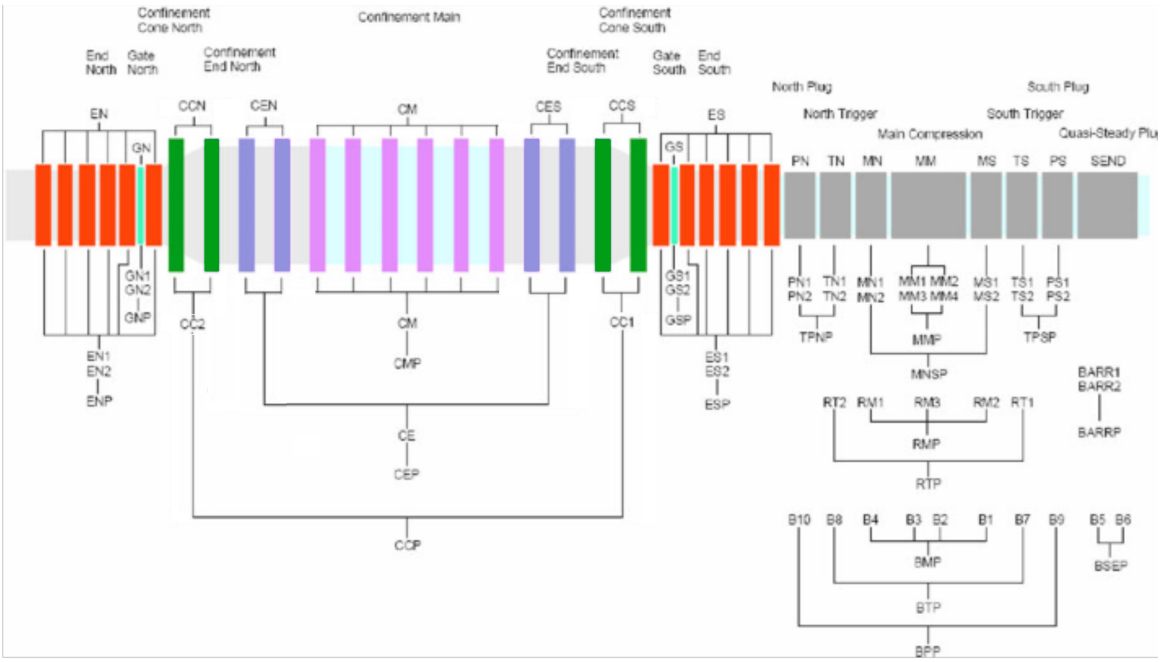

Figure 1.6: Schematic of axial magnetic field coils and power system naming convention

The wiring configuration described above was used for the majority of the experiments described in this paper. However, the magnets could be easily rewired to many different configurations.

A set of flux conserving rings was installed inside the confinement chamber to prevent the plasma from contacting the quartz or stainless steel wall. As plasma moves toward the wall a current is induced in each ring to resist the penetration of the magnetic field, pushing the plasma back toward the axis. Wall contact not only introduces

impurities into the plasma but is also destructive to the FRC; without a flux conserver, the FRC would expand radially until it made wall contact.

The set of 0.74 m ID internal rings spans the length of the 80 cm section of TCSU. Each ring was made from an 8 mm diameter aluminum rod coated with tantalum, which acts as the plasma facing surface. The rings are spaced 3 cm apart, center-to-center. The rings have an L/R time of about 7 ms (in vacuum), which is short enough for the external bias to penetrate but long enough that the rings act as a flux-conserving boundary and prevent the plasma from the hitting the wall. The rings were held in place with alumina spacers that created a trough at the bottom of the machine. The rings held three guides in place for three different magnetic probes. Within the trough were guides for two different probes; one for an axial magnetic probe array that measured the axial B_z just inside the rings, $B_i(z)$, at 29 locations and another for a translatable three-axis probe that measured $B_x(r)$, $B_y(r)$, and $B_z(r)$ at 30 radial locations. The three-axis probe guide ran down the center of the trough and the $B_i(z)$ was just off center. A second 29 loop axial array was located 30^o west, above the trough, and measured the B_z field just outside the rings, $B_o(z)$. The two axial B_z probes were necessary to determine the flux inside the rings and the excluded flux radius.

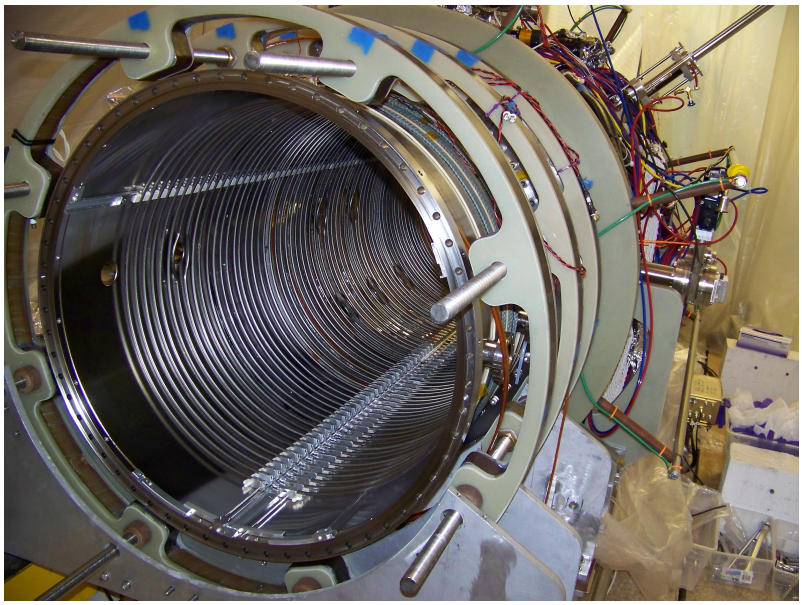

Figure 1.7: Photo of internal flux rings with trough at the base of the vacuum chamber

Section 1.4: Dissertation overview

The work detailed in this dissertation focuses on the magnetic diagnostics used to measure the 3D magnetic field structure in an RMF driven FRC which greatly increases our understanding of the physics of RMF current drive. While a variety of FRC parameters such as temperature and pressure can be measured using external diagnostics, the details of RMF penetration are available only by measuring the internal magnetic field structure. The translatable three-axis probe is used in conjunction with other diagnostics to analyze the internal structure of FRCs formed using even- and odd-parity RMF current drive. The three-axis probe measurements allow for the calculation of the end-shorting torque and the applied RMF torque as a function of axial position. For the first time, an r-z map of the magnetic field associated with an RMF-driven FRC and its jet has been made. The rest of this paper documents the mapping process and describes the implications of the measurements. The field line structure is twisted by the RMF which opens closed flux surfaces. Odd-parity operation allows for longer field lines and achieves the same plasma parameters using less applied torque implying a lower resistivity than in the even-parity configuration. Chapter 2 offers an overview of the analytical torque model used to describe RMF current drive as well as an introduction to the shorting effect and an overview of NIMROD simulations done for TCSU parameters. Chapter 3 covers the construction of the magnetic diagnostics. Chapter 4 details the magnetic probe calibration procedure. Chapter 5 compares the data taken in even- and odd-parity and summarizes the plasma parameters. Chapter 6 describes the process used to take the three-axis probe data and create three-dimensional field line maps of the even- and odd-parity driven FRCs. Chapter 7 presents data related to an internal structure rotating slower than the RMF. Chapter 8 will present a 3D model of the torque applied by the RMF and other sources of torque that balance the RMF torque. The three-axis probe measurements are used to calculate the torque and estimate an average resistivity for even- and odd-parity RMF drive.

Chapter 2: **PHYSICS BACKGROUND**

The history of RMF current drive begins in 1962 when Belvin and Thonemann[**4**] proposed a method to drive azimuthal electron current using a rotating transverse magnetic field. They solved Ohm's law, $E = \eta j + (j \times B)/ne$, for the hall current by neglecting the resistive term because the RMF drive is governed by the jxB term. The theoretical framework they developed has been expanded with further theoretical work.

Jones and Hugrass[**7**] assumed the hall term was small compared to the resistive term and found a solution with a partially penetrated RMF. The RMF penetrates the plasma column by driving the electrons near the separatrix into near synchronous rotation such that the electron rotation frequency equals the RMF rotation frequency ($\omega_e \approx \omega$). In 1986 Hugrass[**8**] considered the effects of realistic antenna geometries and found that higher spatial harmonics degrade the current drive efficiency. Further analysis by Watterson in 1991 showed that the RMF opens the normally closed field lines of an FRC [**9**]**.** These models lead to the development of an analytical model of RMF current drive in an FRC equilibrium by Hoffman in 2000[**10**]. This model has been used to describe the FRCs formed in the TCSU device and provides scaling laws for RMF driven FRCs.

Section 2.1: Analytical model for RMF current drive

Hoffman's analytical model describes the buildup of poloidal flux in terms of the torque applied to the bulk plasma column by the RMF and balanced by the torque due to electron-ion friction. This is a 2D model that assumes an infinitely long cylindrical plasma (no z-dependence), stationary ions, and rigid rotor azimuthal electron motion ($v_{e\theta} = \omega_e r$).

The poloidal flux, ϕ_p, in the FRC is defined by

$$\phi_p = -\int_0^R 2\pi r B_z dr \qquad (2.1)$$

where R is the magnetic field null such that $R\sqrt{2} = r_s$ and B_z is negative inside the field null.

The change in poloidal flux is defined as by:

$$\frac{d\phi_p}{dt} = \int E_\theta \cdot dl \tag{2.2}$$

and requires E_θ at the field null to be greater than zero to grow the poloidal flux and E_θ equal to zero to sustain the poloidal flux in steady state. This analysis is concerned with the steady state equilibrium so E_θ is zero everywhere. To model the steady state behavior of the FRC we need an expression for E_θ in terms of FRC quantities.

Starting from generalized Ohm's law,

$$E + v \times B = \eta j + \frac{1}{ne}\left(j \times B - \nabla p_e\right) \tag{2.3}$$

where E is the electric field, v is the ion velocity, B is the magnetic field, η is the resistivity, j is the plasma current, n is the density, e is the electric charge, and p_e is the electron pressure. First, apply our assumption of stationary ions and rearrange the terms to write an equation for the electric field

$$E = \eta j_e - v_e \times B - \frac{1}{ne}\nabla p_e, \tag{2.4}$$

where j_e and v_e are the electron current and electron velocity, respectively.

For the RMF driven cylindrical plasma, we assume the pressure gradient is only in the radial direction so the expression for E_θ becomes

$$E_\theta = \eta_\perp j_{e\theta} + \left\langle -v_{ez} B_r \right\rangle + v_{er} B_z \tag{2.5}$$

where the term in brackets represents an a time-average over one RMF cycle,

$$\left\langle \ \right\rangle \equiv \frac{\omega}{2\pi}\frac{1}{2\pi}\int_{t=0}^{2\pi/\omega}\int_{\theta=0}^{2\pi} d\theta dt \tag{2.6}$$

The inward radial velocity contributes to the current drive on the inner field lines but this model concerns total torques on the bulk FRC. The $v_{er}B_z$ term is negative outside the field null and positive inside the field null so it has no net effect on the total torque balance. Ignoring the radial velocity term gives

$$E_\theta = \eta_\perp j_{e\theta} + \left\langle -v_{ez} B_r \right\rangle. \tag{2.7}$$

The second term on the right side of *equation 2.7* is the RMF drive term and is balanced by the resistive term. To rewrite *equation 2.7* as a torque balance, we multiply

by $en_e r$ and integrate over the FRC surface area. To perform the integration of E_θ we need a radial profile of E_θ. The profile used in *ref. [10]* is $E_\theta = (r/R)E_{\theta R}$ where $E_{\theta R}$ is the value of E_θ at the field null.

$$\int en_e r E_{\theta R}\left(\frac{r}{R}\right)dS = \int en_e r\eta_\perp j_\theta dS + \int en_e r\left\langle -v_{ez}B_r\right\rangle dS \tag{2.8}$$

$$\int en_e E_{\theta R}\left(\frac{r^2}{R}\right)dS = \int r\left\langle j_{ez}B_r\right\rangle dS - \int m_e n_e \nu_\perp v_{e\theta} r dS \tag{2.9}$$

The two terms on the right hand side of *equation 2.9* correspond to the RMF torque and the resistive torque, respectively.

The torque about the z-axis, T_θ, is given by:

$$T_\theta = \int rF_\theta dS = \int_0^a 2\pi r^2 F_\theta dr \tag{2.10}$$

where *a* is the radius of the plasma column, taken to be the separatrix radius r_s. The RMF exerts an azimuthal force on the electrons given by $F_\theta = \langle j_{ez}B_r\rangle$. The resistive force is due to the electron-ion collisions is given by $F_\theta = m_e n_e \nu_\perp v_{e\theta}$.

Integrating *equation 2.9* gives an expression of the electric field at the field null ($E_{\theta R}$) in terms of the torques per unit length.

$$\frac{\pi}{\sqrt{2}} en_e r_s^3 E_{\theta R} = T'_{RMF} - T'_\eta \tag{2.11}$$

substituting *equation 2.11* into *equation 2.2* yields an expression for the change in poloidal flux in terms of the torque per unit length.

$$\frac{d\phi_p}{dt} = 2\pi R E_{\theta R} = \frac{2}{en_e r_s^2}\left(T'_{RMF} - T'_\eta\right) \tag{2.12}$$

In steady state, the RMF torque is balanced by the resistive torque. With equations for T_{RMF} and T_η we can derive expressions to calculate FRC scaling laws.

The expressions for the torque in terms of the magnetic field and measured plasma parameters are based on the analytical RMF penetration solutions obtained by Hugrass[**8**] and modified by Hoffman[**10**] for the rigid rotor assumption of a fixed electron rotational speed throughout the plasma column.

Using the vector potential we can write $E = -\frac{\partial A}{\partial t}$, $B_r = \frac{1}{r}\frac{\partial A_z}{\partial \theta}$, $B_\theta = -\frac{\partial A_z}{\partial r}$, meaning the current can be expressed as, $j_z = -\frac{1}{\mu_o}\nabla^2 A_z$

Using *equation 2.4* we can write the axial electric field as

$$E_z = \eta_{\|} j_z + v_{e\theta} B_r \tag{2.13}$$

where $\eta_{\|}$ is the parallel resistivity. Using B, E, and j, in terms of the vector potential, the equation for E_z above can be expressed as a 2nd order differential equation whose solutions take the form of modified Bessel functions. The expression for the RMF force, F_θ can then be written as

$$F_\theta = \frac{2B_\omega^2}{\mu_o r}\left|\frac{I_1(\sqrt{i}kr)}{I_0(\sqrt{i}ka)}\right|^2 \tag{2.14}$$

where I_1 and I_0 are the modified Bessel functions and k is a factor related to the penetration depth of the RMF. Using *equation 2.14*, torque per unit length can be written:

$$T'_{RMF} = \int_0^{r_s} 2\pi r^2 F_\theta dr = \frac{2\pi r_s^2 B_\omega^2}{\mu_o}\left(\frac{\sqrt{2}f(ka)}{ka}\right) \tag{2.15}$$

The term in the parenthesis is based on the penetration depth of the RMF and is simplified in subsequent articles[**11**] as $f(\zeta)$.

$$T_{RMF} = \frac{2\pi r_s^2 B_\omega^2}{\mu_o}\ell_a f(\zeta) \tag{2.16}$$

ζ is defined as the ratio of the average electron rotation frequency, $\langle\omega_e\rangle$, to the RMF rotation frequency, ω , and is related to the penetration depth of the RMF. More specifically, ζ is the ratio of the actual FRC line current, given full field reversal, to the line current that would occur with synchronous electron rotation.

$$\zeta = \frac{I'_{line}}{I'_{sync}} = \frac{2B_e/\mu_o}{0.5\langle n_e\rangle e\omega r_s^2} = \frac{\langle\omega_e\rangle}{\omega} \tag{2.17}$$

In the original analysis, the $f(\zeta)$ term was taken to be δ^*/r_s where δ^* is penetration depth of the RMF. However, numerical calculations found that for $0.2 \le \zeta \le 0.9$, $f(\zeta) \approx 0.1$. The FRCs in TCSU typically have $\zeta = 0.4 - 0.7$.

To calculate the resistive torque, we include the assumption of a rigid rotor profile in the last term in *equation* 2.9,

$$T'_\eta = \int m_e n_e \nu_\perp v_{e\theta} r dS = \int_0^a 2\pi r^3 m_e n_e \nu_\perp dr = \frac{1}{2}\pi e^2 a^4 \left\langle n_e^2 \omega_e \eta_\perp \right\rangle \tag{2.18}$$

The assumption of rigid rotor electron motion also implies that the average electron density is approximately 70% of the peak density, $\langle n_e \rangle \approx 0.7\ n_m$, and sets an approximation of the external magnetic field as $B_e = 0.27 \mu_o n_m e \omega_e r_s^2$. These substitutions allow us to estimate the resistive torque in terms of measurements made on TCSU. The total resistive torque depends on the length of the separatrix (l_s) and is calculated as:

$$T_\eta = 1.16\pi r_s^2 e n_m \ell_s \left(\frac{B_e}{\mu_o}\right)\left\langle \eta_\perp \right\rangle \tag{2.19}$$

Equating the RMF and resistive torques gives an expression for the ratio of the external magnetic field to the RMF field. Assuming uniform total temperature, $T_t = T_i + T_e$, and neglecting any ion rotational centrifugal effects, the external magnetic field is

$$B_e = \left(2\mu_o n_m k T_t\right)^{1/2} \tag{2.20}$$

The resistive torque in *equation 2.21* is terms of B_e^2 and can be compared to the RMF torque which varies as B_ω^2.

$$T_\eta = 1.16\pi r_s^2 \ell_s \left(\frac{\mu_o e^2 n_m}{2kT_t}\right)^{1/2}\left(\frac{B_e}{\mu_o}\right)^2 \left\langle \eta_\perp \right\rangle \tag{2.21}$$

Using *equation 2.21 and 2.16*, the ratio of B_e to B_ω is

$$\frac{B_e}{B_\omega} = 1.31\left(\frac{2\mu_o k T_t}{e^2 n_m}\right)^{1/4}\left(\frac{\ell_a f(\xi)}{\ell_s \left\langle \eta_\perp \right\rangle}\right)^{1/2} \tag{2.22}$$

Taking $l_s / l_a \approx 1.25$, and plugging in the values of the constants we can simplify the above expression as

$$\frac{B_e}{B_\omega} = 13.1\left(\frac{T_t(eV)}{n_m(10^{19} m^{-3})}\right)^{1/4}\left(\frac{1}{\left\langle \eta_\perp \right\rangle}\right)^{1/2} \tag{2.23}$$

Typical ratios for B_e/B_ω are around 4.5 for even-parity 122 kHz RMF and upward of 6.5 for 107 kHz odd-parity; B_ω represents the same factor of the antenna current in each case, B_ω (mT) = 0.5 I_{ant} (kA).

Using measurements to calculate B_e, B_ω , T_t, and n_m, we can calculate the average resistivity. Fundamentally, the plasma resistivity is a key parameter for determining the effectiveness of RMF current drive; it determines the plasma density that can be supported and the RMF power required to support the desired poloidal current.

The analytical model is developed for a 2D geometry assuming infinite RMF antennas but the actual RMF antenna geometry is almost square so there will be 3D effects on the RMF drive. However, the model provides scaling laws which form a framework to compare the 3D calculations made using the translatable probe data.

So far, the radial velocity has been neglected, however for the FRC to be in steady state, the azimuthal electric field must be zero everywhere. The RMF does not penetrate to the inner field lines so where the $<j_{ez}B_r>$ force falls to zero, there must be an inward radial flow that provides a $v_{er}B_z$ force to balance the resistive term in *equation 2.5* for E_θ. On the inner field lines, a positive $v_{er}B_z$ balances the negative $\eta_\perp j_\theta$. On the outer field lines, $v_{er}B_z$ is negative and the positive RMF term, $< v_{ez}B_r >$, must be large enough balance both negative terms ($\eta_\perp j_\theta$ and $v_{er}B_z$). The inward v_r implies the presence of a swirling flow. If we allow for ion motion, the necessary v_r can be supplied by either a fluid flow or an electron flow. Previous analysis[**12**] did not distinguish between the two types of swirling flow. An electron flow creates a steady toroidal field inside the FRC that flips sign across the midplane; this toroidal field was measured directly for the first time by the translatable three-axis probe. A schematic of the swirling flow is shown in *figure 2.1*

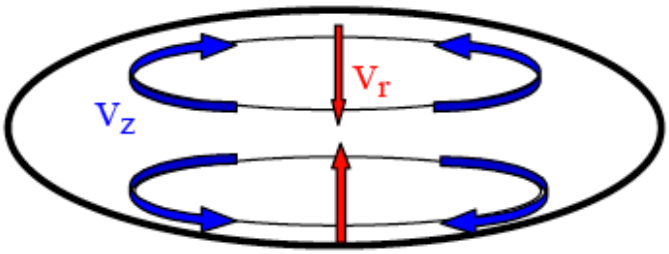

Figure 2.1: Swirling radial electron flow pattern

The existence of this swirling flow indicates important axial dependencies on the physics of the FRC. Axial variation in the electric and magnetic fields are important to the physics of the FRC.

Section 2.2: End-shorting effects

The analysis presented so far has assumed no axial variation, i.e. quantities are independent of z. However, the RMF antennas have a finite length and the plasma in the open field line region affects the behavior of the FRC. The open field lines terminate on a conducting boundary where the tangential electric field is forced to zero and line-tying occurs. In the central quartz section, the open field lines are free to rotate with the RMF and a portion of the RMF torque is spent twisting the open field lines. The torque generated in the open field line region is called the shorting torque. Detailed analysis of the physics at the shorting boundary was done by Steinhauer [**13**] using the two fluid equations and by Macnab et. al.[**14**] using Hall MHD. However, we are most interested in the details of RMF drive within the FRC volume.

The open field lines terminate on a tantalum shield in a cusp of the magnetic field forcing the tangential electric field (E_z) to zero. This sets up a condition where $\dot{B}_\theta = -(\nabla \times E)_\theta = \partial_r E_z - \partial_z E_r$ is large because $\partial_r E_z$ is large at the wall. A toroidal field develops on the open field lines, which creates a torque that acts on the FRC. This shorting torque is in the opposite direction as the RMF torque. Steinhauer[**13**] theorized that the shorting torque could prevent the ions from spinning up to the RMF frequency.

However, analysis performed by Deards[**15**] found that ion-neutral interactions primarily limit the ion spin-up in an RMF driven FRC.

The mechanism described above is independent of the RMF. However, the central section of TCSU is quartz and the axial field lines that are tied to the conducting boundary are free to rotate with the RMF at the midplane. A portion of the RMF torque is transmitted along the open field lines. The rotating field lines twist up to an equilibrium in the open field line region. The two effects are complementary. The electric field is difficult to measure but the shorting torque can be calculated using the three-axis probe in the Maxwell stress tensor analysis described in *chapter 8.*

Section 2.3: Odd-parity RMF

Studies of field line closure for FRC-like plasmas have found that the addition of a uniform transverse field (like the RMF) results in the opening of field lines[**11**,**16**]. However, the mean-field component remains closed. The ions experience this field line closure because the RMF is operated at a frequency such that $\omega_{ci} << \omega_{RMF}$. Because $\omega_{ce} > \omega_{RMF}$, the electrons see open field lines and quickly lose energy due to high parallel thermal conduction; this makes it difficult for the electrons to achieve high electron temperatures in an RMF driven FRC.

Odd-parity RMF current drive employs two separate sets of antennas with anti-parallel magnetic fields that rotate in the same direction. It has been shown numerically[**6**] that the odd-parity RMF allows for the possibility of closed field lines. Specifically, field line closure was observed in simulations where the RMF field B_ω was a small fraction of the external field B_e ($B_e/B_\omega \approx 20$).

Experiments on TCS[**17**] found that odd-parity drive yielded an improvement in confinement for $B_e/B_\omega \approx 4$. In the TCS device, the odd-parity antenna provided the same B_ω (scaled from the measured antenna current) and line integrated density but resulted in a larger external field (B_e)

Section 2.4: NIMROD simulations

RMF current drive in TCSU has been modeled using NIMROD[**18**], a 3D extended-MHD code. The physics of RMF current drive has been modeled using uniform plasma resistivity for both even- and odd-parity configurations[**19**]. The boundary conditions are specified by setting the tangential component of the electric field and normal component of the magnetic field on the boundary; this is done through an expression for the vector potential, which is a function of z and θ. More recently, the boundary conditions have been tailored to match the experimental boundary values measured by the three-axis probe[**20**]. The results from the NIMROD simulations show good qualitative agreement to experimental measurements. The TCSU data and NIMROD results have similar toroidal field structure inside the FRC. A comparison of the simulation and experimental boundary conditions and toroidal field profiles is presented in *section 5.5*. Additionally, the magnetic field lines drawn using simulation results show the same behavior as measured in the machine. The odd-parity field lines are much longer; this is described in detail in *sections 6.7* and *6.8*.

Chapter 3: **MAGNETIC PROBES**

Magnetic probes on TCSU provide information about the structure of the FRC. Magnetic probes[**21**] operate on Faraday's law, $V_{out} = Nd\Phi/dt = NAdB/dt$, where V_{out} is the voltage developed around a single turn of the probe, N is the number of turns in the probe, Φ is the flux through the probe winding, A is cross-sectional area of the probe winding, and B is the magnitude of the magnetic field. Flux penetrating the loop generates a loop voltage proportional to the change in flux. The signal from each winding is integrated to provide a direct measure of the magnetic field, $B = (1/NARC)\int V_{out}dt$, where R and C are the resistance and capacitance of the integrator circuit. The integrators used for the internal magnetic probes have a 10 μs RC time.

External magnetic diagnostics measure the magnetic field outside the separatrix and help determine the overall shape of the FRC. Flux loops wrapped around the outside of the wall at 24 axial locations measure the total magnetic flux passing through their cross-sectional area. Using local measurements of B_z we can determine the separatrix radius. The internal flux rings add a complication that is solved using two axial B_z measurements and is discussed in section 3.1.

There are two internal magnetic diagnostics that give radial magnetic field profiles. There is a two-axis probe (B_x and B_z) inserted from the top of the machine at the midplane that could be retracted to allow for wall-conditioning. A fully translatable three-axis probe sticks up into the plasma from the bottom of the machine; the probe can be positioned anywhere along the z-axis in the 80 cm diameter main chamber. Using the internal probes we measure radial profiles of the magnetic field and have data about the internal dynamics of the FRC which are not visible on the external magnetic diagnostics. The majority of other diagnostics on TCSU are located at the midplane and the translatability of the three-axis probe has given detailed information about the dynamics of the FRC along its entire length as well as providing new data on magnetic activity in the open field line region. The magnetic probes have very little noise pick-up, are non-perturbing, and designed to withstand TCSU parameters.

Section 3.1: Axial $B_z(z)$ probes

The separatrix radius is approximated by calculating the excluded flux radius (r_{xf}), which is the radius at which the poloidal flux in the FRC goes to zero. Recall that the FRC has zero net flux; the flux inside the field null is equal and opposite to the flux between the field null and the excluded flux radius. The excluded flux radius is equal to the separatrix radius in the absence of field line curvature and open field line pressure[**22**]. Deviations between the separatrix and excluded flux radii are most evident near the x-points where the separatrix radius is small. The excluded flux radius is easy to measure and gives the overall shape of the FRC. Prior to the installation of the internal flux conserving rings, flux conserving straps were wrapped around the vacuum chamber. The excluded flux radius was calculated from *equation 3.2* using a flux loop wrapped around the vacuum chamber and magnetic probes at the wall.

After the installation of the internal flux conserving rings, mentioned in section 1.3, two axial arrays of magnetic loops were installed in order to measure the flux at the rings and the excluded flux radius. *Figure 3.1* shows a machine drawing of the TCSU main chamber with the flux rings and the axial location of each probe winding. Both arrays consist of 29 windings, each 6 cm long, placed 9 cm apart center-to-center. Current running through a flux ring creates a small, local magnetic field. The rings are spaced 3 cm apart so the axial probe windings span the length of two rings with overlap on either side to cancel the local field effects. Winding #15 is at the midplane; winding #01 is at the south end of the machine at z = -126 cm and winding #29 is its symmetric pair at z = +126 cm. The probes are electrostatically shielded with gold-plated Kapton and a grounded drain wire. Additional layers of Kapton, approximately 3 mils thick, provide high voltage insulation. Each probe is placed in a stainless steel tube that forms the vacuum boundary. An outer quartz tube insulates the stainless steel from the plasma. As described in section 1.3, the two probes are at the same radial location, shown in *figure 3.2* (left). The internal flux rings are secured in a trough sitting on the bottom of the machine. The B-field Main Inner (BMI) probe is placed within the trough to measure $B_i(z)$, the magnetic field internal to the rings. The B-Field Main Outer (BMO) probe is 30 degrees off the bottom and measures $B_o(z)$, the field outside the rings. The trough extends

the rings to a larger radius at the bottom of the machine, ensuring the magnetic measurements are made at the same radial location of r = 38.5 cm. A close up of the rings, trough, and probe housings is shown in *figure 3.2* (right).

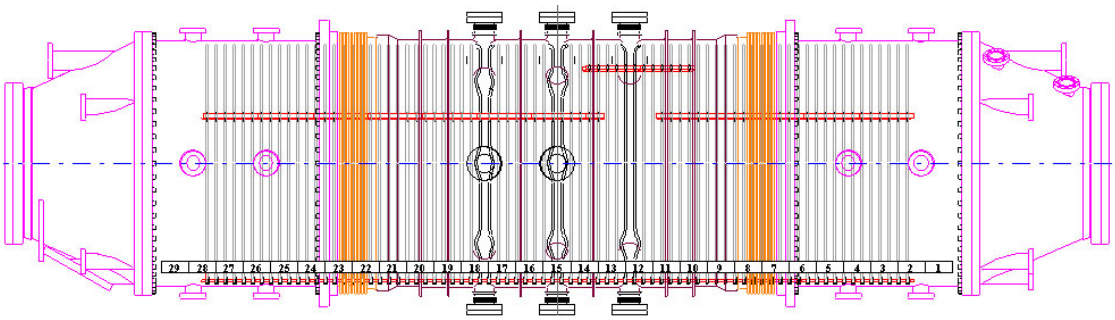

Figure 3.1: Drawing of main chamber showing internal flux rings as gray lines with numbers indicating the position of the axial B_z loops.

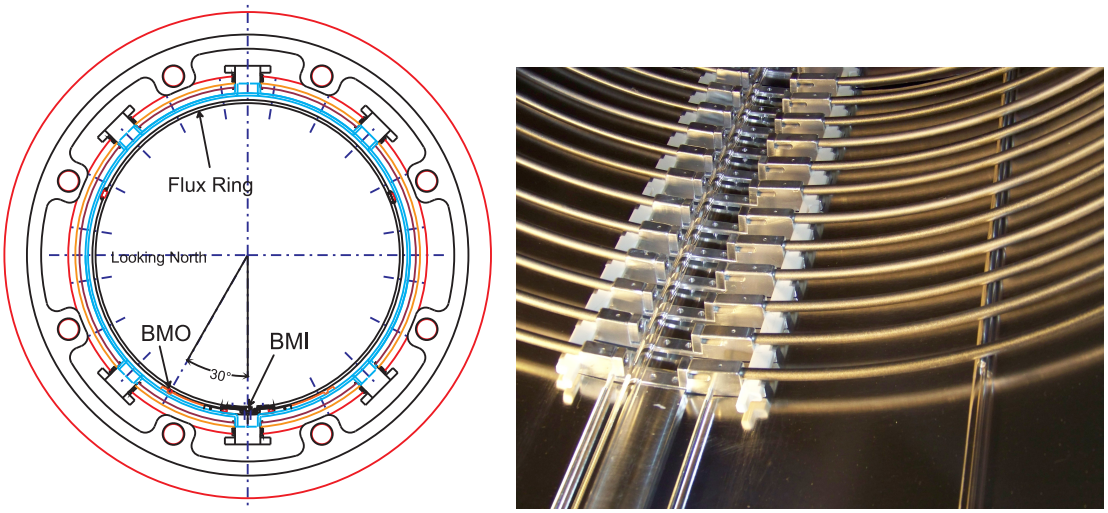

**Figure 3.2: Left) Drawing showing location of axial magnetic probes.
Right) Close up photo of trough with guides for axial magnetic probes.**

The BMI & BMO diagnostics are primarily used to calculate the excluded flux radius at the location of each loop. The external flux loops measure the flux outside the wall of TCSU. The 24 flux loops are extrapolated to the 29 locations of the axial loops. The flux at the ring is calculated by subtracting the flux between the rings and the outer flux loops from the external flux measurement, as given by *equation 3.1*:

$$\Phi_{ring} = \Phi_{external} - B_o \pi \left(r_{fluxloop}^2 - r_{probe}^2 \right). \qquad (3.1)$$

The flux on the internal rings is also given by *equation 3.2*, which gives the magnetic flux between the rings and the FRC

$$\Phi_{ring} = B_i \pi \left(r_{probe}^2 - r_{xf}^2 \right) \tag{3.2}$$

where r_{xf} is the excluded flux radius. Equating equations 3.1 and 3.2 and solving for r_{xf} allows us to calculate the excluded flux radius as a function of axial position to see the overall shape of the FRC as it evolves in time.

Section 3.2: Internal magnetic probes

TCSU has two magnetic probes that are inserted into the plasma and are used to characterize the internal dynamics of the FRC. A two-axis array is inserted at the midplane and a three-axis array is inserted at the north cone and is translatable along the length of the 80 cm chamber.

The Midplane Internal B Probe (MIBP) has 24 winding locations spaced 2 cm apart. At each location from y = 40 cm to -6 cm there are two orthogonal windings oriented to measure B_x and B_z. The three-axis probe has 30 winding locations spaced 1.5 cm apart and spanning from y = 6.5cm to -37 cm. Each position has three orthogonal windings measuring B_x, B_y, and B_z. A photo of one winding triplet is shown in *figure 3.3*. This probe is oriented such that loops in the z-direction measure B_z, loops in the x-direction measure B_θ, and loops in the y-direction measure B_r.

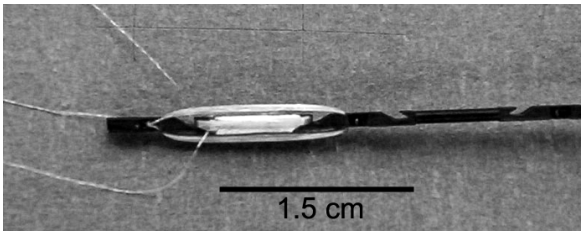

Figure 3.3: One group of windings from the three-axis internal probe

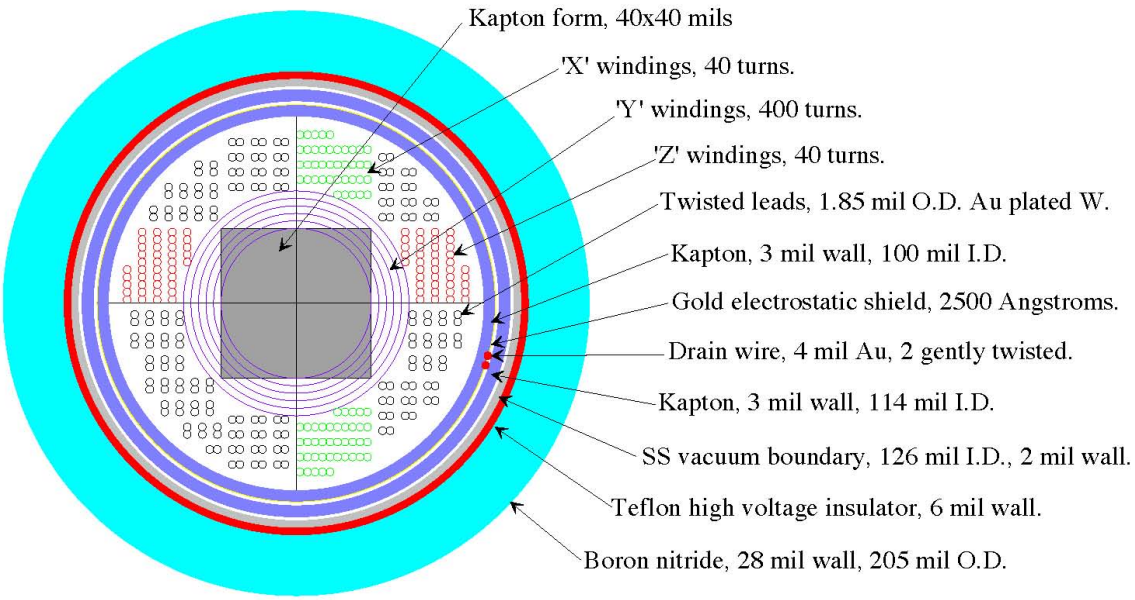

Figure 3.4: Cross-section of internal probe construction

The two probes have the same basic construction[**23**], detailed in *figure 3.4*. Notches are cut in a Kapton form to provide a guide for winding the 2 mil gold-plated tungsten wire. B_x and B_z loops have 40 turns, B_y has 400, yielding a total area of approximately 7, 4.5, and 2 cm^2, respectively. The windings and twisted leads are covered with a gold plated Kapton tube that provides electrostatic shielding. A bare Kapton tube holds the drain wire onto the gold plating and the probe is inserted into a thin-walled stainless steel tube, which acts as the vacuum boundary. Prior to probe insertion, the thin-walled tube is covered in Teflon heat shrink, which provides 22 kV of voltage holdoff. A final sheath of boron nitride acts as the plasma-facing surface and provides additional insulation. The boron nitride has a 5 mm outer diameter. Probe construction ensures good frequency response up to 5 MHz.

The probes were built to withstand TCSU plasma pulses of 3 ms with plasma densities around 10^{19} m^{-3} up to approximately 300 eV. Total temperature in TCSU is typically 50-100 eV. The probes are non-perturbing; external diagnostics show no change in plasma parameters with or without the probes inserted.

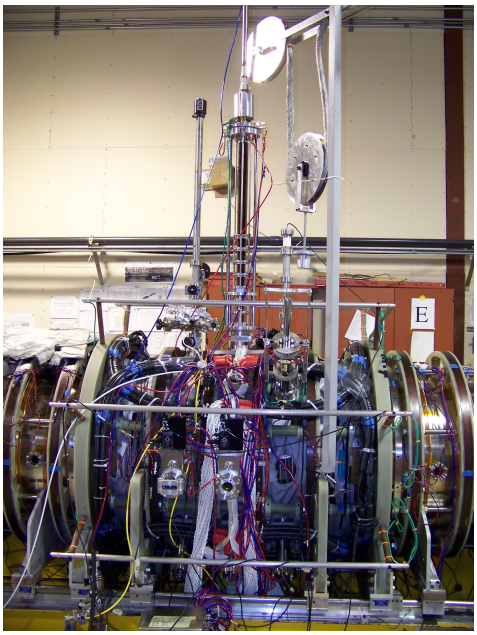

Figure 3.5: Photo of two-axis probe bellows installed at the midplane

MIBP is inserted transversely at the midplane from the top of TCSU, shown in *figure 3.5.* It is in a bellows housing and can be retracted for glow discharge cleaning or Ti-gettering. In this vertical orientation the B_x loops measure $-B_\theta$ and are primarily used to look at the RMF field penetration.

The three-axis probe is installed through an approximately 14 ft long bellows setup that allows translation within the 80 cm section of TCSU from z = -132 cm to +138 cm. A machine drawing of the fully contracted bellows is shown in *figure 3.6.*

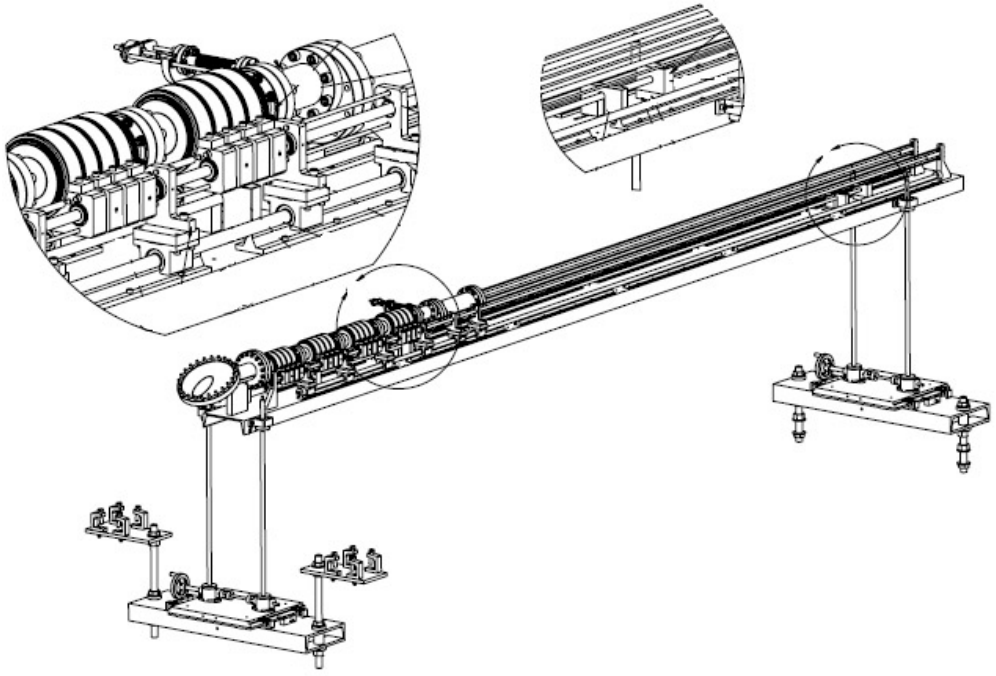

Figure 3.6: Machine drawing of three-axis probe bellows fully contracted

The 12-inch flange on the end attaches to a port on the north cone section of TCSU. The gold plated tungsten probe wires are soldered on to approximately 13-foot long 5 mil copper wires that are soldered onto standard RJ45 connectors. The high resistance of the tungsten wire would cause a large attenuation of the signal if kept to the length necessary to reach the connector block. The wire leads are wrapped with Teflon tape for additional insulation and a 5 mil tungsten wire is included for structural support; this was necessary to ensure smooth insertion into the stainless steel vacuum boundary. The vacuum boundary consists of three sections; a 19 inch thin wall stainless tube, which covers the probe stalk, is brazed onto a short copper tube that is brazed to a thicker stainless tube with ¼" inner diameter. The copper section was installed to have a soft metal that would bend smoothly. A 90-degree bend was made at the base of the thin walled stainless tube so the probe would measure a radial stick up into the chamber. A close-up of the insulated bend is shown in *figure 3.7* (left). To provide insulation, a quartz tube covers the long stainless steel tube and the copper section. The quartz tube rides along the bottom of the machine, in the same trough where BMI resides. A photo of the entire setup is shown in *figure 3.7* (right); the connector box is at the left in the foreground and the probe stalk can be seen under TCSU in the background.

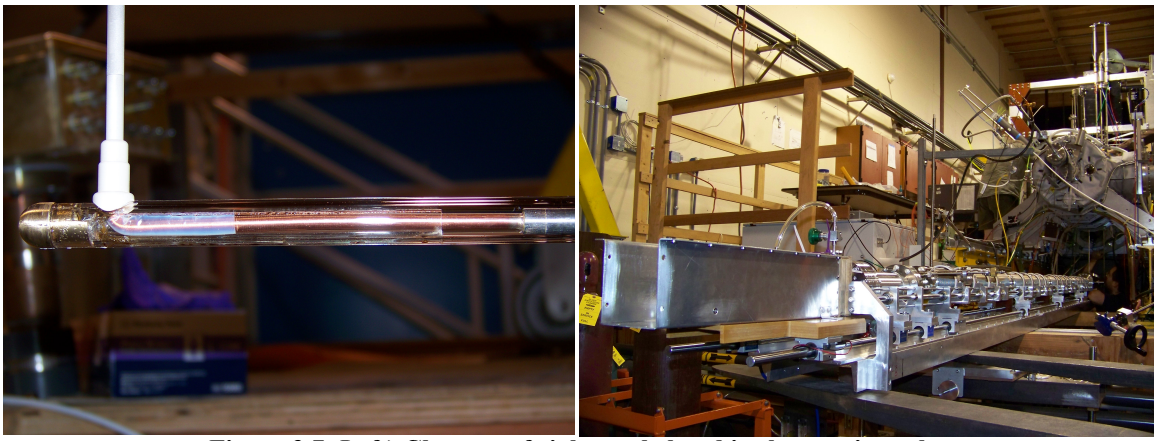

Figure 3.7: Left) Close up of right angle bend in three-axis probe
Right) Photo of bellows setup prepared for installation on TCSU

The three-axis probe was used to make scans of TCSU using repeatable shots. The midplane internal probe, axial magnetic probes, and other external diagnostics were used to confirm that the FRC conditions on each shot matched the baseline chosen for the scan. We moved the three-axis probe a few centimeters between each useable shot, generally we have 5 cm spacing with extra positions to get better resolution around the ends of the RMF antenna. The scans of the 80 cm section of TCSU yield a full 2D map of the magnetic field. We have B_r, B_θ, and B_z as a function of r and z at $\theta = 90^o$ and use this data to understand plasma behavior throughout the FRC and in the open field line region.

Chapter 4: CALIBRATION PROCEDURES

All magnetic diagnostics were absolutely calibrated in a box with well-known geometry; the magnetic field inside the box is calculated using a Biot-Savart code solver and confirmed using a loop with well known area. After the diagnostics were installed on the machine, the data was compared to the signals from the flux loops to verify the magnetic field measurements. Small calibration 'fudge factors' were added where necessary to ensure diagnostic agreement. The details regarding the 'fudge factors' are discussed later in section 4.2. First, the general calibration process for each probe is presented. This calibration converts the raw probe data into the magnetic field pointing in the correct coordinate direction.

The calibration box contains three orthogonal pairs of 8-turn coils. Each pair is wired to give a uniform magnetic field in the center of the box in each direction. Inserting the probes into the box using the final cable, integrator, digitizer setup allows for an accurate calibration.

Calibration was performed using a box containing a known magnetic field. The box was carefully made and its dimensions measured with millimeter accuracy. The box is constructed out of clear Plexiglas with crosshairs etched onto the four closed sides showing the center of the box. The probe is inserted through the open sides in the XZ plane. The B_x coils are 86 x 83 cm; B_y coils are 86 x 86 cm; B_z coils are 83 x 83 cm. The two coils of a pair are 52.5 cm apart. The two X coils were wired in series to give a uniform field and powered using a capacitor bank charged to 12kV. The current runs through high-power 33Ω resistors, shown in *figure 4.1*; 2 stacks of 11 resistors are wired in parallel. The resistors dissipate power before the current goes through the calibration box coils, which would otherwise overheat.

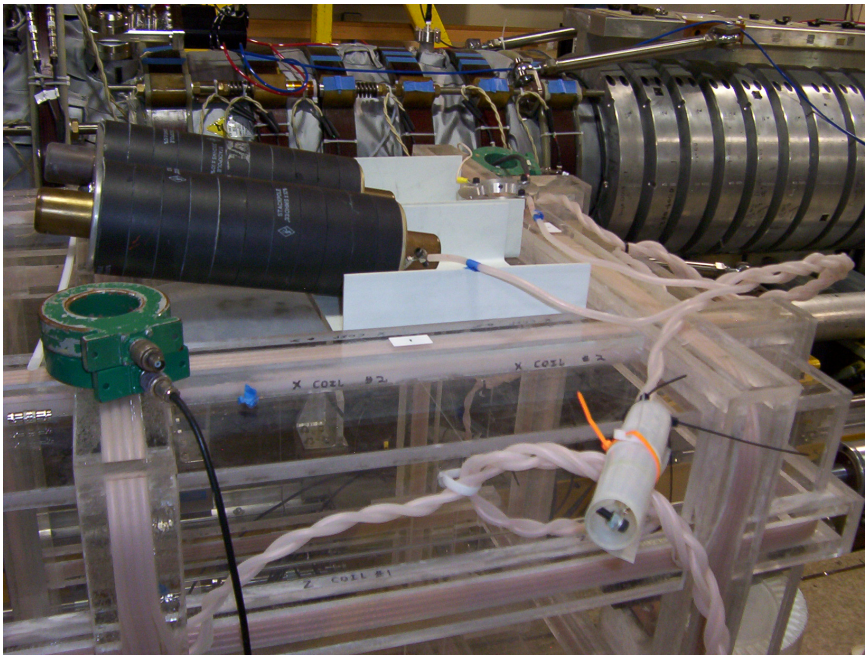

Figure 4.1: Photo of calibration box setup with resistors on top.

Section 4.1: Midplane Internal B-Field Probe (MIBP) calibration

Using a calibrated Pearson probe with 0.025V/A, 4%/msec droop, 100nsec rise time, and ITmax = 3.0amp-sec, the current through the coils was measured and using a Biot-Savart solver the magnetic field was calculated at each position in the box. The calculation was confirmed using two magnetic pickup loops of known area. Pearson probes must be terminated into 50Ω to prevent reflections. The signal from the Pearson probe was too large for the digitizers and was attenuated. The 50Ω termination divides the signal by 2 and the extra 2W attenuators added give a further division of 20. For greater accuracy, the attenuators were measured and found to give a division of 18.61.

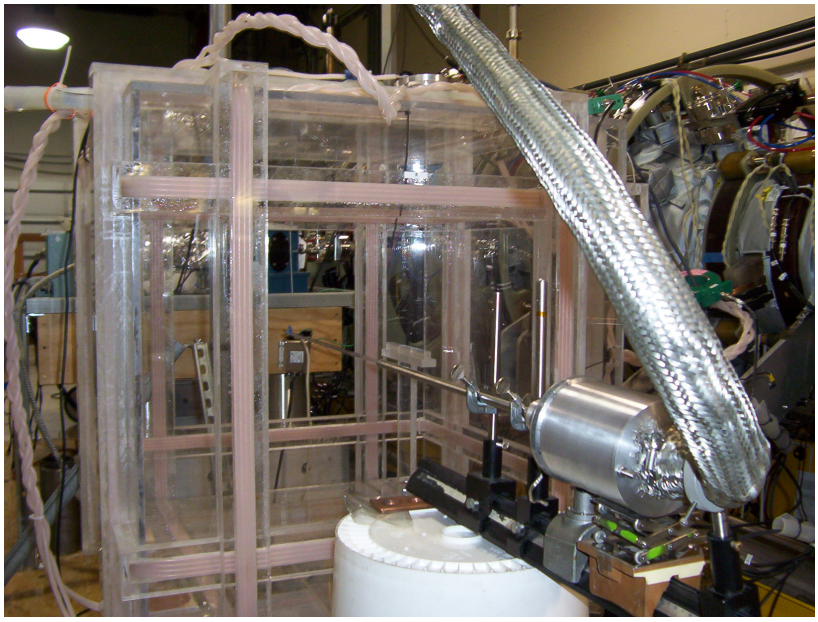

Figure 4.2: Photo of MIBP inserted into calibration box.

To get the probe setup in the box, shown in *figure 4.2*, it is mounted onto an optical rail such that the axis of the probe lines up with the centerline of the box from the side and above. A pointer, mounted on the rail, pointing to the compass attached to the probe connector housing gives an arbitrary angle to the position. With each rotation of the probe, alignment must be redone, if necessary, by shifting the optical rail. The probe is slightly flexible but alignment can, and must, be maintained to an accuracy of a few millimeters.

The field inside the box between +/- 10cm is the most uniform so only signals from the probes located within this region are considered. The magnetic field in the box is shown in *figure 4.3*. This is the output of the Biot-Savart solver, which assumes single turn coils with a 1 amp current. This data is multiplied by 8 for the number of turns and by the current measured by the Pearson probe to get the field in the box at each location. Initially, the center of the first probe winding is located at y = -10cm and a set of shots is taken. The probe is rotated through 200 degrees with at least two shots taken every 15 degrees. This is repeated with the center of the probe at y = 0, 10, 17 cm.

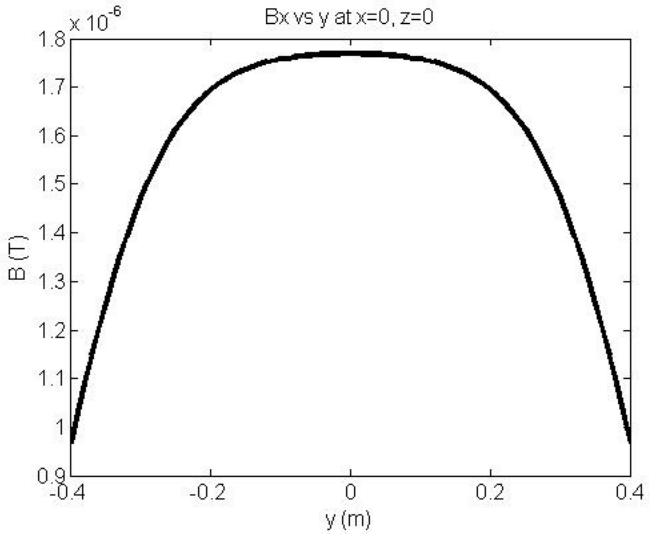

Figure 4.3: Magnetic field inside calibration box calculated by Biot-Savart solver

The fully calibrated signals from the midplane probe are called BIX and BIZ for 'B-field Internal X-direction' and 'B-field Internal Z-direction', respectively. The 24 windings are numbered from 01-24 with BIX01 and BIZ01 at y = 40 cm, BIX02 and BIZ02 at y = 38.5 cm, and so on until BIX24 and BIZ24 at y = -6 cm (past the machine axis). A single signal at a single location, called BIX01, will be used to illustrate the calibration factor calculation below.

The raw probe data is called BIXP01_Raw; the P indicates the field measured by the winding and not necessarily in the x-coordinate direction. For each shot at a single rotation angle, the peak of the raw signal is averaged. A plot is made of the rotation angle versus peak field. A sinusoidal curve fit to the data gives the angle of the zero crossing, i.e. the angle at which the BIX01 winding is parallel to the magnetic field. The peak of the curve fit gives the voltage measured when the winding is perpendicular to the field.

The first calibration numbers convert the raw probe data (BIXP01_Raw), in volts to the measured magnetic field normal to the area of the individual winding (BIXP01). For this we need numbers to fill the equation:

BIXP01 = BIXP01_Raw * RC time * attenuation / (# of turns * area of winding)

The RC times are approximately 10 μs but are measured from the integrator. The attenuation is caused by the highly resistive tungsten wire terminating into 100 Ω on the

integrator board and is calculated using the measured probe resistance which is approximately 150 Ω. the area is unknown and calculated using the data from the calibration box.

Starting with $B_{box} = (1/ARC)V_{probe}$, the area of the winding is calculated to be $A = (1/B_{box}RC)V_{probe}$. However, this does not take the attenuation into account and is an "effective" area equal to the probe area divided by the attenuation. Using the attenuation at the time of calibration allows these numbers to be separated in case the attenuation changes. The attenuation is a due to a voltage division between the termination resistance and the probe wire resistance: Attenuation = $(100\Omega + R_{probe})/100\Omega$. So now we have:

Probe Area = V_{probe}(1/Attenuation*RC time*B_{box}),

where V_{probe} is the peak of the curve fit described above. The area and winding angle is calculated for each location in the box and averaged to get better accuracy.

The probe form is flexible and has an internal twist so that the angle of the zero crossing for BIX01 will not be the same as for BIX24. Additionally, BIX01 and BIZ01 are not precisely 90 degrees apart since the individual windings can relax and deform slightly. This is why the zero crossing angle for each BIX and BIZ winding is needed in order to transform the magnetic field measured by each loop into the magnetic field pointing in the x- and z- coordinate directions on TCSU.

After the windings are turned from raw voltage, BIXP01_Raw, to the magnetic field measured by the winding, BIXP01, the signals are separated into the coordinate directions using basic coordinate transformation formulas:

BIX01 = BIXP01*cos(bix01_angle) – BIZP01*sin(biz01_angle)
BIZ01 = BIXP01*sin(bix01_angle) + BIZP01*cos(biz01_angle),

where the angle in each formula is the angle at which the probe signal is a maximum, or , the angle of the zero crossing +/- 90^o.

Now the probe is calibrated to the field in the calibration box. However, when it is installed on TCSU it will undergo an unknown rotation. To set the angle of the probe

on the machine, another set of rotation shots are taken using the bias magnetic field. The probe was again rotated through 200 degrees and the zero crossings found. The probe was then aligned so that the center winding, BIX12, was parallel to the B_z field and registered zero bias field. A bulk rotation angle was added to the individual probe angles in order to get proper calibration in the machine.

TCSU has blankets that heat the machine to approximately 100 ^oC. The tungsten wires in the probe have a temperature dependant resistance. The resistance of the heated probes is 12% larger on average. After the probe in installed and allowed to equilibrate with the heated machine, the probe resistance is measured again and the attenuation number in the calibration is changed to match the increased attenuation from the increased resistance.

As a final check of the midplane probe calibration, the bias field magnets were wired in series to give a uniform magnetic field inside the machine. Based on the position of the B_z field coils, the expected magnetic field and flux were calculated in the range Z = +/- 1.5m and R = 0 – 0.5m. This calculation was done for the ideal case of current rings in steady state. The magnitude of this calculated field was scaled to match field measured by two-axis midplane probe, averaged from r = 0 – 20 cm where the field profile is flat. *Figure 4.4* shows the calculated field in TCSU with 10 of the bias magnets wired in series.

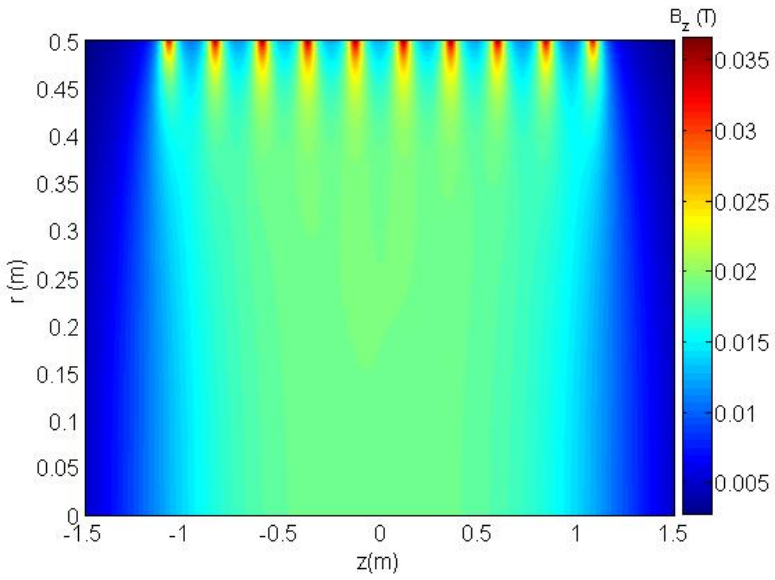

Figure 4.4: Calculated B_z for series magnets used in calibration

The two-axis midplane probe and the flux loops were independently and absolutely calibrated. If the calibrations were correct, the flux loop data should fit the calculated magnetic field given in *figure 4.5*. To make the comparison, the flux data was divided by the area of the loop in order to give a measured average field in Tesla and then fit to the curve at the radius of the flux loops, r = 40.9 cm. However, when the flux data (in Tesla) was fit to calculated B_z data, it was bigger by 6%, shown in *figure 4.5*.

The difference in the data could be due multiple factors including: Errors in the midplane probe calibration, estimated to be ~3%; errors in the measured flux loop area, as some sagging of the loops on the machine was observed; errors from poorly measured attenuator values from ÷2 and ÷5 attenuators used on the flux loops. In order to reconcile the difference, the midplane probe data was multiplied by 1.03 and the flux loop data multiplied by 0.9717 = (1.03/1.06).

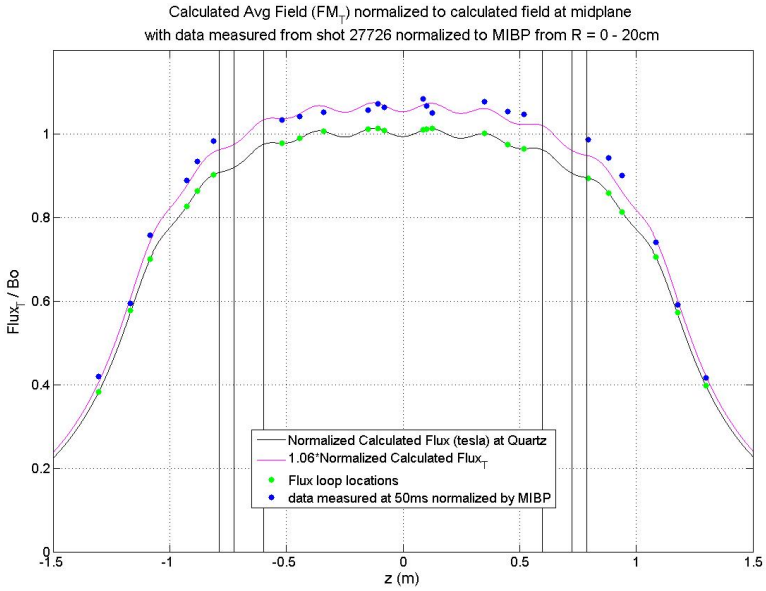

Figure 4.5: Steady state magnetic field calculated using bias magnets wired in series, scaled to match midplane internal probe, shown with flux loop data.

Section 4.2: Axial $B_z(z)$ probe array calibration (BMI & BMO)

The two axial magnetic probes needed to be re-calibrated after the installation on the bottom of the machine. The calibration was done with the bias magnets wired in series with the magnetic field shown in *figure 4.5*. The data calculated at the radial

location of the two probes (r = 38.5 cm) was axially smoothed with a 6 cm wide boxcar to capture the fact that the individual windings are axially uniform and 6 cm long.

The magnetic field calculated in *figure 4.5* is for an ideal case. However, TCSU has large stainless steel flanges and invar bellows that connect the stainless steel sections to the quartz chamber. There are also small invar bellows that connect the quartz to the stainless steel diagnostic ports. The large flanges slow magnetic field penetration and the invar bellows soak up some of the magnetic field, lowering the actual field below the expected calculated field. In order to account for these effects, data at 2.5 ms and 50 ms is considered for the calibration. At 2.5 ms, the field measured just inside the rings (from the BMI probe) is equal to the field measured outside the rings (from the BMO probe). At this point, the flux rings have no effect. At 50 ms, the bleed-through effect of the large flanges is minimized. Two calibration factors are calculated based on the data at these two times. First, the data at 2.5 ms is used to find a scale factor that is applied to all of the channels to make the data match the calculated field. Second, the data at 50 ms is used to find a deviation factor that eliminates the scatter about the calculated field curve.

Again, the two numbers needed for the calibration of the outer axial probe array (BMO) are the 29 deviation factors from the calculated magnetic field, which eliminates the random scatter and an offset scale factor. The offset scale factor for the BMO probe is 0.94. The scaled data at 2.5 ms is shown in *figure 4.6* in red; the data used to calculate the deviation factors is shown in blue. The windings directly under the flange are still affected by the longer field soak through time and are not corrected to fit the calculated field curve. Instead, the average of symmetric pairs is used to calculate the deviation factor. These are: BMO06 & BMO24, BMO07 & BMO23, and BMO08 & BMO22. *Figure 4.7* shows the corrected data at 0, ms, 2.5 ms, and 50 ms.

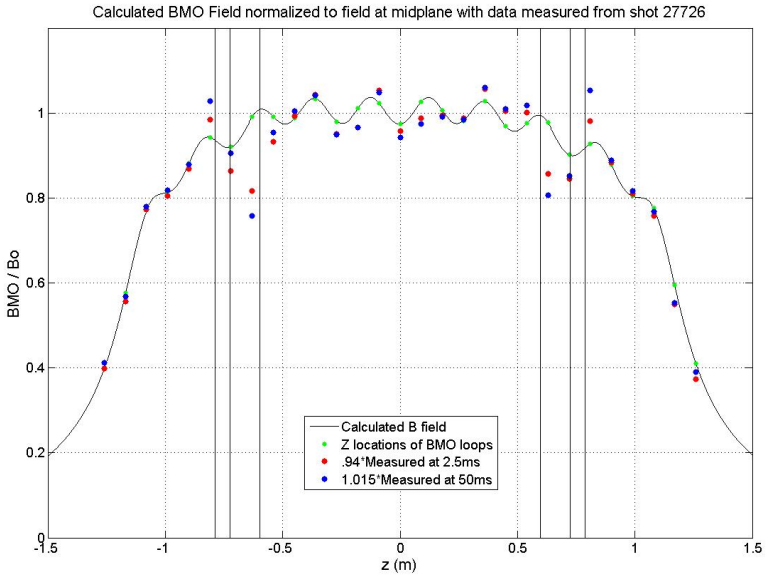

Figure 4.6: BMO data scaled to match calculated curve

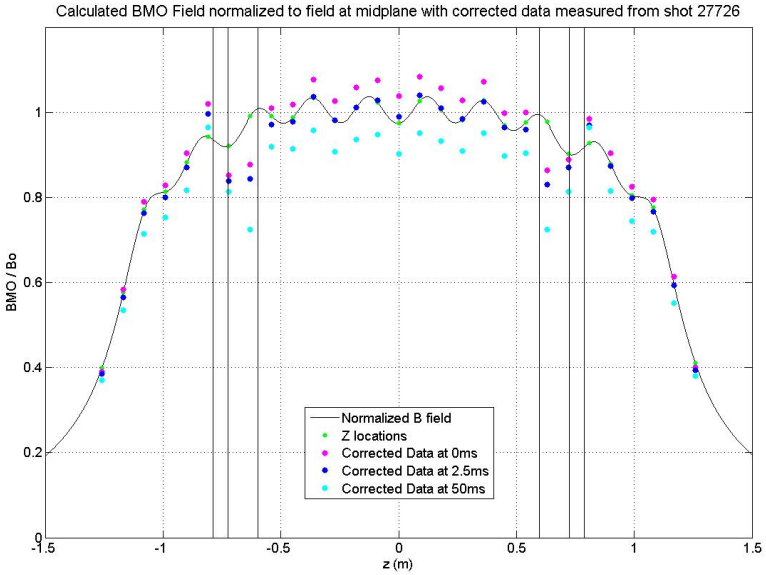

Figure 4.7: Corrected BMO data for shot 27726

The same method is used to calculate the axial probe measuring the field just inside the flux rings (BMI). The data from 2.5 ms is scaled by 0.93 to match the calculated magnetic field. Again, the data at 50 ms is used to calculate the deviation from the calculated magnetic field. As with the BMO probe, the deviation factors for loops BMI06-BMI08 and BMI24-BMI22 are calculated from the average of the symmetric pairs. However, the BMI probe is located in the trough at the base of the flux rings and has three windings on top of three small invar bellows that are in the diagnostic ports.

These small invar bellows soak up some field, lowering the field in these three locations. To calculate the deviation factors for probes BMI12, 15, 18, the average of the three data points is taken and the deviation factor for each loop is the deviation from that average value.

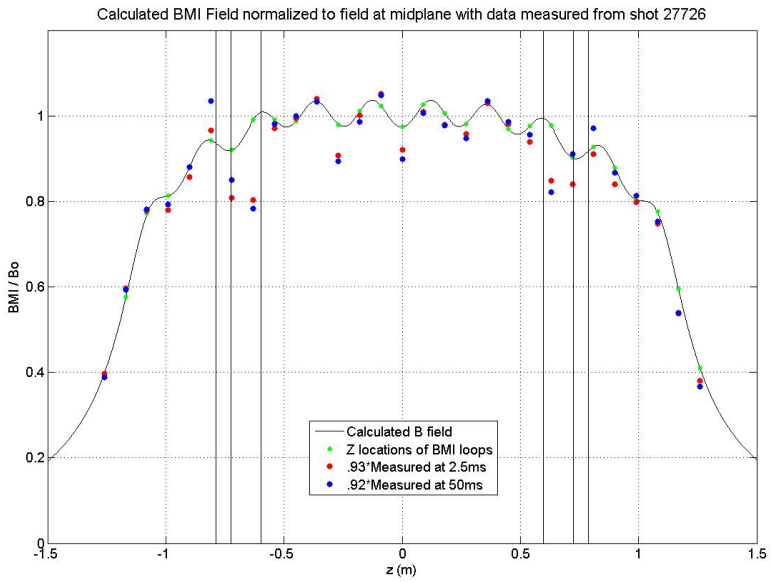

Figure 4.8: Uncorrected Scaled Data

This calibration uses the same as the method for the BMO data except that BMI12, 15, 18 are averaged to find the deviation factor because they are over small invar ports and are lower than the calibration curve by about 4%. So, BMI Corrected = 0.93*DF*BMI.

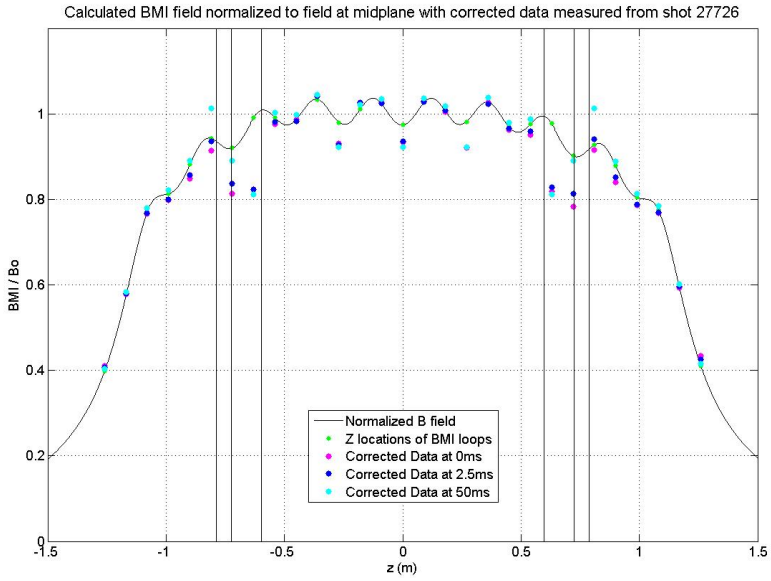

Figure 4.9: Corrected BMI data

Section 4.3: Three-axis probe calibration

The calibration procedure for the three-axis probe was similar to that of the two-axis midplane probe. However, since all three directions are measured the procedure can be done using a matrix coordinate inversion.

Initial calibration factors are applied to convert the raw voltage signal to a signal approximately equal to the magnitude of the magnetic field in the direction normal to the probe winding; these are called **BTXP** ('**B**-field, **T**ranslatable, **X**-loop, **P**robe direction'), **BTYP** ('**Y**-loop'), and **BTZP** ('**Z**-loop). As with the midplane two-axis probe, they are in the form:

BTXP01 = BTXP01_Raw (volts) * RC time * attenuation / (# of turns * area of winding)

The RC time is approximately 10 μs but is slightly different for each channel. If an integrator needs replacing the calibration is easily modified. The attenuation is based on the resistance of the wire terminated into 2000 Ω on the integrator. This is 1.07, 1.09, 1.08 for the x, y, and z windings, respectively. The areas are approximate; for x, y, and z they are 7, 2, and 4.5 cm^2, respectively. A negative sign is added to make the signals positive where the field is positive.

With the probe inserted into the box each coil pair is fired individually to get the probe response to a B_x, B_y, and B_z field. To calculate the field in the x, y, and z direction we must find the matrix A such that B = A*BP or,

$$\begin{bmatrix} Bx \\ By \\ Bz \end{bmatrix} = \begin{bmatrix} a11 & a21 & a31 \\ a12 & a22 & a32 \\ a13 & a23 & a33 \end{bmatrix} \begin{bmatrix} BPx \\ BPy \\ BPz \end{bmatrix},$$

where Bx, By, Bz is the field in the vector direction x, y, z, and BPx, BPy, BPz is the value measured by the probe.

Using the calibration box the inverse matrix A^{-1} is easily calculated.

$$\begin{bmatrix} a11' & a21' & a31' \\ a12' & a22' & a32' \\ a13' & a23' & a33' \end{bmatrix} \begin{bmatrix} Bx \\ By \\ Bz \end{bmatrix} = \begin{bmatrix} BPx \\ BPy \\ BPz \end{bmatrix}$$

For example, firing B_x only gives a11'*Bx = BPx, a12'*Bx = BPy, a13'*Bx = BPz. Repeating this calculation for B_y and B_z yields each element of the A^{-1} matrix; a simple inversion gives the A matrix used to transform the magnetic field normal to each probe winding into the magnetic field in the coordinate directions.

Transferring the probe from the calibration box to the machine will include rotating the probe about the y-axis. To get a final calibration in TCSU a rotation matrix is needed to re-align the data for the TCSU coordinate system. In TCSU, +X = west, +Y = up, +Z = north. The three-dimensional rotation matrix, holding the y-axis fixed, is:

$$R = \begin{bmatrix} \cos\theta y & 0 & \sin\theta y \\ 0 & 1 & 0 \\ -\sin\theta y & 0 & \cos\theta y \end{bmatrix}$$

where θy is the angle of rotation about the y-axis from the original calibration orientation. In addition to rotating the probe between calibration and machine installation, the probe form can twist inside the probe housing such that each winding will have a different twist about the fixed y-axis; a different θy is calculated for each of the 30 X and 30 Z windings.

The final calibration is of the form B = R*A*BP

$$\begin{bmatrix} Bx \\ By \\ Bz \end{bmatrix} = \begin{bmatrix} \cos\theta y & 0 & \sin\theta y \\ 0 & 1 & 0 \\ -\sin\theta y & 0 & \cos\theta y \end{bmatrix} \begin{bmatrix} a11 & a21 & a31 \\ a12 & a22 & a31 \\ a13 & a23 & a33 \end{bmatrix} \begin{bmatrix} BPx \\ BPy \\ BPz \end{bmatrix}$$

After final installation in TCSU, the θy is calculated by firing the B_z coils only. Say, T = A*BP where T is the "transformed" data but not necessarily in the correct orientation yet. So,

$$\begin{bmatrix} Tx \\ Ty \\ Tz \end{bmatrix} = \begin{bmatrix} a11 & a21 & a31 \\ a12 & a22 & a32 \\ a13 & a23 & a33 \end{bmatrix} \begin{bmatrix} BPx \\ BPy \\ BPz \end{bmatrix},$$

then, firing only B_z gives:

$$\begin{bmatrix} Bx \\ By \\ Bz \end{bmatrix} = \begin{bmatrix} \cos\theta y & 0 & \sin\theta y \\ 0 & 1 & 0 \\ -\sin\theta y & 0 & \cos\theta y \end{bmatrix} \begin{bmatrix} Tx \\ Ty \\ Tz \end{bmatrix} = \begin{bmatrix} 0 \\ 0 \\ Bz \end{bmatrix}$$

and Bx = 0 = Tx*cos(θy) + Tz*sin(θy) gives θy = arctan(-Tx/Tz)

A quick recalibration was done to find a new θy for each scan. Vibration from moving the probe could effect the internal twist over time.

After the full calibration was done, the data from the three-axis probe, placed at the midplane, was compared to the data from the midplane two-axis probe. Data from a vacuum shot without the RMF was used as a comparison. It was found that the three-axis probe data was giving a lower magnetic field than the two-axis probe. After the extensive calculations made to reconcile the midplane internal probe and the flux loop signals it was decided to use the midplane probe and flux signals as the definitive TCSU magnetic field measurements. In order to correct the three-axis probe data a comparison was made using the two loops of the midplane probe that match locations of loops in the three-axis probe. These are BIZ02 with BTZ08 and BIZ05 with BTZ04. With a scale factor of 1.08 the BTZ data matched the BIZ data and this was applied to all the loops on the three-axis probe.

Chapter 5: **BASIC MEASUREMENTS and PLASMA PARAMETERS**

The analysis of TCSU data using the three-axis probe focuses on stable, repeatable FRCs formed using 122 kHz even-parity RMF and 107 kHz odd-parity RMF. This chapter gives an overview of the basic plasma parameters for each FRC scanned by the three-axis probe and details the information acquired using the magnetic diagnostics. The basic parameters measured by the external diagnostics describe two FRCs that are similar, regardless of parity; they have a similar temperature, density, and magnetic field. The odd-parity FRC is driven with a smaller current in the RMF antennas implying better current drive efficiency. The internal magnetic measurements show, for the first time, the structure of the average toroidal field inside the FRC.

This chapter provides an overview of the data collected on TCSU. First, there is a summary of the external diagnostics for even- and odd-parity. Second, details of the general magnetic field behavior are discussed, focusing on the data collected at the midplane as well as the axial magnetic field data collected around the flux conserving rings. While this data begins to expose the underlying differences in the two types of RMF current drive it was only with the implementation of the three-axis probe that the full structure came into view. In section 5.3, the full r-z map of each FRC is presented to show the steady state behavior; the steady state data is the primary focus of further analysis. However, we can also use the three-axis probe to watch the formation of the FRC; a short time series is presented. In addition to forming a comprehensive picture of the average state of the FRC, we now have enough information to see the distribution of the RMF and other frequency components that contribute to the FRC equilibrium. The oscillating data is summarized in section 5.4 and analyzed further in subsequent chapters. Section 5.5 presents a brief comparison of the three-axis probe data to the NIMROD simulations performed for the even- and odd-parity RMF configurations.

Section 5.1 External diagnostic data

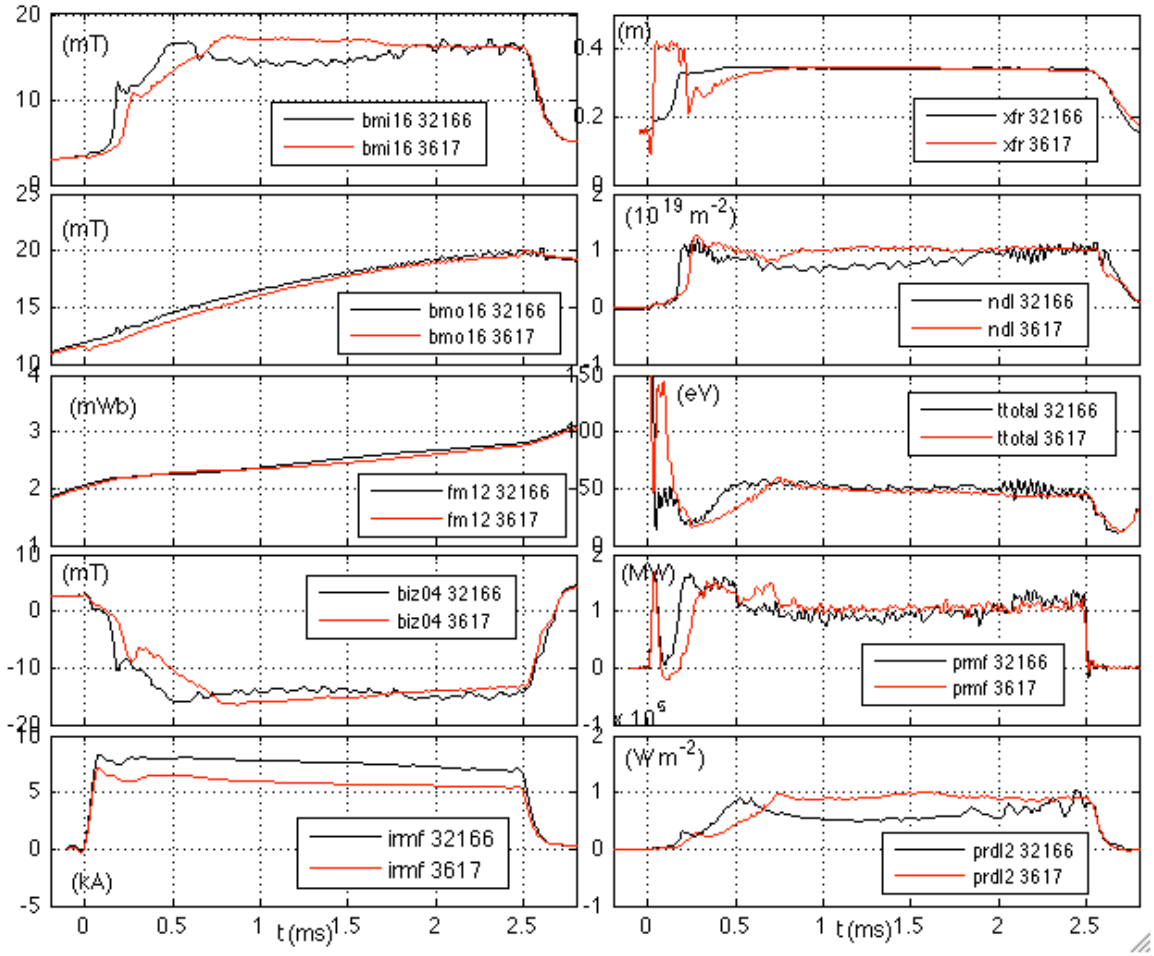

Figure 5.1: Overview of typical plasma parameters measured for even-parity (black) and odd-parity (red) RMF formed FRCs

A sample of the data taken on every shot is shown in *figure 5.1*. The RMF is applied for 2.5 ms. The black traces are from an even-parity RMF formed FRC and the red traces are from an odd-parity RMF formed FRC. Most plasma parameters are similar. The first two traces, bmi16 and bmo16, show the magnetic field inside and outside the flux conserving rings near the axial midplane. The timing and voltage of the capacitor banks that power the bias magnets (shown in *table 5.1*) is arranged such that the field outside the rings rises above the field inside the rings after the formation of the FRC; this maintains flux inside the rings and provides a quasi-stable equilibrium. The next trace, fm12, shows the flux at the midplane measured by a flux loop at r = 40.5 cm, outside the vacuum chamber. The reversed magnetic field near r = 0 at the midplane is shown in the

fourth panel. The bottom left box shows the RMF antenna current given by $I_{RMF}^2 = I_{horiz}^2 + I_{vert}^2$, where I_{horiz} and I_{vert} are the currents in the horizontal and vertical RMF antennas. A smaller current in odd-parity operation yields plasma parameters similar to those in even-parity operation. The excluded flux radius at the midplane is calculated from the external flux loop and the axial magnetic loops inside and outside of the internal rings as in *equation 3.2*. The line-integrated density is from the two-pass CO_2 interferometer. The total temperature is calculated from pressure balance using *equation 5.1*. The absorbed RMF power (prmf) is 1 MW. The total radiated power (prdl2) is larger for odd-parity and is measured by several bolometers.

The inductance of the odd-parity antenna configuration is higher than for even-parity which results in a lower antenna current for the same voltage despite the lower operating frequency. However, odd-parity achieves similar plasma parameters once in steady state. The odd-parity FRC formation phase last longer and the steady state FRC has slightly higher density and radiated power; these are most likely consequences of the larger gas puff that was needed for consistent operation. *Table 5.1* gives the machine operating parameters for the probe scans. The RMF is turned on at 0.0 ms and is applied for 2.5 ms. The voltage and timing for each capacitor bank were the same in each case while the gas injection was much larger in odd-parity.

Module/time	122 kHz Even	107 kHz Odd
BCMP	0 V	0 V
BCMP time	-25 ms	-25 ms
ENSP	1000 V	1000 V
ENSP time	-15 ms	-15 ms
CEP	125 V	125 V
CEP time	-14 ms	-14 ms
CCP	250 V	250 V
CCP time	-9 ms	-9 ms
CMP	340 V	350 V
CMP time	-1.5 ms	-2 ms
RMFP	12 kV	12 kV
RMF time	0 ms	0 ms
PUFF1	8.5 psia	16 psia
puff1 duration	-25 to -22.5 ms	-25 to -24.78 ms
PUFF2	35.5 psia	52 psia
puff2 duration	-3.7 to +2 ms	-3.5 to +3 ms

Table 5.1: TCSU input parameters for each three-axis probe scan.

Section 5.2: Overview of magnetic probe data for even- and odd-parity FRCs

The magnetic probes provide detailed information about the shape and internal structure of the FRCs. Using the two-axis midplane magnetic probe we can see the magnetic field reversal and begin to investigate the frequency content. *Figures 5.2-5.5* show each signal from the midplane probe from the loops near r = 0 (biz01-biz05) showing full field reversal to the field outside the rings at r = 40 cm (biz24). A close-up of the unfiltered data shown in *figure 5.2* shows the transition from the stable FRC to a developing n=2 rotational mode at 2 ms. The n=2 mode was common but generally not disruptive. However, the mode behavior was not consistent between shots so the data during this time was not used in the analysis of the three-axis probe scan.

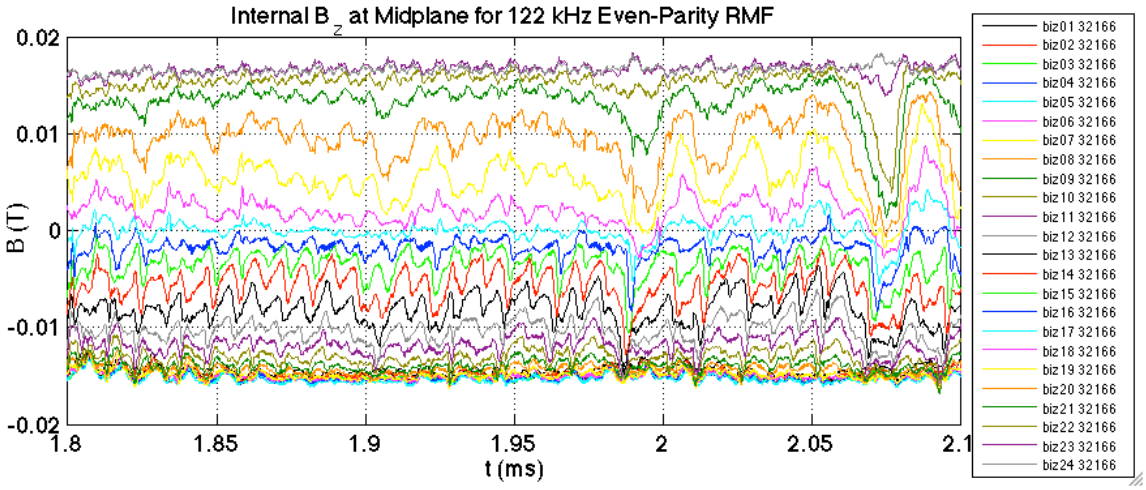

Figure 5.2: Typical $B_z(r)$ unfiltered data measured from the midplane probe for a short period of time showing field oscillations and the beginning of an n=2 mode.

Data filtered with a 10 kHz low-pass filter (*figure 5.3)* shows the average field behavior and gives a clear picture of the formation phase, steady state period, and the oscillations that develop at the end. The FRC begins to grow at 150 µs and is fully formed by 500µs. The steady state period of the FRC is 0.6 – 2.0 ms when the average magnetic field behavior is stable and generally constant.

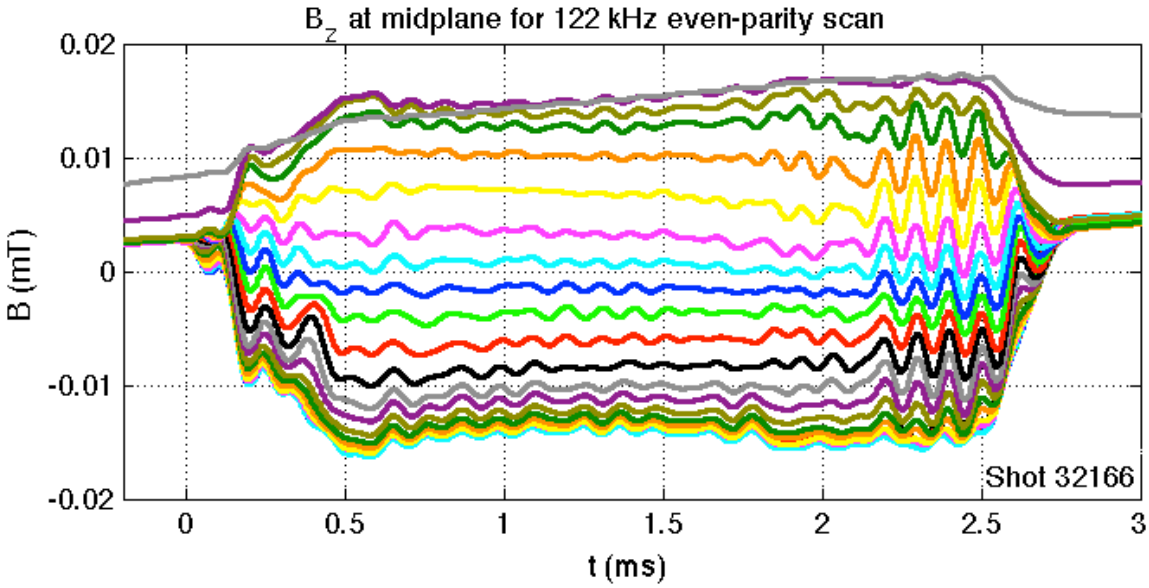

Figure 5.3: Lifetime of the even-parity FRC shown using the average values of the magnetic field from applying a 10 kHz low-pass filter. The RMF shuts off at 2.5 ms and the FRC decays.

Figure 5.4 shows the unfiltered data from the midplane probe for the odd-parity case. The large azimuthal current in the antenna at the midplane produces a large oscillating B_z field at the RMF frequency that is picked up by the midplane internal probe. The FRCs formed with odd-parity were more repeatable and did not develop the n=2 rotation.

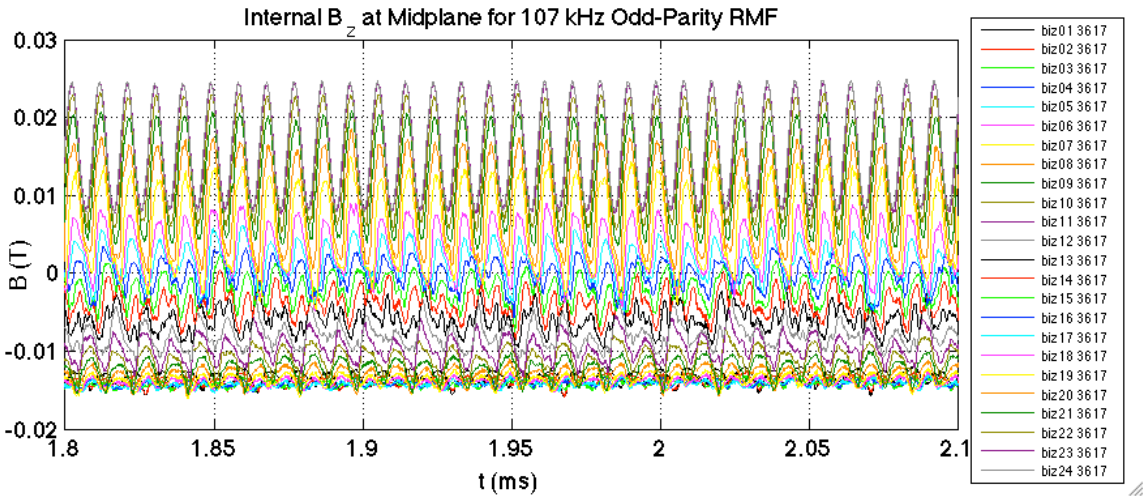

Figure 5.4: Unfiltered $B_z(r)$ data from the odd-parity driven FRC showing RMF oscillations at the outer radii and no n=2 mode development.

Again using the 10 kHz low-pass filter, *figure 5.5* shows the whole picture of the odd-parity FRC internal magnetic field. The odd-parity driven FRC has a longer

formation period but has a more stable average magnetic field and does not develop an n=2 rotation. The quiescent period of the odd-parity FRC is approximately 0.8 – 2.5 ms.

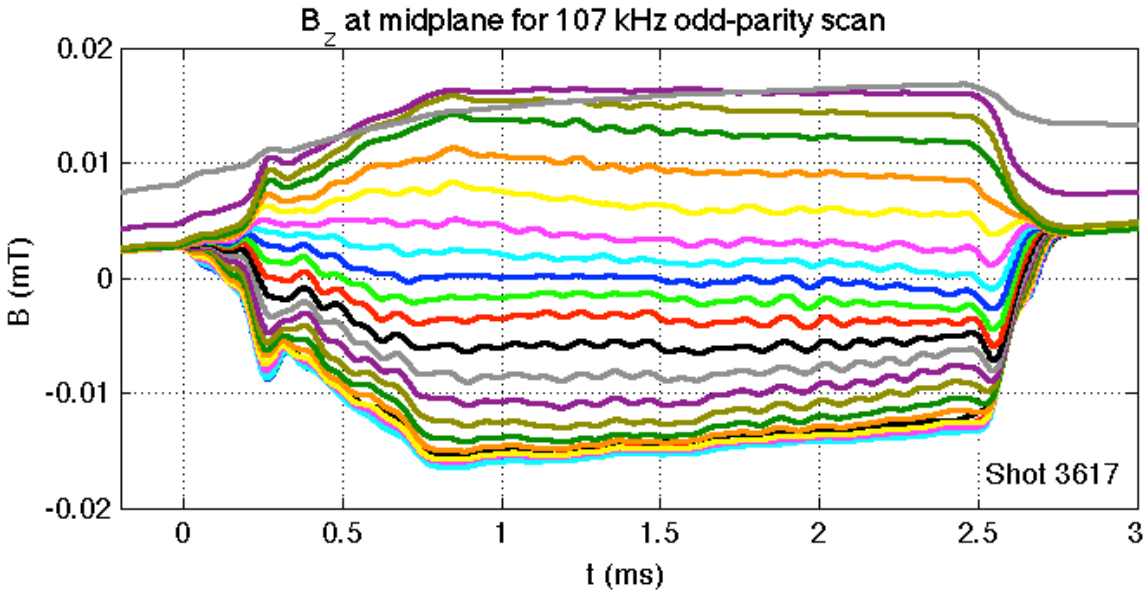

Figure 5.5: Lifetime of the odd-parity FRC displayed using the average magnetic field values from applying a 10 kHz low-pass filter.

Taking a time slice during the steady state period highlights the differences in the radial profiles. Shown in *figure 5.6* is the average axial magnetic field (B_z) with the envelope of the RMF B_θ. In the odd-parity case, B_θ is zero at the midplane because the RMF is in the z-direction. The even-parity RMF peaks just inside the separatrix and penetrates to the magnetic field null. There is some wiggle of these profiles in time but the B_z profile for odd-parity has a slightly larger peak field.

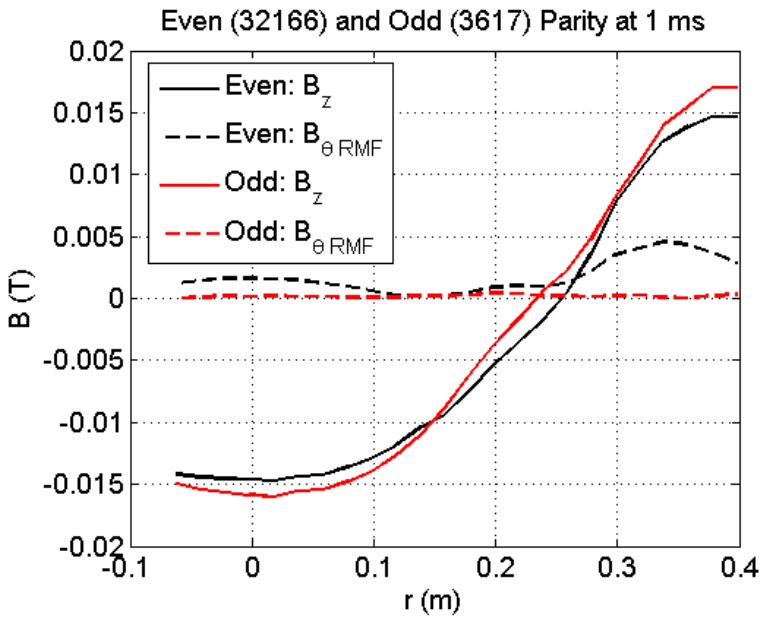

Figure 5.6: Typical radial profiles at the midplane of the B_θ RMF envelope and average B_z field.

Given the radial magnetic field profile we can calculate the radial density profile, shown in *figure 5.7*. Assuming radial pressure balance with a uniform total temperature given by *equation 5.1*, the density profile is scaled and iterated until the line integral of n(r) agrees with the interferometer data.

$$n(r)kT_t + \frac{B_z(r)^2}{2\mu_o} + \frac{B_{\theta RMF}(r)^2}{4\mu_o} + \int_r^{r_w} \rho(r)\Omega_i^2 r dr = p_{wall} + \frac{B_e^2}{2\mu_o} + \frac{B_{\theta RMF}(r_w)^2}{4\mu_o} \qquad (5.1)$$

The density profile is set such that the minimum density is 0. In *equation 5.1*, T_t is the total temperature ($T_i + T_e$), $B_{\theta RMF}$ is the envelope RMF frequency component of B_θ, Ω_i is the ion rotation frequency, which is set to 10 kHz.

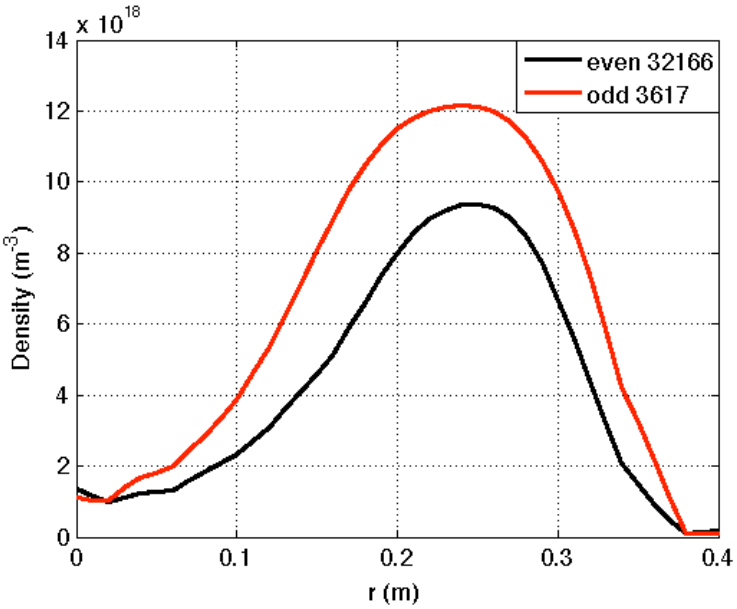

Figure 5.7: Radial density profiles calculated from pressure balance for even- and odd-parity RMF.

The data presented so far has been taken at the midplane at z = 0. In order to get an idea of the axial behavior of the FRC, we use the axial magnetic probes that measure B_z inside and outside of the flux conserving rings. Shown in *figure 5.8* is B_e as a function of axial position showing the formation of the even- and odd-parity FRCs. The initial bias field is shown in black; the plasma reaches steady state at 1 ms (blue). The initial field starts to be compressed at 0.2 ms (orange) but the FRC is still growing. At 0.5 ms (green), the FRC has formed but has not reached steady state. The FRC initially forms with a long separatrix and then undergoes axial length contraction as it reaches steady state at 1 ms.

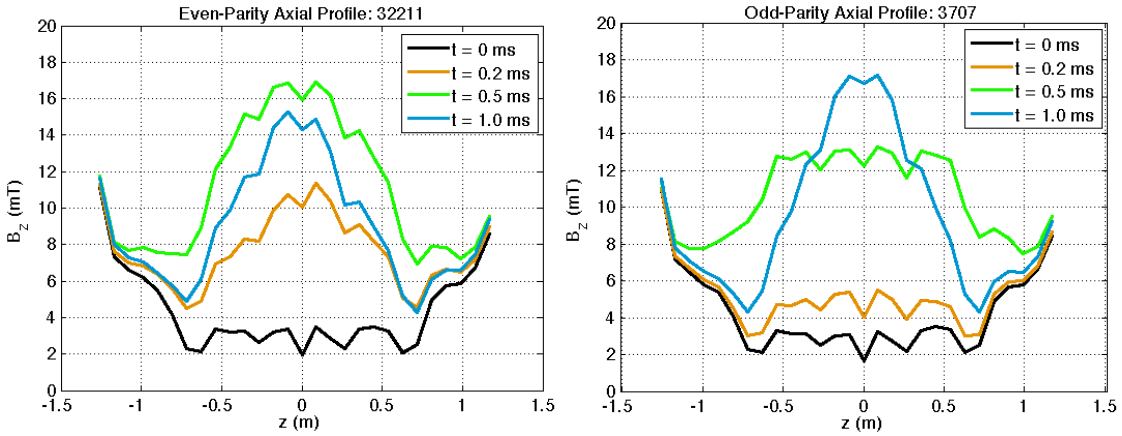

Figure 5.8: FRC external field profiles for even- (left) and odd-parity (right) measured from inner $B_z(z)$ probe (BMI) showing the compression of the initial bias field during the formation of the FRC.

As discussed in *section 3.1,* the axial B_z probes are used to calculate the flux on the rings and the excluded flux radius using *equations 3.1* and *3.2*; these are shown in *figure 5.9* for both operating conditions.

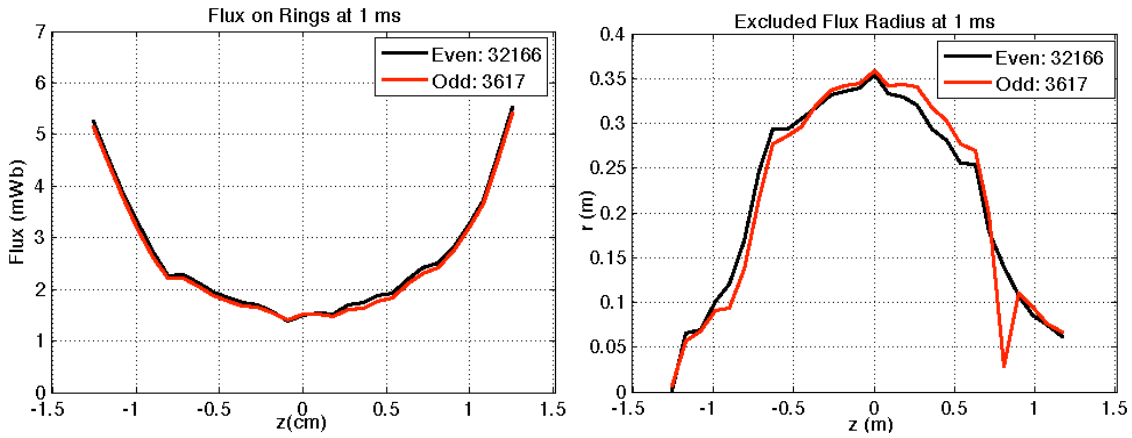

Figure 5.9: Magnetic flux on the rings (left) and excluded flux radius (right) for even-parity (black) and odd-parity (red) calculated from the $B_z(z)$ axial probes.

It appears that the even-parity FRC is shifted slightly to the –z direction. The evolution of the excluded flux radius over the lifetime of the FRC is shown in *figure 5.10.*

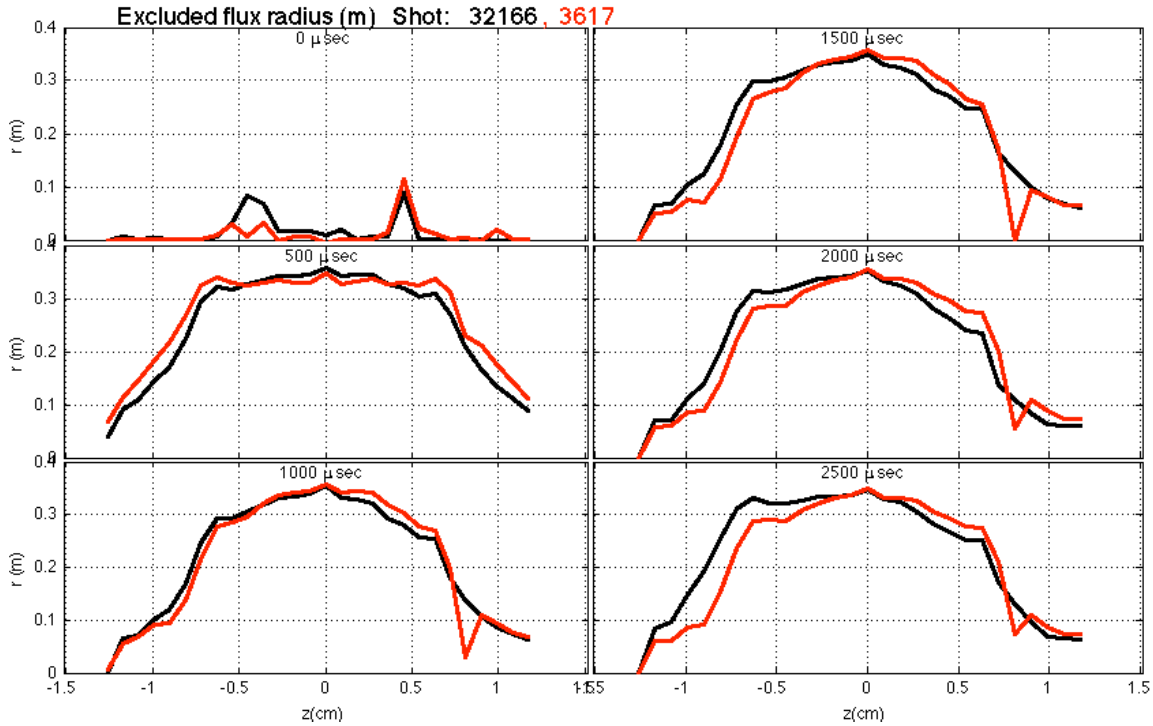

Figure 5.10: Time series of the excluded flux radius for even- (black) and odd-parity (red) FRCs.

Again, we see the even-parity FRC forms symmetrically (at 500 μs) and then begin to shift toward the south while the odd-parity FRC remains symmetric. *Figure 5.10* also shows the length contraction of each FRC between 500 and 1000 μs.

Section 5.3: Three-axis probe scan summary

The above data formed the baseline FRC used for the three-axis probe scans of TCSU. Once the baseline was established, the three-axis probe was positioned at one end of its range and plasma shots were taken until the data matched the baseline. A match was accepted if qualitative agreement was seen in measurements at the midplane and the $B_z(z)$ probes presented a consistent axial magnetic field profile. After achieving good agreement, the probe was moved 5 cm and the process repeated. At various locations such as the midplane or antenna ends (+/- 0.6 m), the probe was moved in 2 cm increments to achieve higher resolution. We have 65 axial measurements for the even-parity FRC and 76 axial measurements for the odd-parity FRC. The probe scans yield a full picture of the magnetic field inside the FRC and in the open field line region. In this section, the 2D r-z field maps are presented to give an overall picture of the magnetic structure measured by the three-axis probe. The average field data from applying a 10 kHz low-pass filter gives the overall behavior of the FRC; this data is shown in *figures 5.11 – 5.14*. The magnetic flux contours are calculated using the average field data to get the general shape of the FRC. The flux is given as

$$\Phi = 2\pi \int_0^r r B_z(r) dr \,. \tag{5.2}$$

During the steady state period of the FRC, when the data is generally constant, the shape of the FRC is stable, as seen in *figure 5.11*. The closed flux contours of the FRC are shown in blue with black lines showing the magnetic flux in the open field line region. The FRC is approximately 1.6 m long. The arrows are B_rB_z vectors showing the direction of the magnetic field in the 2D slice mapped out by the three-axis probe. Again, we focus on the average fields (below 10 kHz) at 1 ms to get a picture of the steady state magnetic field behavior.

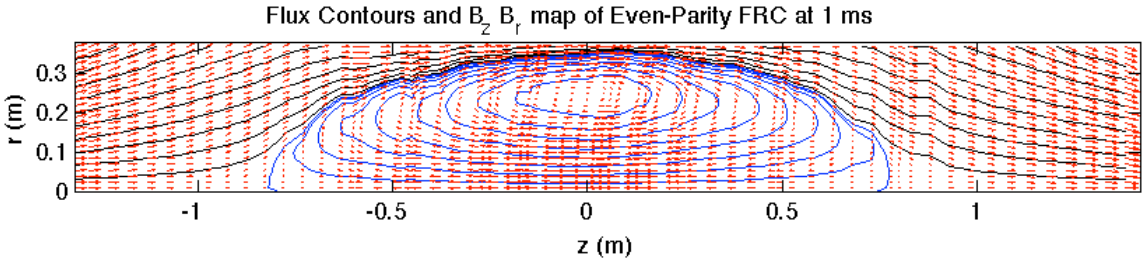

Figure 5.11: Flux contours of even-parity FRC with arrows showing B_zB_r magnetic field vectors at 1 ms during steady state.

Figure 5.12 shows the steady state B_θ that develops within the FRC and on the open field lines. The sign of B_θ flips across the midplane. B_θ within the FRC is caused by a circulating current that flows inward at the midplane and back out around the ends of the FRC. The inward j_r is an essential feature of even-parity RMF sustainment where the RMF does not fully penetrate the FRC. As explained in *section 2.1*, where $\langle j_z B_r \rangle = 0$, a positive $j_r B_z$ is necessary to sustain current drive. The toroidal field in the open field line region is due to line-tying; the open magnetic field lines are tied to a conducting boundary past the ends of the domain of the three-axis probe. Under the RMF antenna in the quartz region of the confinement chamber, the open field lines rotate with the RMF. Because the field lines rotate in the center and are tied at the ends, they twist up until they reach an equilibrium dictated by the resistivity and a steady state B_θ is created. A symmetric FRC would have an equal magnitude of B_θ on either side of the midplane but it appears that the even-parity FRC is shifted slightly to the –z direction, which is what we saw in *figure 5.10*. Perhaps, the asymmetry in the FRC contributes to the asymmetry in B_θ.

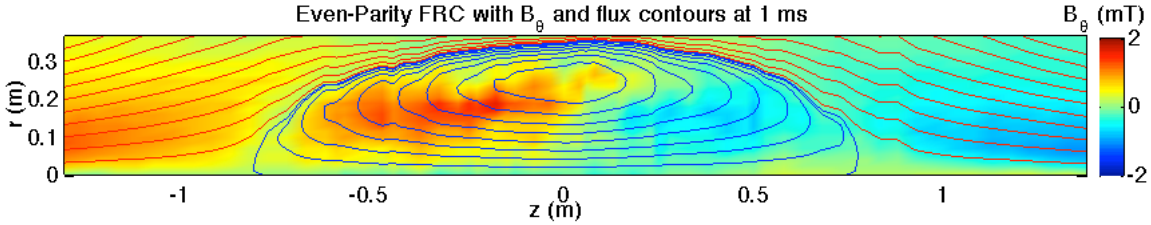

Figure 5.12: Even-parity FRC flux contours showing a small steady state B_θ.

The odd-parity RMF driven FRC in *figure 5.13* has a similar field line structure and B_rB_z field vectors.

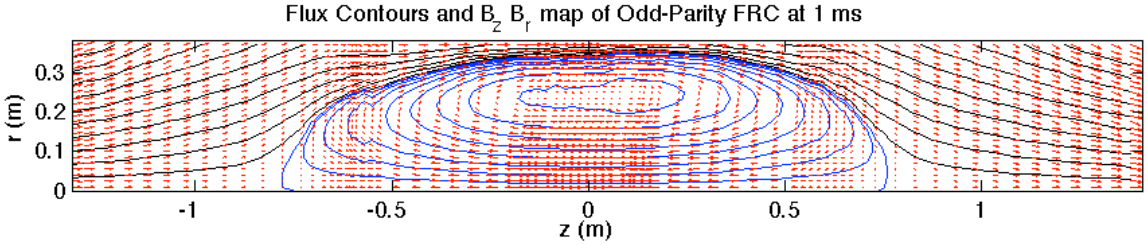

Figure 5.13: Odd-parity FRC with flux contours and B_rB_z vector field during steady state.

However, the steady state $B_{\theta,}$ seen in *figure 5.14,* shows a four-lobed structure to the internal field. The structure of the circulating currents is a more complicated figure-8 type shape.

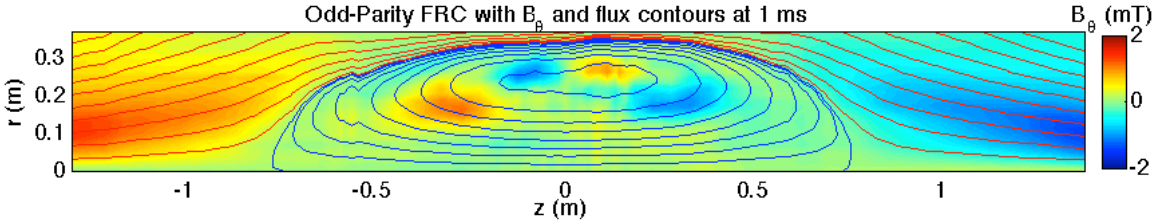

Figure 5.14: Odd-parity FRC flux contours showing the steady state B_θ.

The scans of each RMF configuration provide a full r-z cross-section of the FRC and allow for a general comparison of the size and structure. In each scan, the FRC has an elliptical shape. The internal structure of the even-parity FRC shows a small toroidal field going in opposite directions on either side of the midplane. In odd-parity operation there is a four-lobed internal structure to the toroidal field.

A short time series of the formation of the odd-parity FRC shown in *figure 5.15* shows the initial formation of the FRC to be almost 2 m long before it undergoes axial length contraction as it settles to steady state.

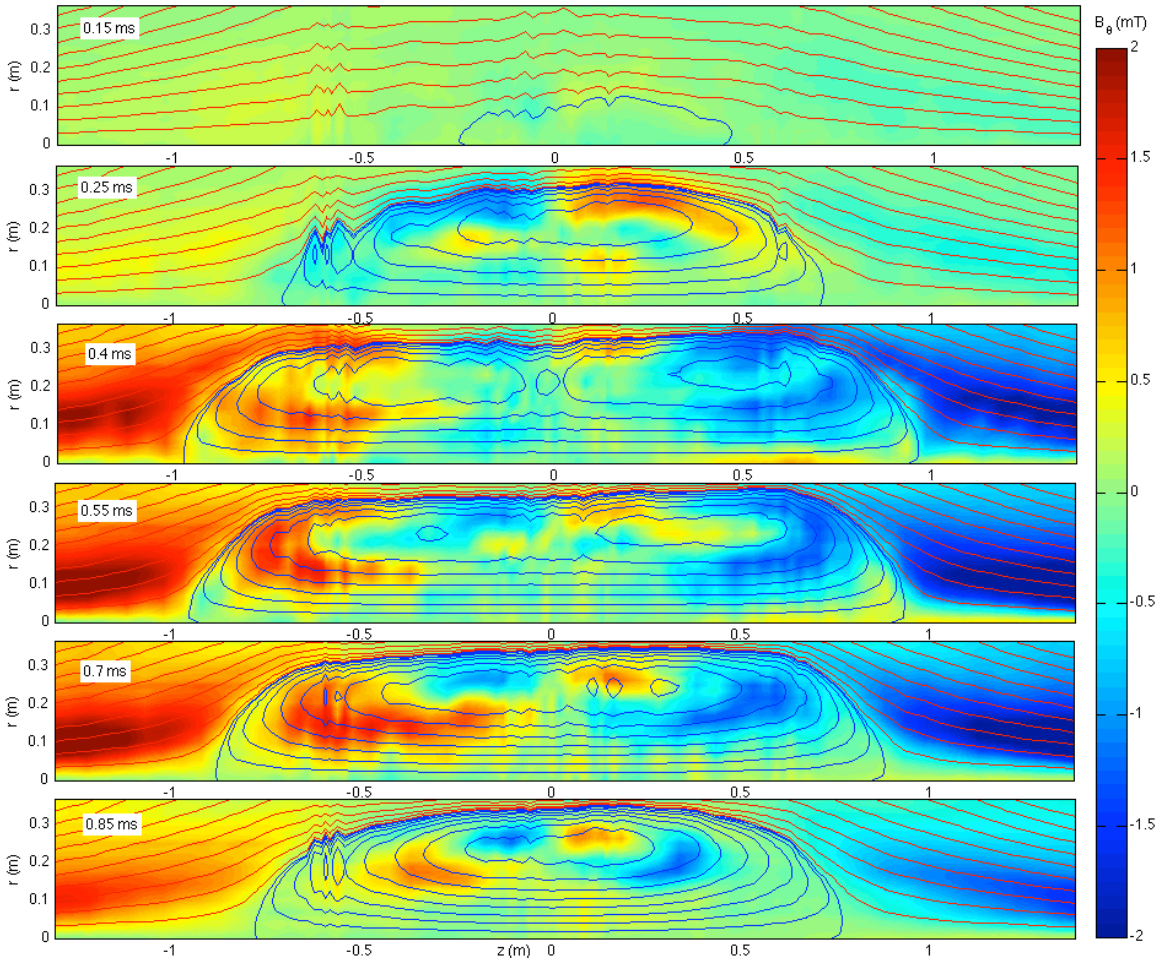

Figure 5.15: Time series of odd-parity FRC formation showing flux contours and B_θ from data filtered with a 10 kHz low-pass filter.

Section 5.4: Oscillating magnetic field data

So far the data presented has been low-pass filtered at 10 kHz but the frequency spectrum shows activity at higher frequencies. *Figures 5.16 – 5.18* show the frequency spectrum measured by the three-axis probe at the midplane as a function of radius for B_x, B_y, and B_z, respectively. Each figure compares the frequency spectrum of even-parity (left) and odd-parity (right). The data shows that a few distinct frequency peaks dominate the magnetic field activity. Understanding the dominant frequency activity and the variation between even- and odd-parity FRCs will aid in understanding the plasma dynamics.

There are a few significant features seen in the frequency spectrum plots. First, there are peaks at the RMF frequency in B_x and B_y for even-parity but a large signal only on B_z for odd-parity. Remember *figure 1.3;* the RMF antenna is split at the midplane to create the odd-parity configuration. In even-parity, the azimuthal current from the antenna straps around the midplane cancels; the RMF at the midplane is a transverse field and is picked up by the B_x and B_y probes. However, in odd-parity, the azimuthal current from each antenna strap adds to create a large B_z signal oscillating at the RMF frequency. The distinct frequency spectrum seen in the odd-parity B_z plot is due to the complicated RMF structure at the midplane.

The even-parity and odd-parity FRCs each show activity in the frequency spectrum around 30 kHz, specifically, 37 kHz for even-parity and 28 kHz for odd-parity. In addition to the ~30 kHz peaks there are signals in the spectrum at RMF + 30 kHz and RMF – 30 kHz. These peaks in the frequency spectrum were observed in certain conditions on TCS as well as in earlier work on TCSU[**24**]. In the previous TCS device, this frequency was associated with edge-drive mode[**25**], which is related to but did not fully describe the plasma behavior. The three-axis probe has improved our understanding of the mechanisms that produce the spectral data; the behavior of the 37 kHz signal from the even-parity driven FRC is discussed further in *chapter 7*.

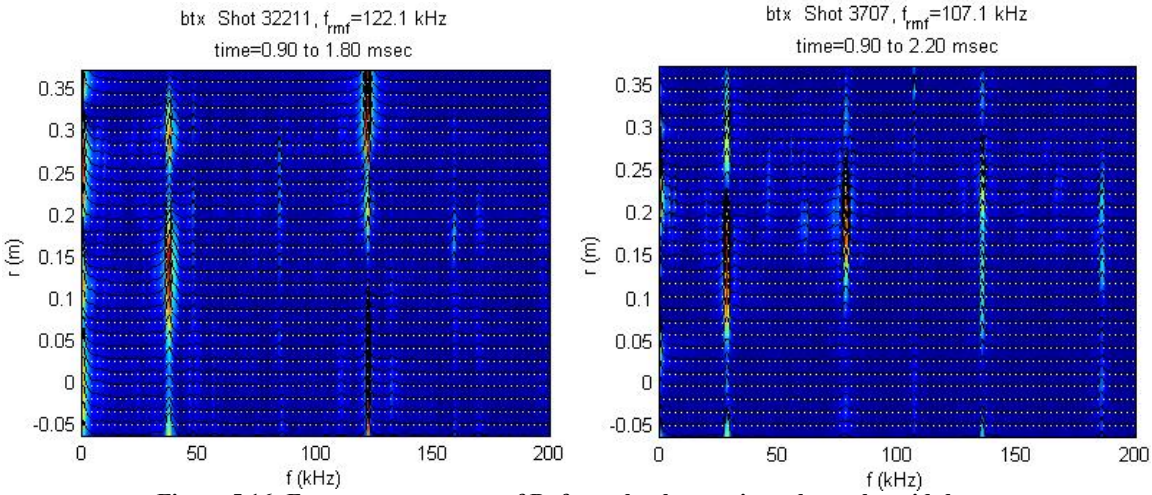

Figure 5.16: Frequency spectrum of B_x from the three-axis probe at the midplane. Even-parity (left) and odd-parity (right)

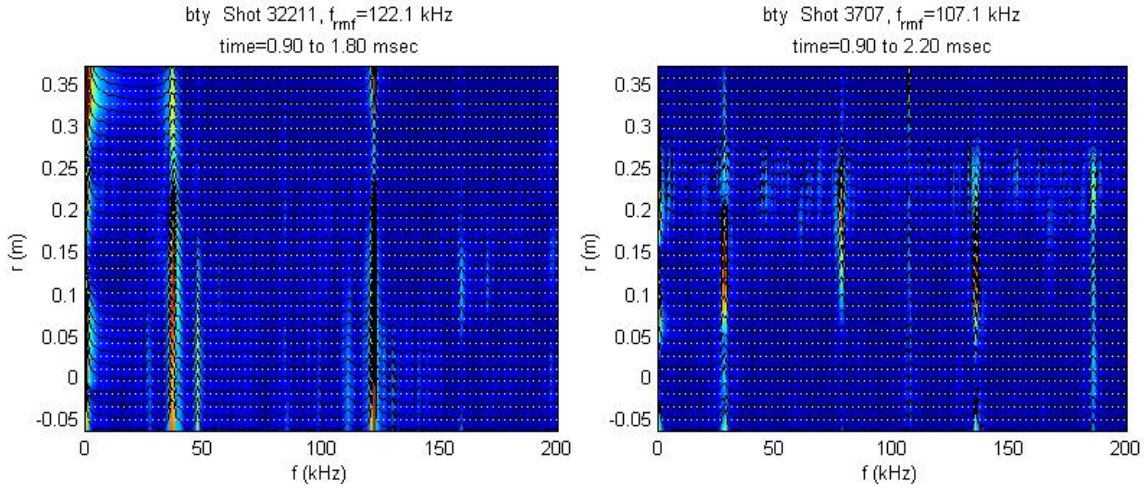

Figure 5.17: Frequency spectrum of B_y from the three-axis probe at the midplane. Even-parity (left) and odd-parity (right)

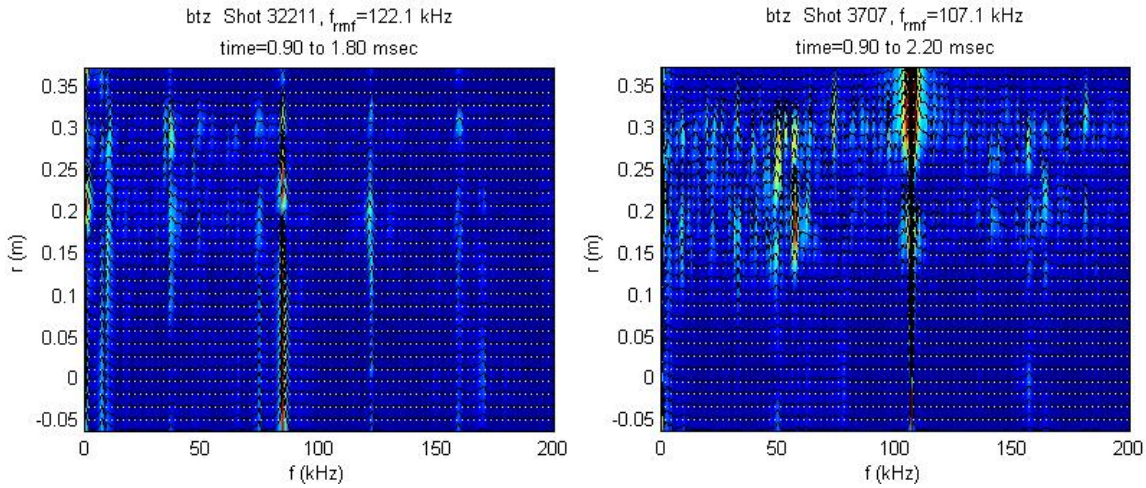

Figure 5.18: Frequency spectrum of B_z from the three-axis probe at the midplane. Even-parity (left) and odd-parity (right)

We can isolate the RMF frequency by applying a band-pass filter with a 20 kHz bandwidth at 122 kHz and 107 kHz for even- and odd-parity, respectively. Plotting the magnitude of the envelope of the RMF signal in the same manner as done with the average field data shows the general structure of the RMF, how it interacts with the FRC, and emphasizes that the effects of the RMF are three-dimensional. *Figures 5.19* and *5.20* show the amplitude of the RMF signal and include the flux contours calculated from the average field data so we can see the shape of the FRC. The color is the magnitude of the RMF envelope. The even-parity RMF structure in *figure 5.19* shows that the largest

contribution is from the RMF B_θ, which is generally confined to within the length of the RMF antennas and outside the radius of magnetic field null. The B_z component is produced by the RMF antenna return straps that wrap around the machine at z = +0.6 m and z = -0.6 m. The RMF B_r component is small compared to B_θ but appears outside the field null and has a small magnitude near the machine axis around the midplane.

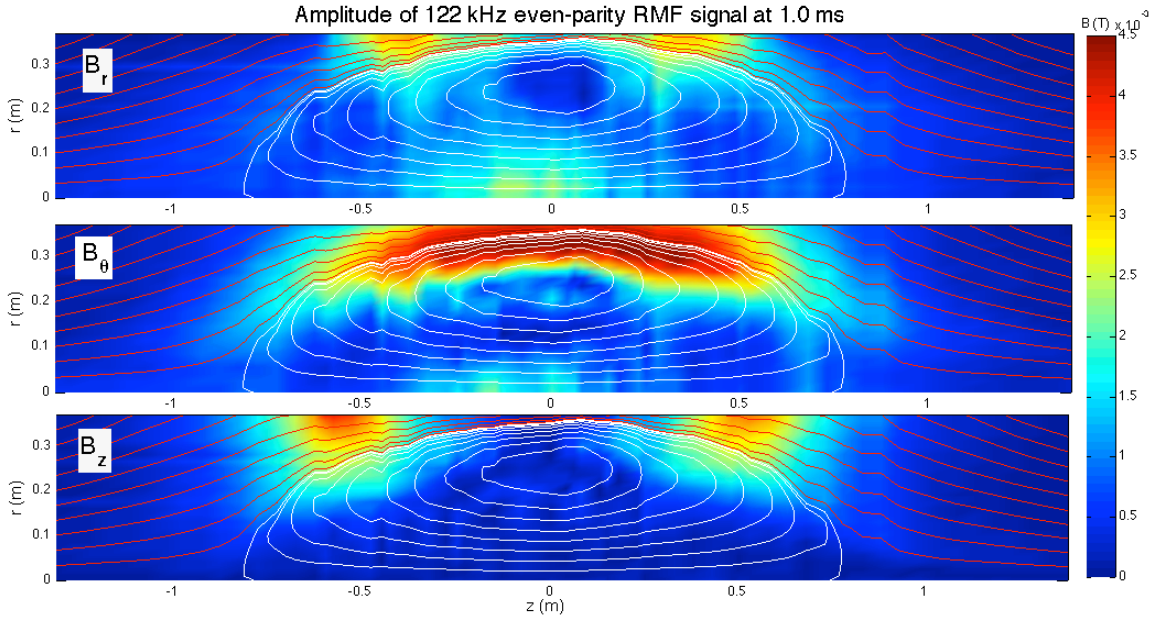

Figure 5.19: r-z map of the envelope of the even-parity RMF frequency data during the steady state period of the FRC

The RMF data from odd-parity in *figure 5.20* shows a very different structure. As expected, the amplitude of the RMF B_θ and B_r is small at the midplane while the RMF B_z peaks near 7 mT because the azimuthal antenna current is large there. The B_r signal is larger and present over a wider area. Perhaps most importantly, the RMF B_θ penetrates past the radius of the magnetic field null. This implies that a larger fraction of the electrons are co-rotating with the RMF in this region and there is more efficient current drive in the regions on either side of the midplane.

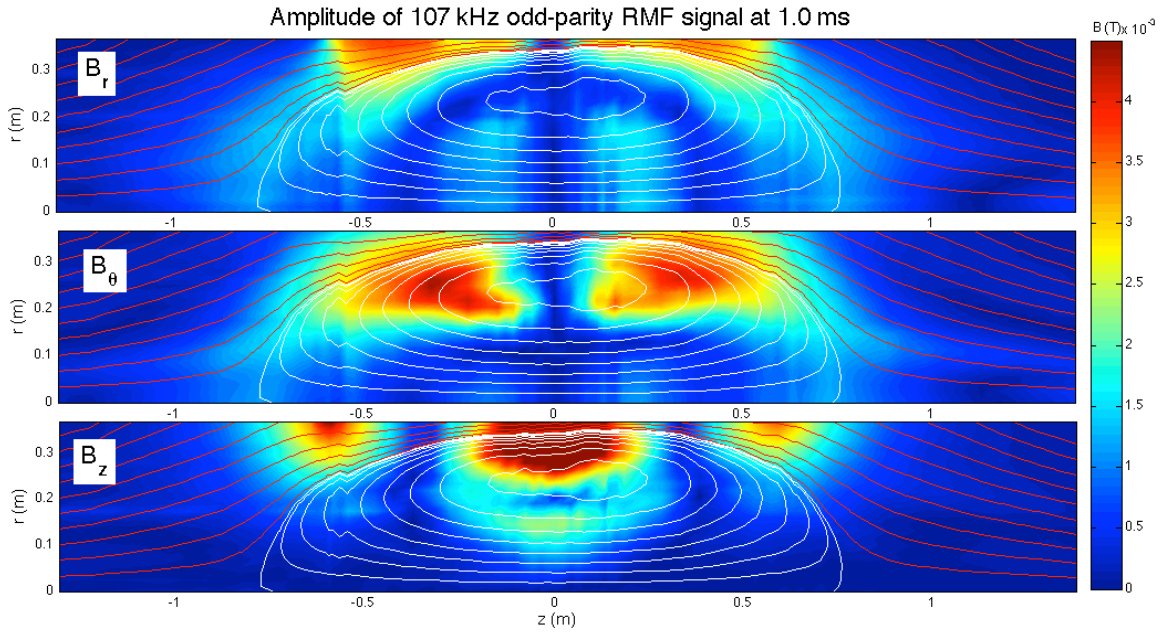

Figure 5.20: r-z map of the odd-parity RMF amplitude data during the steady state period of the FRC.

The magnitude of B_θ peaks near z = +/-0.3 m at the center of each half of the antennas. The three-axis probe took a measurement at -0.28 m; *figure 5.21* shows the radial profile of the RMF B_θ envelope with the average B_z field. As indicated by *figure 5.20*, the RMF signal peaks at 4.5 mT near the field null and still measures 1.2 mT at r = 15 cm, well inside the radius of the field null.

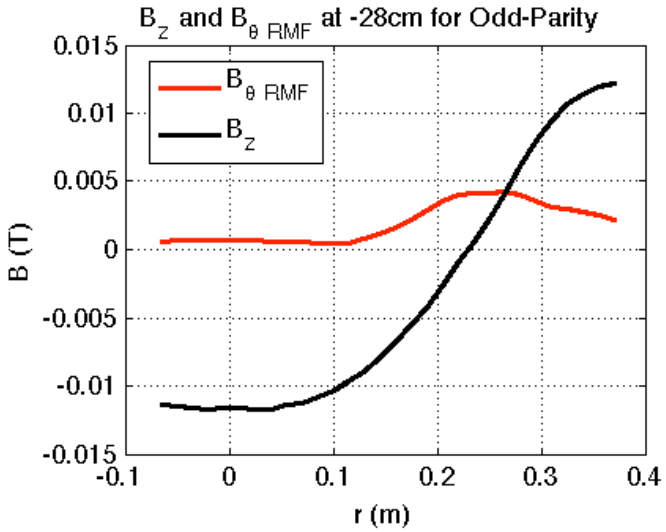

Figure 5.21: Radial profiles of RMF B_θ and steady state B_z for odd-parity at z = - 28 cm near the peak of the RMF

Section 5.5: Comparison to NIMROD simulation results.

NIMROD simulations performed on TCSU[**20**], as described in *chapter 2*, show general agreement with the experimental data. The steady state flux and RMF B_r boundary condition are specified for the simulation. The RMF B_θ and B_z boundary profiles are calculated self-consistently and depend on the plasma response. The RMF boundary conditions for the even-parity calculation are shown in *figure 5.22*.

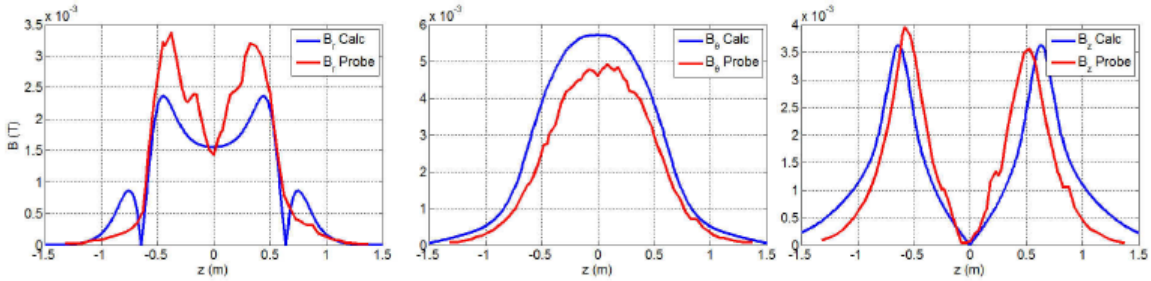

Figure 5.22: Radial boundary values of RMF components from even-parity measurements (red) and NIMROD calculation (blue)

The imposed B_r profile is slightly lower than the experimental value but the resulting B_θ profile is larger than the experimental data; increasing B_r to match would further increase B_θ. The profile shapes are in good agreement.

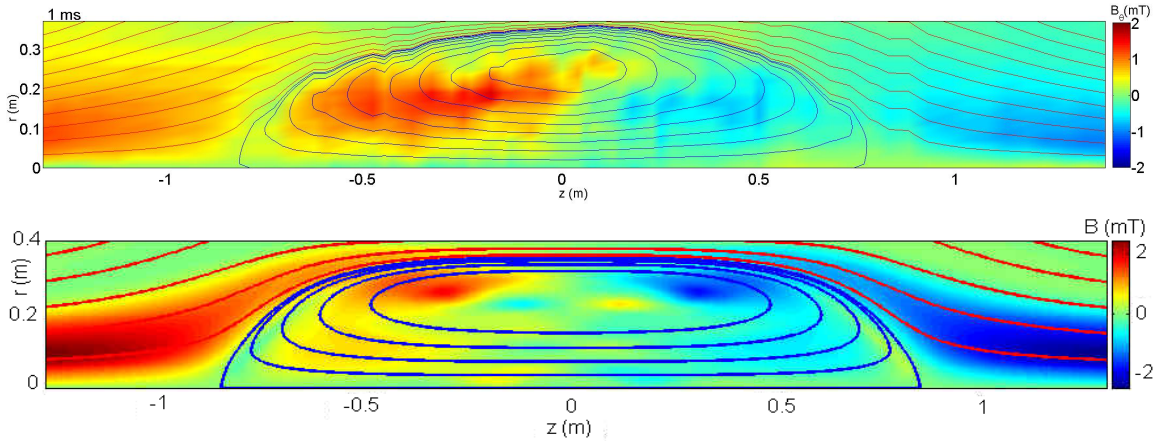

Figure 5.23: Flux contours and B_θ for the steady state even-parity FRC from the three-axis probe (top) and NIMROD simulation (bottom).

A comparison of the steady state FRC is shown in *figure 5.23*. The top plot in *figure 5.23* is the same r-z map of the three-axis probe data filtered with a 10 kHz low-pass filter as shown in *figure 5.12*. The overall shape of the flux contours is elliptical in the experiment but the simulation shows a racetrack shape. The simulation shows that the toroidal field inside the FRC peaks at 2 mT and is concentrated in the outer radii; the experimental data shows a wider distribution of toroidal field within the FRC and peaks at 1 mT.

The steady state toroidal field in the open field line region is due to the twisting of the open field lines that terminate on a conducting boundary. There is good qualitative agreement but again, the simulation shows a larger toroidal field in the open field line region. The magnitude of toroidal field is dependent on the resistivity, which is uniform in the calculations but is assumed to vary in the experiment.

The comparison of the axial boundary profiles for the odd-parity RMF configuration is plotted in *figure 5.24*. The B_r profile specified in the simulation has larger peaks but the total integrated flux matches. The simulation B_θ profile is larger by almost a factor of two but matches the shape of the experimental data. Curiously, the B_z profiles show different axial dependencies and the simulated profile is lower than in the experiment.

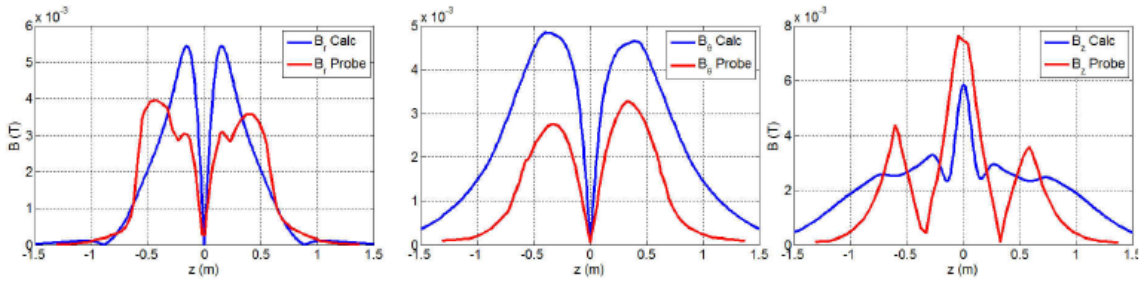

Figure 5.24: Radial boundary of the RMF components from the odd-parity simulation and experiment.

Despite the differences in the radial boundary profiles, the r-z map of the steady state FRC in *figure 5.25* shows remarkable agreement. There is a slight asymmetry in the flux contours of experimental data, which shows a slightly larger separatrix radius on the +z side. There is also a slight pinching of the flux contours at the midplane in the simulation, which is not seen in the experiment. However, both FRCs are elliptical, as opposed to the racetrack shape seen in the even-parity simulation. Both FRCs show the

distinct internal toroidal structure unique to the odd-parity RMF configuration. Again, the magnitude of the toroidal field is slightly larger in the simulation.

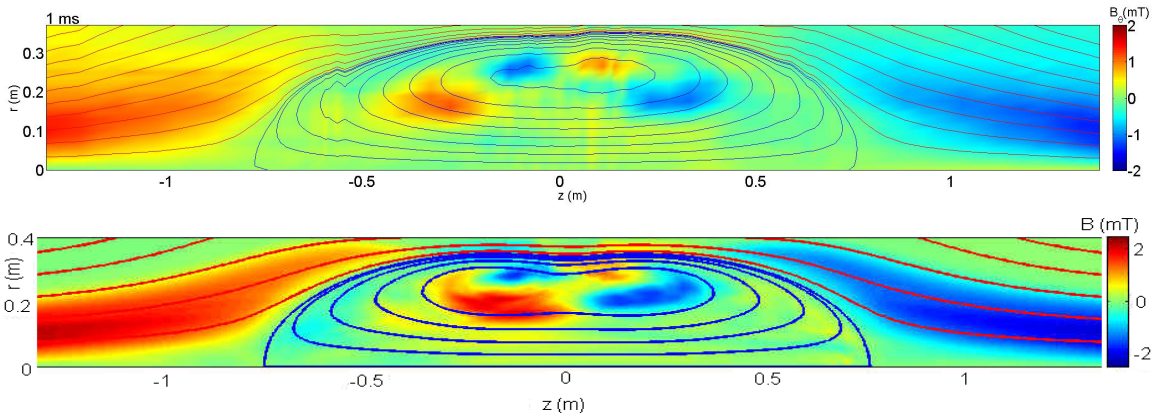

Figure 5.25: Flux contours and B_θ for the steady state odd-parity FRC from the three-axis probe (top) and NIMROD simulation (bottom).

Now that we have an overview of the behavior and structure of the even- and odd-parity FRCs, we can use the three-axis probe data to create a 3D image of the internal magnetic fields. The two RMF configurations form two FRCs with similar plasma parameters but using the internal probes we were able to detail important differences in the magnetic structure. For the first time, we measured the small steady state toroidal field, which changes sign across the midplane of the even-parity FRC but has a more complicated four-lobed structure in the odd-parity case. For the first time, we can investigate the axial variation of the RMF current drive. For the first time, we have the ability to expand our understanding of the ~30 kHz frequency that has been measured since the midplane probe was first installed on TCSU.

Chapter 6: **3D MAGNETIC FIELD VISUALIZATION**

We want to understand the 3D nature of the FRCs using the three-axis probe scans taken of the even-parity and odd-parity RMF current drive. There are important 3D effects from the antennas that are not described using the analytical model developed for RMF current drive, which can be captured using the three-axis probe data. We need to match the magnetic field frequency components that are consistent and repeatable in order to extrapolate our 2D r-z measurements in the θ direction. Previous efforts yielded a 2D r-θ slice of the magnetic field at the driven RMF frequency; now we add the mean-field component. Using the RMF component and the average field component we can compare the 3D magnetic field structure of the even- and odd-parity RMF configurations.

Using the three-axis probe we would like to get a 3D picture of the magnetic field inside TCSU. To do this we need to extrapolate our data in the θ direction to get a 2D r-θ picture at each axial position that measurements were taken and then connect the dots to get the 3D picture. Unlike previous work, we can do this with all three magnetic field components, B_x B_y, and B_z, and with more than just the RMF frequency component. To go from measurements of a radial chord to the 2D r-θ cross-section we need to know how the data varies azimuthally. Previously, it was assumed that data at the RMF frequency was driven by, or rotated with, the RMF and had the same sinusoidal θ dependence. Here, we make the same assumption and present evidence to show its validity.

This chapter details the method used to create 3D field line plots of even- and odd-parity RMF formed FRCs. First, I summarize the previous work on TCSU to create a 2D picture of the RMF field. Second, I demonstrate that a just a few frequency components can be used to represent the total magnetic field. Third, I show that despite eliminating other frequency components, using only the average field plus the RMF component yields a decent approximation of the total magnetic field. Fourth, I detail the calculation of the θ dependence and the necessary $\nabla \cdot B$ error correction. Lastly, I will present the 3D magnetic field line plots and show that odd-parity formed FRCs have field lines that make multiple internal transits while most field lines for even-parity driven FRCs transit the FRC only once.

Section 6.1: Previous efforts of 2D field construction.

In earlier work, a magnetic probe installed on the TCS device was used to measure the RMF field by using a radial chord of measurements of B_x. The magnetic probe installed at the midplane of TCS was a single axis of windings that could be rotated to measure B_x or B_z. Measurements taken while the probe was oriented to measure B_x were used to reconstruct the RMF field at the midplane. These results were compared to simulations run using a 2D r-θ RMF code tailored to TCS in order to gain insight into RMF penetration[**25**]. An example of RMF field lines inferred from TCS experimental results is shown in *figure 6.1*. As the RMF rotates it exerts a torque on the electrons, which rotate slightly slower than the RMF and drag the field lines in the opposite direction.

Figure 6.1: RMF field lines inferred from TCS experimental data [25]

The results from TCS helped expand our understanding of RMF penetration by visualizing the transfer of RMF torque to the electrons. However, this is only a two-dimensional r-θ representation of RMF current drive and the physics of RMF drive is fully three-dimensional.

In addition to the RMF frequency, we would like to capture the average value of each magnetic field component. The average field component is the slowly varying part of the field that yields the general magnetic structure and is assumed to be independent of

theta for the quiescent period of the FRC. The average field is calculated by applying a 10 kHz low pass filter to the magnetic probe data.

The frequency spectrum of each magnetic field component shows oscillations that contribute to the magnetic field structure. *Figures 6.2 – 6.4* show the even-parity frequency spectrum as a function of radius for B_x, B_y, and B_z, respectively. The data is taken from shot 32184 with the probe at z = +13 cm and shows the typical frequency activity measured within the even-parity driven FRC. Each magnetic field component has a peak at 37 kHz, 122 kHz, and near zero but little other activity. The RMF is the dominant oscillating field at most radii, however, around r = 8 – 18 cm the RMF does not penetrate and the 37 kHz signal becomes important. Analysis of the 37 kHz signal will be discussed in *chapter 7*.

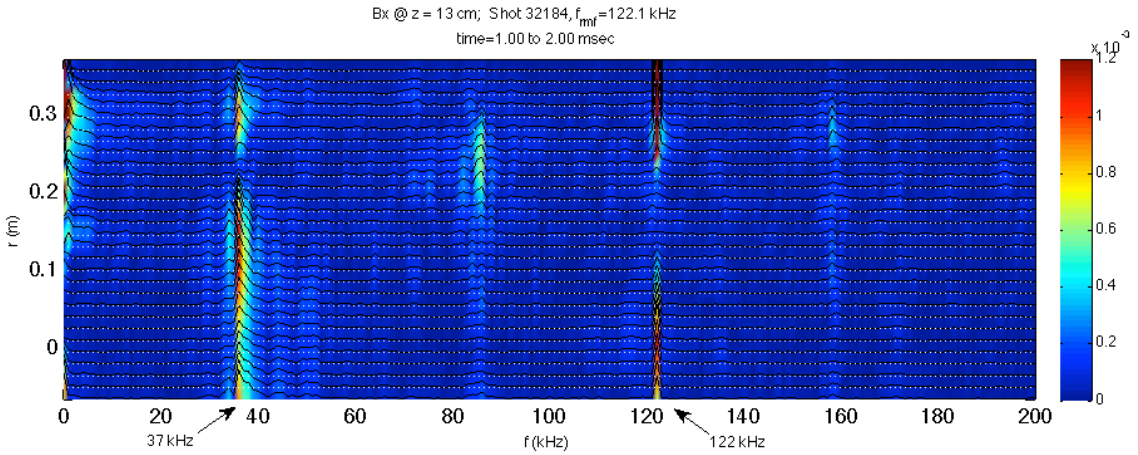

Figure 6.2: Frequency spectrum of B_x as a function of radius from three-axis probe at z = +13 cm

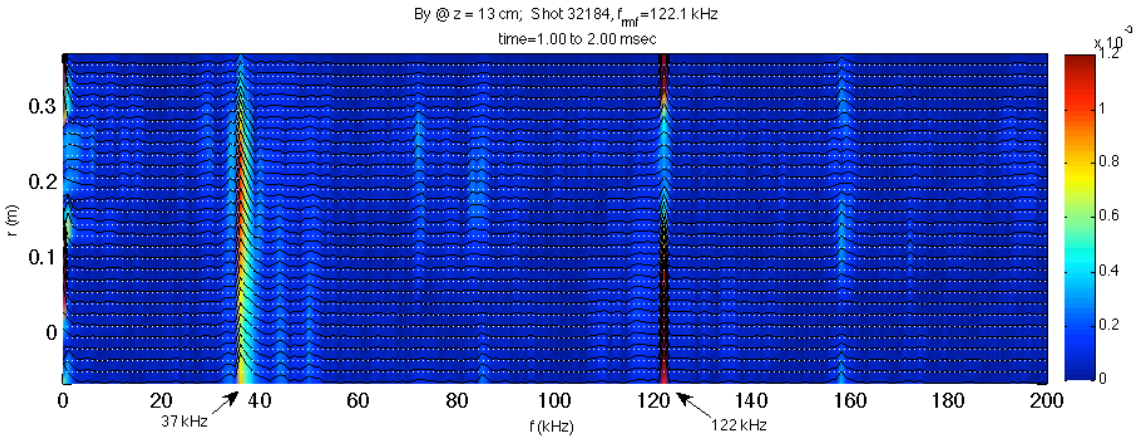

Figure 6.3: Frequency spectrum of B_y as a function of radius from the three-axis probe at z = +13 cm

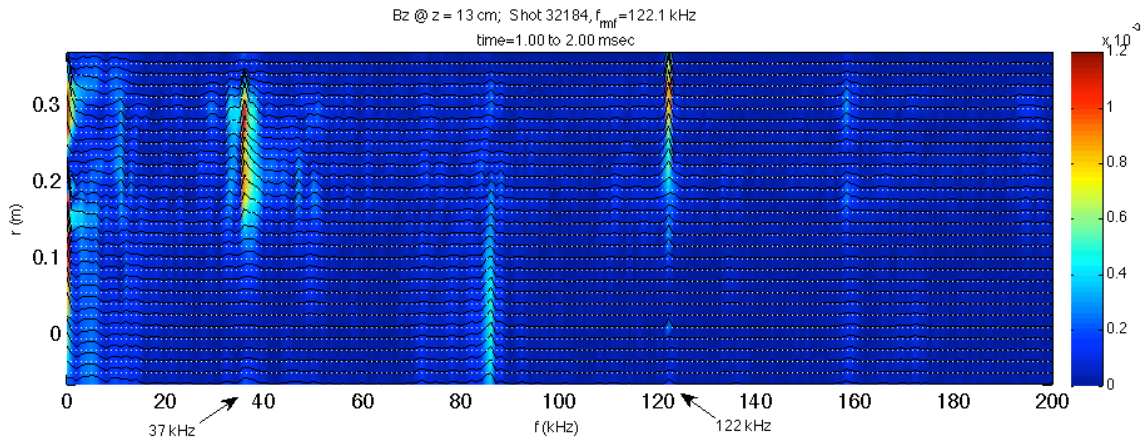

Figure 6.4: Frequency spectrum of B_z as a function of radius from the three-axis probe at z = +13 cm

Section 6.2: RMF signal has sinusoidal theta dependence

As in the work done on TCS, we use the RMF frequency component of B_x to generate a 2D r-θ picture of the RMF field lines. It was assumed that the data from a band-pass filter at the RMF frequency had a simple sinusoidal spatial dependence in the azimuthal direction because the RMF is a driven sin(θ) signal. Using the midplane probe, which measures the +y chord, and the three-axis probe, which measures the –y chord, we have a measurement of the full diameter of TCSU and can confirm the sin(θ) spatial variation of data at the RMF frequency. If data at the RMF frequency has a sin(θ) dependence, the B_x measurements at the same radius will have the same phase. Shots were taken with the midplane probe and three-axis probe separated by as little as 4 cm. To analyze the spatial dependence we use shot 32212 where the three-axis probe was positioned at z = -4 cm.

There are two y-locations where the midplane probe and three-axis probe each take a measurement. At y = 2 cm, each probe makes the same measurement; *figure 6.5* shows that the RMF component of B_x measured by the three-axis probe (btx04) at z = -4 cm is the same as the measurement from the midplane probe (bix05) at z = 0 cm.

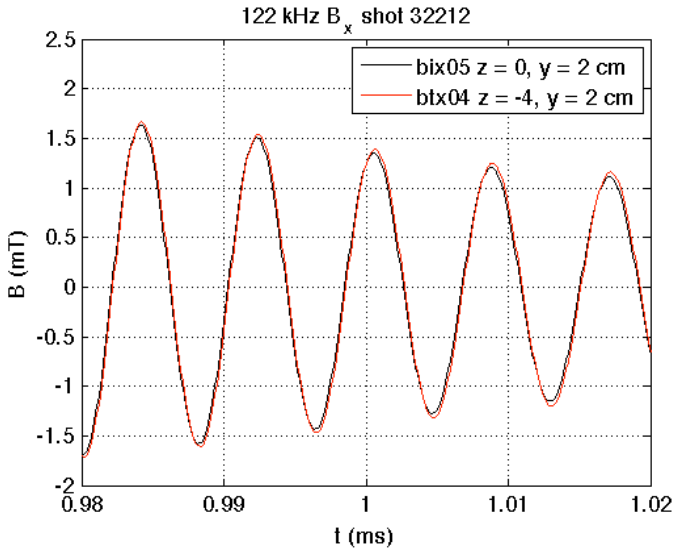

Figure 6.5: 122 kHz RMF component measured at y = 2 cm by the midplane probe (black) and three-axis probe at z = -4 cm (red)

The overlapping signals confirm that we can view this configuration as giving measurements of the full diameter of TCSU in order to analyze the phase matching between windings at the same radial locations.

The peak of the RMF signal is at r = 34 cm, just inside the separatrix. *Figure 6.6* shows the three-axis probe measurement at y = -34 cm (btx28) and the corresponding midplane probe measurement at y = 34 cm (bix21). Each B_x signal is the RMF component and the phases match.

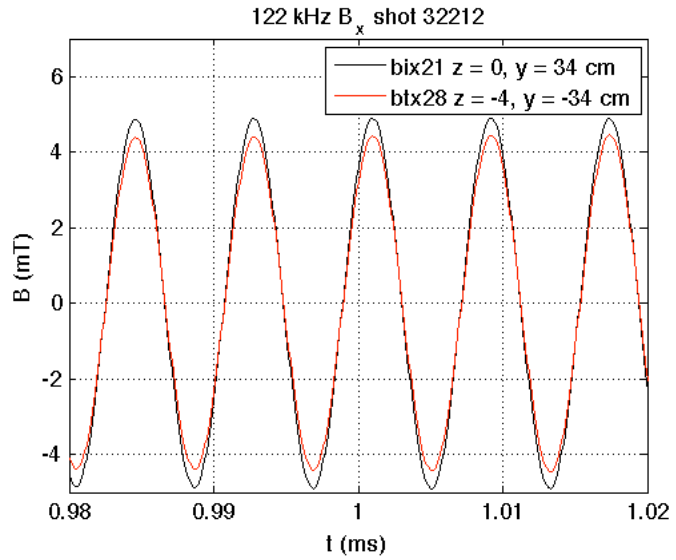

Figure 6.6: 122 kHz RMF component measured at r = 34 cm from midplane probe (black) and three-axis probe (red)

There is also a measurable RMF signal near r = 0 and there are probe loops on either side of the centerline at r = 2. This time we are looking at the midplane probe at y = -2 cm and the three-axis probe at y = +2 cm. The RMF magnitude is only 1.5 mT but we still see excellent phase matching between the two probes.

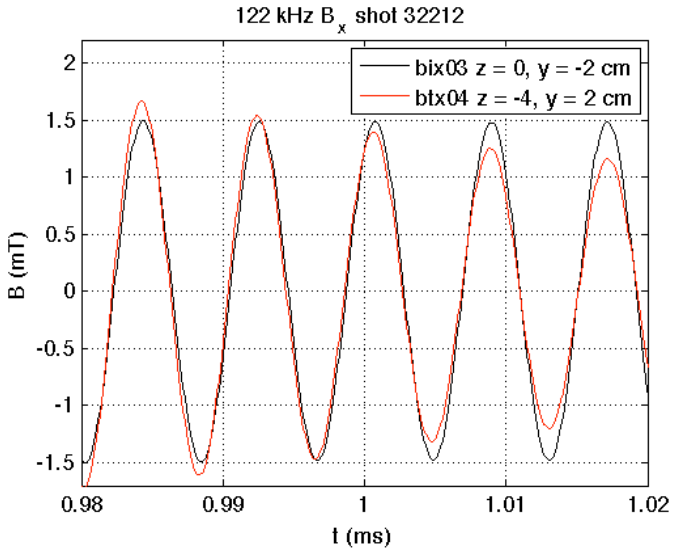

Figure 6.7: 122 kHz RMF component measured at r = 2 cm by the midplane probe (black) and three-axis probe (red)

Figures 6.5 – 6.7 confirm that the data at the RMF frequency has a simple sin(θ) spatial dependence. Additional comparisons made at other radial locations by extrapolating adjacent probe windings show the same result.

Also important to the 3D field reconstruction is the consistency of RMF signal; to get the 3D picture we need to see the same phase and magnitude measured by the stationary midplane probe on each shot. *Figure 6.8* shows the RMF component of the B_x measurement at y = 28 cm for multiple shots; the RMF is driven externally and has excellent repeatability.

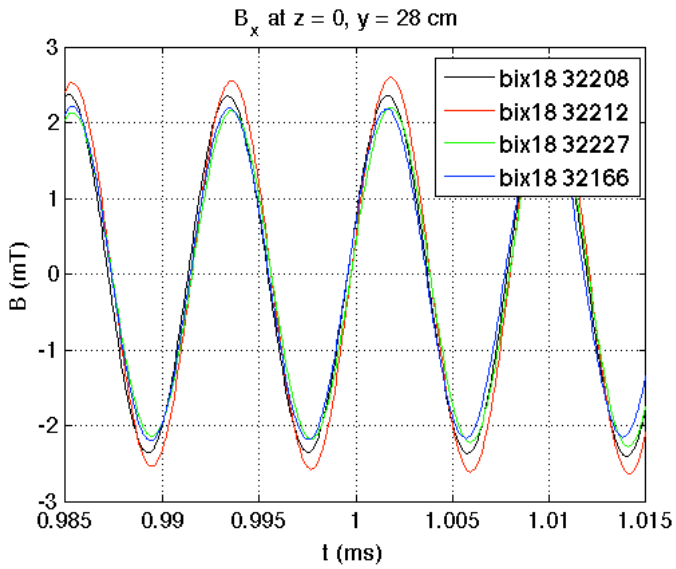

Figure 6.8: 122 kHz RMF component measured by midplane probe at y = 28 cm for multiple shots

Section 6.3: Theta dependence of 37 kHz signal

The frequency spectrum of each magnetic field component showed that in addition to the average field and the 122 kHz RMF oscillation there is also a measureable oscillation at 37 kHz that is important in describing the total magnetic field. We perform the same analysis as done with the 122 kHz RMF to see if the 37 kHz signal also has a sinθ spatial dependence. Again, we isolate the 37 kHz frequency using a band-pass filter at 37 kHz with a 20 kHz bandwidth and compare probe signals from the same radial location. The 37 kHz signal is strongest near the two probes at r = 16 cm. As with the data at the 122 kHz RMF frequency, there is good agreement in phase and magnitude, shown in *figure 6.9*, implying that the 37 kHz data also has a simple sin(θ) spatial dependence.

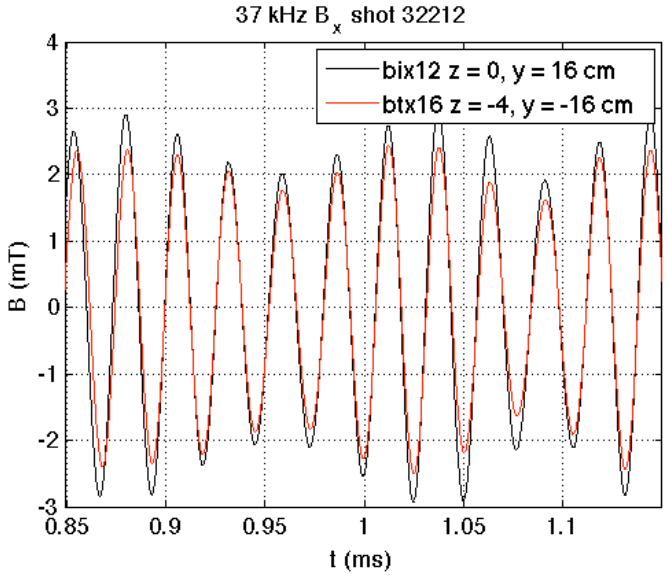

Figure 6.9: 37 kHz signal measured at r = 16 cm by midplane probe (black) and three-axis probe (red)

However, if we look at the 37 kHz signal at the midplane over multiple shots as in *figure 6.10*, we see that the 37 kHz signal is not consistent in phase or magnitude.

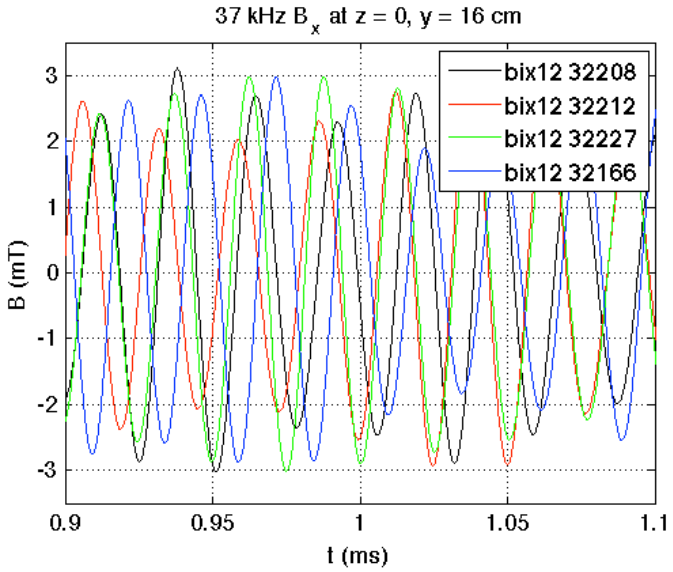

Figure 6.10: 37 kHz signal measured at the midplane for multiple shots

The 37 kHz signal has similar spatial behavior as the RMF signal; to gain further insight we analyze the 37 kHz signal assuming is has a sin(θ) spatial dependence. However, unlike the driven RMF signal, the behavior of the 37 kHz signal is not consistent between shots and cannot be included in the 3D field reconstruction. However,

the 37 kHz component is important in describing the FRC behavior and can be analyzed by looking at a 2D slice at any axial location. This analysis is presented in *chapter 7.*

Section 6.4: Simplified representation of total magnetic field

In order to form a 3D picture of the magnetic field structure we are going to represent the magnetic field as

$$B(t) = B_o(t) + B_{RMF}(t)$$

where $B_o(t)$ is the mean-field component from applying a 10 kHz low-pass filter and $B_{RMF}(t)$ is the RMF component from applying a band-pass filter with a 20 kHz bandwidth at the RMF frequency, either 122 kHz for even-parity or 107 kHz for odd-parity. The low frequency part of the field is axisymmetric and independent of θ. The RMF component is driven with a known frequency and sinusoidal θ dependence.

Figures 6.11 – 6.13 show an example of the magnetic field represented with two frequency components compared to the unfiltered signal. The figures show B_x, B_y, and B_z, respectively, just outside the separatrix at the midplane. The unfiltered signal is shown in black; the simplified representation is shown in red. The general behavior is captured but additional oscillatory behavior is lost.

Outside the separatrix, the B_x signal, *figure 6.11*, is almost entirely due to the 122 kHz RMF. The B_y signal in *figure 6.12* is well described by the RMF but also has a contribution from the 37 kHz component, seen in the peaks near +/-2.5 mT. Both of these signals oscillate around 0 and have little contribution from the low-frequency spectrum.

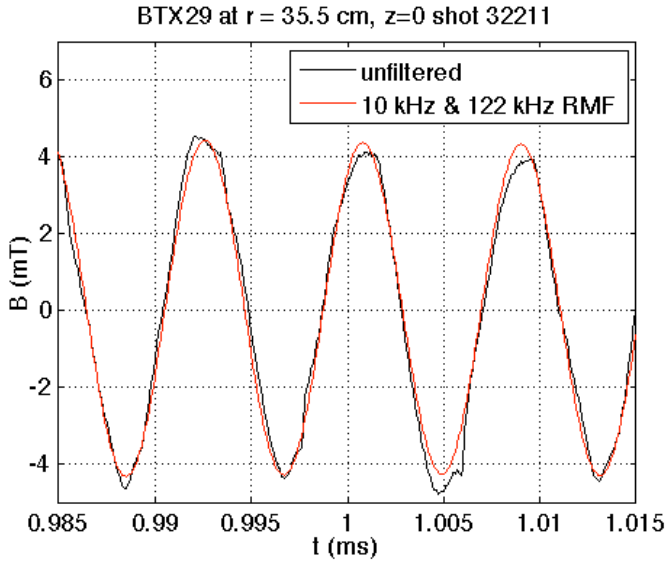

Figure 6.11: Midplane B_x outside the separatrix comparing the average field + rmf component (red) to the unfiltered data (black)

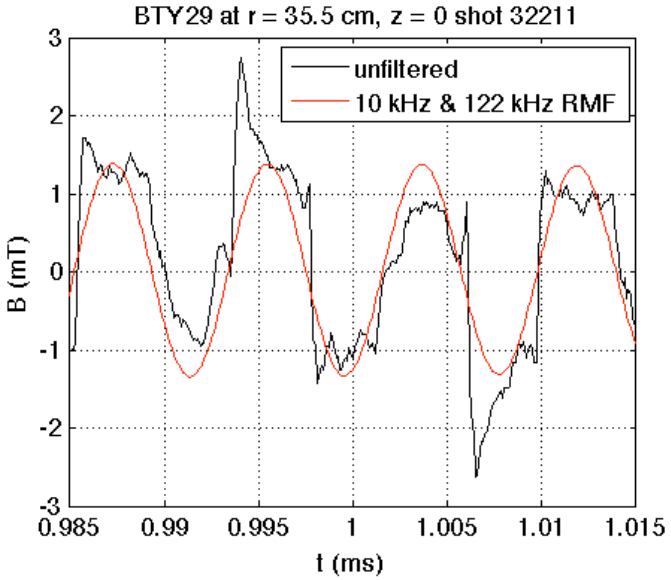

Figure 6.12: Midplane B_y outside the separatrix comparing the average field + RMF component (red) with unfiltered data (black)

At the midplane, the bias magnetic field points in the z-direction. Remember that the measurement of B_z outside the separatrix is used for B_e, the field external to the FRC after the initial bias field is compressed. The axial magnetic field, B_z, is well described using the low-frequency component. *Figure 6.13* shows the unfiltered measurement in black for the lifetime of the FRC with the 10 kHz + 122 kHz shown in red. Zooming in

on a smaller time period shows the details of higher frequency oscillations on top of the steady field. The 122 kHz RMF component captures a small portion of the oscillating field. Other components of the oscillating field are much smaller than the magnitude of the average field during the quiescent period of the FRC that we are focusing on in all of our detailed analysis.

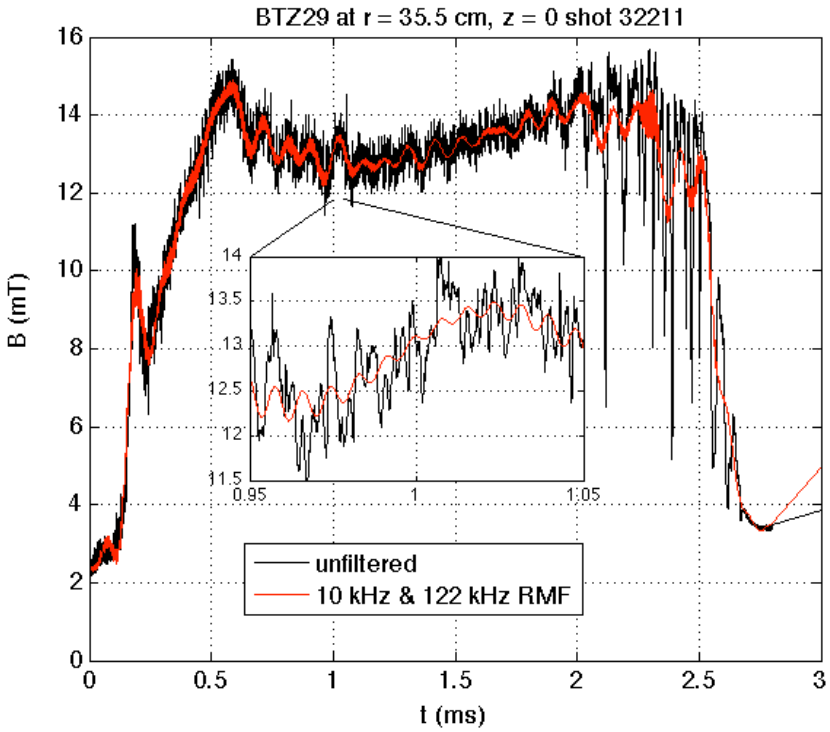

Figure 6.13: Midplane B_z showing the average field + 122 kHz RMF (red) with unfiltered data (black).

Section 6.5*:* Azimuthal extrapolation of probe measurements

In order to get a 3D picture of the magnetic field structure, we are representing the total magnetic field with the low frequency and RMF frequency components. In doing so, we are throwing out all other information about magnetic field oscillations that are important to the 3D nature of the FRC, such as the 37 kHz signal. However, we can still gain an understanding of how the RMF affects the 3D structure of the FRC, especially though a comparison of the even- and odd-parity RMF current drive.

To form the 3D picture, first we need to extrapolate our single radial chord of probe measurements in the θ direction. For the low-frequency portion of the data we assume that the field does not vary as a function of θ so this extrapolation is trivial. The RMF component has a sinusoidal variation described as

$$B_i^{RMF}(\theta,t) = \tilde{A}_i(t)\cos(\theta + \phi_i(t) + \pi/2) \qquad (6.1)$$

where i = r,θ,z, $\tilde{A}(t)$ is the amplitude of the RMF component, and ϕ(t) is the instantaneous phase of the oscillating signal. Remember that the probe measures the magnetic field in the x, y, and z directions but the probe orientation ensures $B_r = -B_y$ and $B_\theta = B_x$.

To calculate the amplitude and phase of the RMF component we use the Hilbert transform**[26]**. The transform shifts the phase of the signal by 90^o; i.e. our signal is ~cos(ωt) so its Hilbert transform is ~sin(ωt). The amplitude and phase of the original RMF signal are calculated using:

$$\text{Amplitude} = \tilde{A}(t) = \sqrt{H[u(t)]^2 + u(t)^2}$$

$$\text{Phase} = \phi(t) = \arctan\left(\frac{H[u(t)]}{u(t)}\right)$$

where u(t) is the band-pass filtered data at the RMF frequency, H[u(t)] is the transformed data, and the arctangent is given on the interval (-π,π].

The calculation we use gives the instantaneous phase with respect to the peak of the original signal, which is why we use Cosine to describe the spatial variation; we need $B^{RMF}(t) = \tilde{A}(t)$ when ϕ = 0 and θ = 0. However, in the plane of the TCSU cross-section, the probe is located at θ= -π/2; to match the probe data to the extrapolated data at the correct position on the x-y plane, we added a shift of π/2.

Using *equation 6.1* we calculate the RMF as a function of θ for each of the probe windings at each axial location that measurements were taken. We add the steady field, which is independent of θ, and look at the vector field from B_θ and B_r to begin to understand how the magnetic field varies in space. The vector field at the midplane, shown in *figure 6.14*, shows $B_\theta B_r$ vectors at the midplane when the B_x probe at the edge measures the peak of the RMF signal. The RMF is in the horizontal direction.

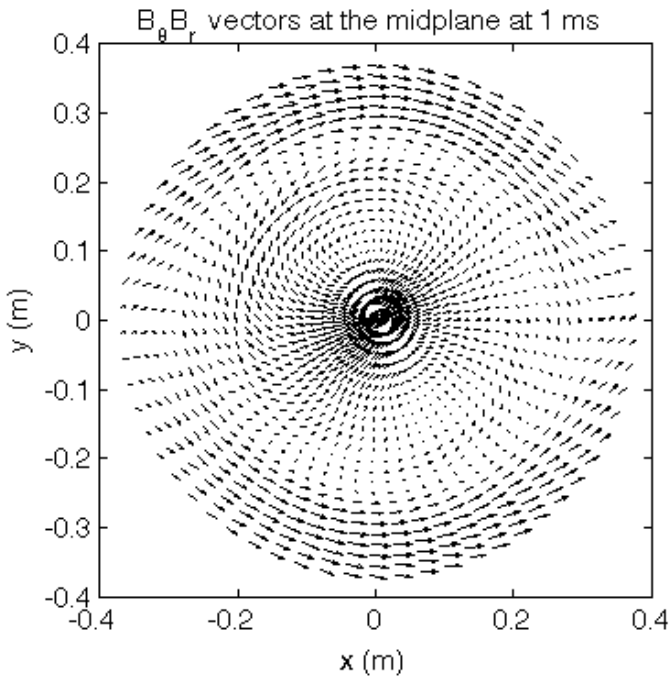

Figure 6.14: $B_r B_\theta$ vector field at the midplane

Looking around the outer edge of the cross-section, the magnetic field enters the domain around x = - 0.4 m, y = 0, circles around the machine, and exits at x = +0.4 m. However, to understand the overall behavior, we need to look at the magnetic field in 3D.

To create the 3D representation of the even- and odd-parity FRCs, we use a program called VisIt, a 3D visualization tool developed by the Department of Energy (DOE) Advanced Simulation and Computing Initiative (ASCI). VisIt can read a VTK file written by Matlab containing a list of spatial grid points and the corresponding magnetic field vector. Our spatial grid consists of 25 radial points, 64 azimuthal points, and 65 axial points (for the 122 kHz long mirror even-parity) or 76 axial points (for 107 kHz odd-parity). These points are converted to Cartesian coordinates for input to VisIt.

The VisIt program allows us to visualize the magnetic field streamlines. Beginning at a specified point, the streamline follows the trajectory of the magnetic field. Small errors in the magnetic field result in a non-zero divergence, which causes the streamlines to spiral toward the magnetic field null. This is easily visible when looking at the average field data from applying the 10 kHz low-pass filter. *Figures 6.15* and *6.16* show two views of the same average field streamline launched from the 'ball' located at

x = 0.35 m, y = z = 0 that spirals toward the magnetic null. This effect is non-physical; a divergence free steady state magnetic field would form a closed flux surface.

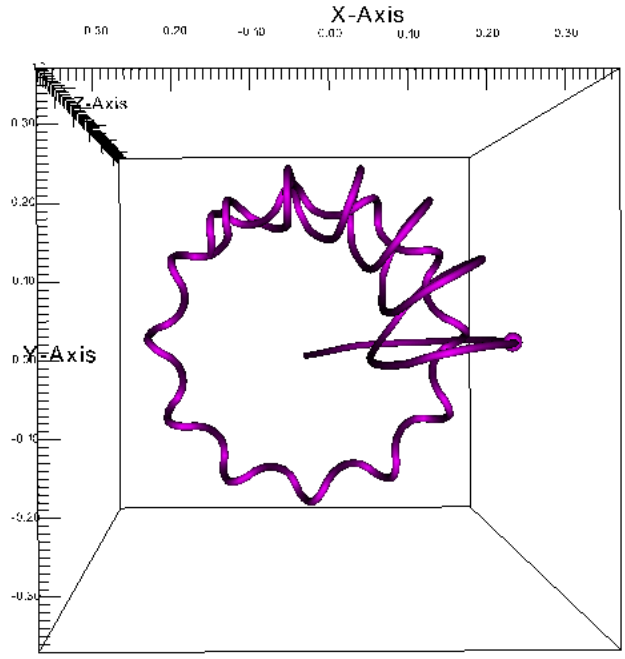

Figure 6.15: Magnetic field streamline calculated using the average field from applying a 10 kHz low-pass filter showing a nonzero divergence

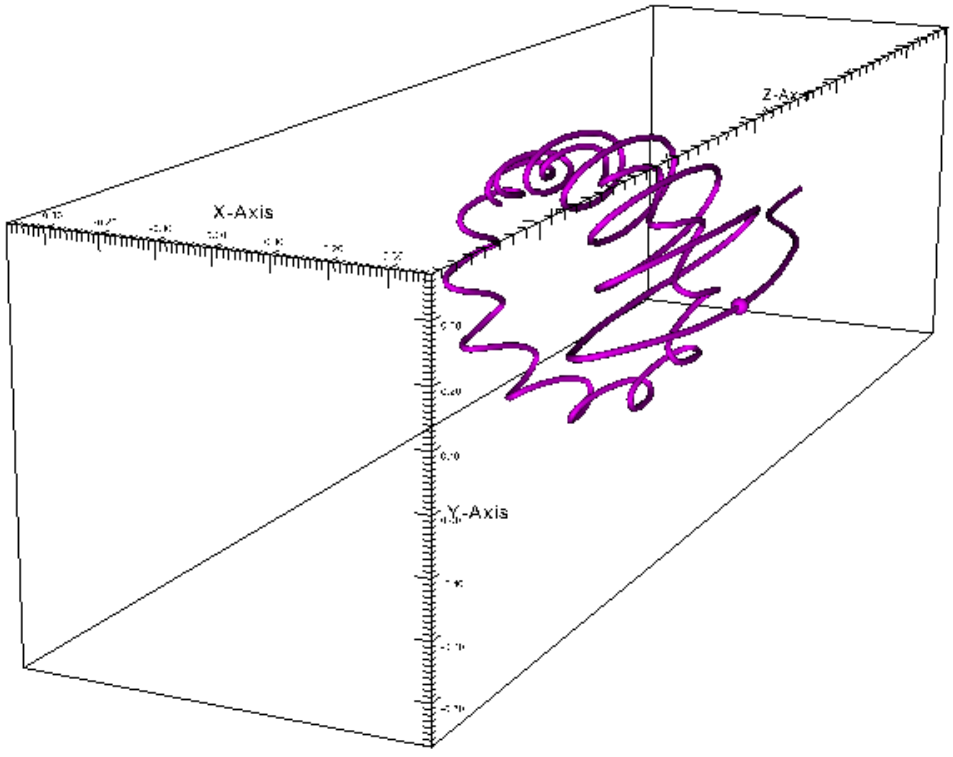

Figure 6.16: Oblique view of field line created from the steady state magnetic field component

Section 6.6*:* $\nabla\cdot B$ error correction

In order to properly visualize the 3D field, we must correct small errors in the steady state portion of the magnetic field so that the divergence of the steady field is zero.

Imperfect repeatability and small measurement error contribute to the nonzero divergence of the magnetic field. Applying a correction to the steady field component is straightforward and will yield a better representation of the 3D field. We are not correcting divergence errors in the RMF component. First, to correct for errors in the reproducibility of the shots, we can smooth the data by using $B(z_i) = 0.5B(z_i) + 0.25(B(z_{i+1})+B(z_{i-1}))$ along the axial extent. Second, We correct the divergence errors by using the measured data to calculate the flux and then re-calculate B_z and B_r from the flux so that we maintain $\nabla\cdot B = 0$. The axisymmetric θ component does not contribute to the divergence so the correction will be applied to B_r and B_z only.

The divergence of the magnetic field in cylindrical coordinates is given by,

$$\nabla\cdot B = \frac{1}{r}\frac{\partial}{\partial r}\left(rB_r\right) + \frac{1}{r}\frac{\partial B_\theta}{\partial \theta} + \frac{\partial B_z}{\partial z} \tag{6.2}$$

The flux is calculated using,

$$\psi = \int rB_z(r)dr \tag{6.3}$$

Given the definition of flux, $B_z(r)$ and $B_r(z)$ are defined as

$$B_z = \frac{1}{r}\frac{\partial \psi}{\partial r} \tag{6.4}$$

$$B_r = -\frac{1}{r}\frac{\partial \psi}{\partial z} \tag{6.5}$$

I use 2nd order accurate difference methods to calculate the derivatives for *equations 6.4* and *6.5*.

The B_z field for the first probe at r = 0.5 cm is given by the 2nd order accurate forward difference equation:

$$B_z(first) = \frac{-\psi(r_{i+2},z,t) + 4\psi(r_{i+1},z,t) - 3\psi(r_i,z,t)}{r_i(2\Delta r)}.$$

The B_z field for the outermost probe winding at r = 37 cm is given by the 2nd order accurate backward difference equation:

$$B_z(last) = \frac{3\psi(r_i,z,t) - 4\psi(r_{i-1},z,t) + \psi(r_{i-2},z,t)}{r_i(2\Delta r)}.$$

The 2nd order accurate centered difference is used to calculate the other elements.

$$B_z(r_i) = \frac{\psi(r_{i+1},z,t) - \psi(r_{i-1},z,t)}{r_i(2\Delta r)}.$$

The same equations are used to calculate $B_r(z)$ with the steps taken in the z-direction.

Generally, the errors in B_r and B_z are small. To evaluate the error correction we see if the B_rB_z vectors are aligned with the flux contours calculated using the original B_z data. *Figure 6.17* shows the full r-z plane with flux lines and B_rB_z vectors; the original vectors are shown in red with vectors using the new data shown in red. Generally, the red and green arrows overlap and are aligned with the nearest flux contour. Focusing on a section of the FRC where the largest errors occur illustrates the small but important correction made to the data.

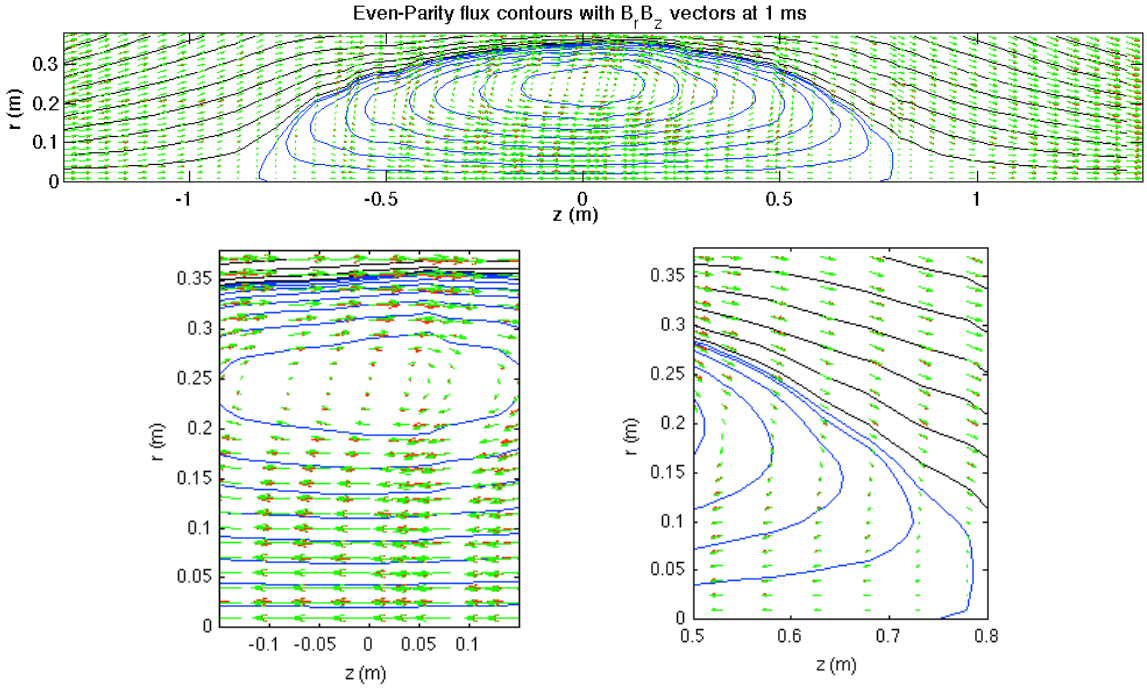

Figure 6.17: Original BrBz vector field shown in red with the divergence free correction shown in green for the full axial extent (top) and two subsections showing additional detail (bottom).

Section 6.7: Magnetic field streamlines of 122 kHz even-parity formed FRC

Minimizing errors in the divergence of the average field yields a better picture of the general structure of the FRC. Using the new data to create *figure 6.18***,** we see that the streamline launched from the same point as in *figure 6.16*, (0.35, 0.0, 0.0), results in the beginning of a flux surface.

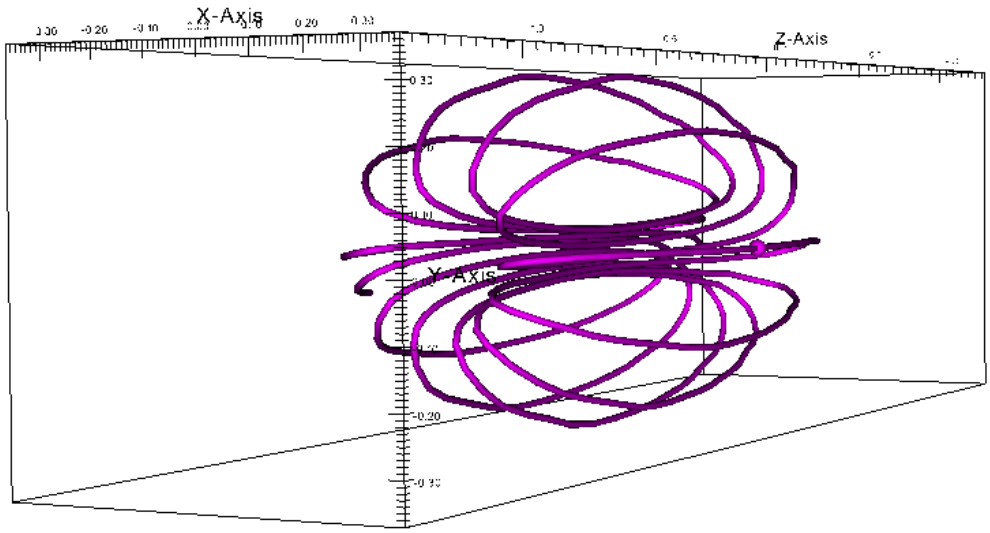

Figure 6.18: Divergence free steady state field streamline launched at (0.35,0,0)

However, the RMF tears open flux surfaces. The same trace shown above opens up when the RMF data is included. A streamline launched from the same point, (0.35, 0, 0), in *figure 6.19* quickly leaves the domain. The RMF field is pointing in the x-direction; the plot is oriented so that the RMF is vertical. There is an S-shaped field line that enters the domain under the RMF antenna, wraps around the end of the FRC to continue along the centerline of the machine and wrap around to exit under opposite side.

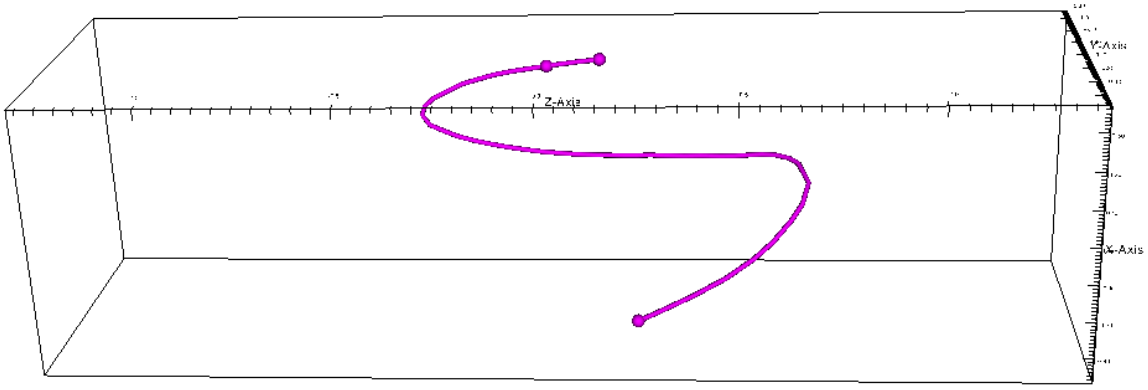

Figure 6.19: Magnetic field streamline calculated using divergence free steady state magnetic field plus the 122 kHz RMF component launched at (0.35,0,0)

This S-shaped field line is a primary feature of the even-parity RMF current drive. Field lines that originate within FRC near the separatrix or centerline generally exit the domain after transiting an s-shaped path; *figure 6.20* shows multiple field lines launched at the midplane inside r = 0.1 m that exhibit this behavior.

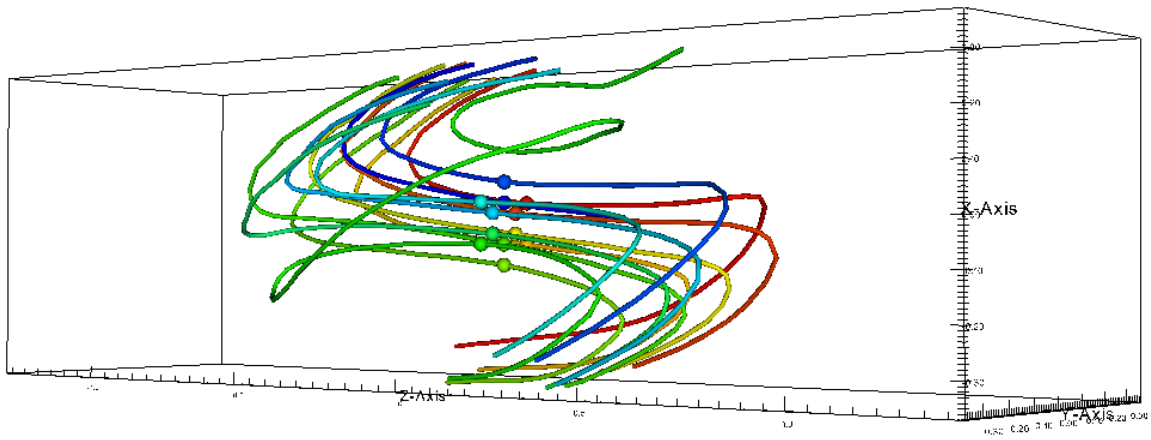

Figure 6.20: Multiple field lines launched within r = 0.1 m at the midplane

However, field lines launched closer to the field null, around $0.2 < r < 0.3$ m, can execute multiple transits of the FRC. In *figure 6.21* six streamlines were launched outside the field null at r = 0.3 m, each at a different point in θ. These are some of the few field lines that connect the inside of the FRC to the open field line region and contribute to the torque transfer to the jet, as discussed in *chapter 8*.

Figure 6.21: Magnetic field lines launched at r = 0.3 m

The experimental field lines exhibit similar behavior to the magnetic field lines generated using the results from the NIMROD simulation[**20**]. *Figure 6.22* shows streamlines launched from a ring at the midplane with a ball marking the intersection with the simulation boundary. The launch radii vary from 0.03 m at the top, 0.1, 0.2, 0.3, and 0.35 m in the last figure. *Figure 6.23* shows the same plots for the experimental data.

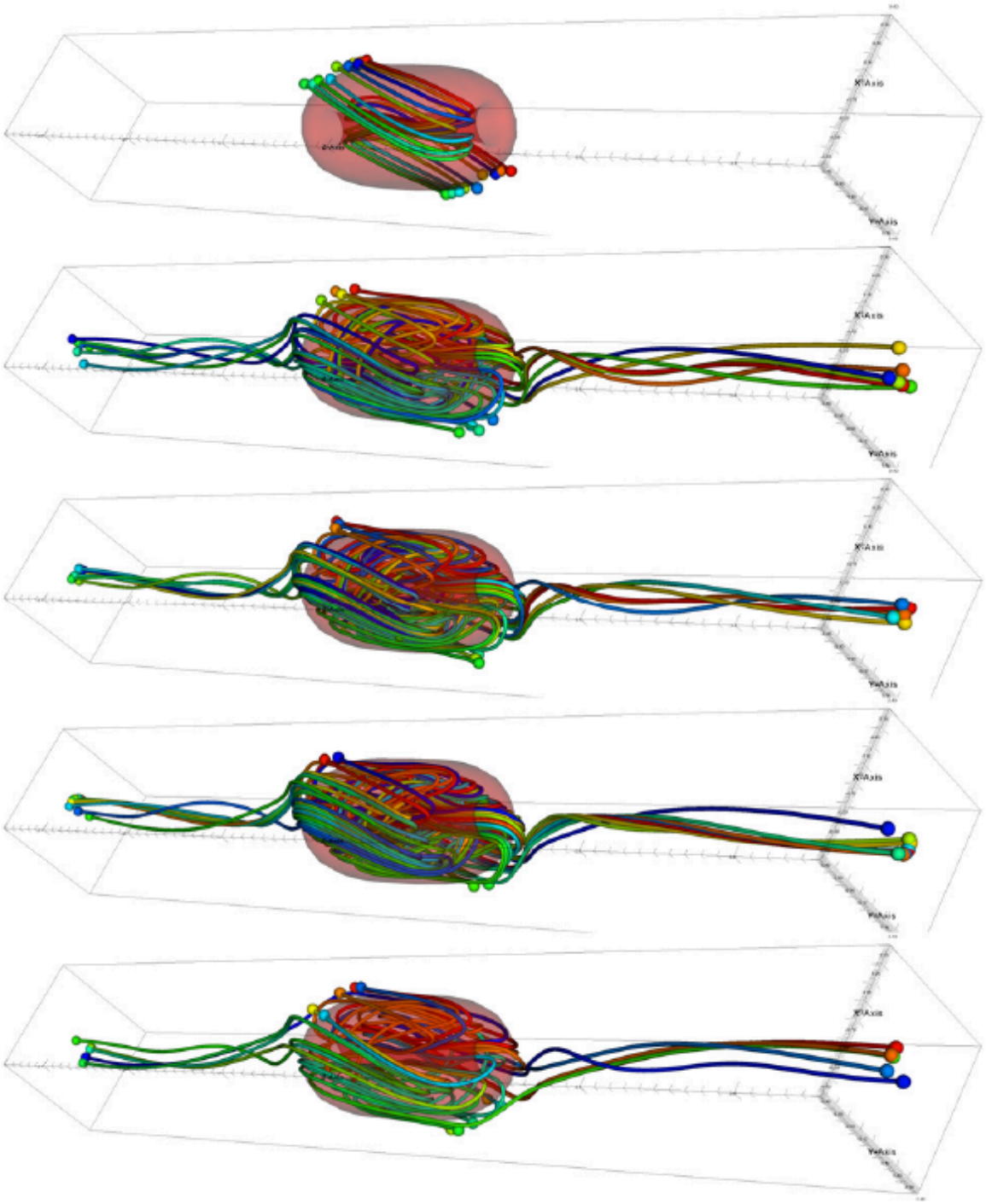

Figure 6.22: Three-dimensional images of magnetic field lines and a partially transparent pressure for an even-parity NIMROD calculation. In each plot, 10 field lines are launched from a circle of radius 0.03, 0.10, 0.20, 0.30, and 0.35 m (top to bottom) [20]

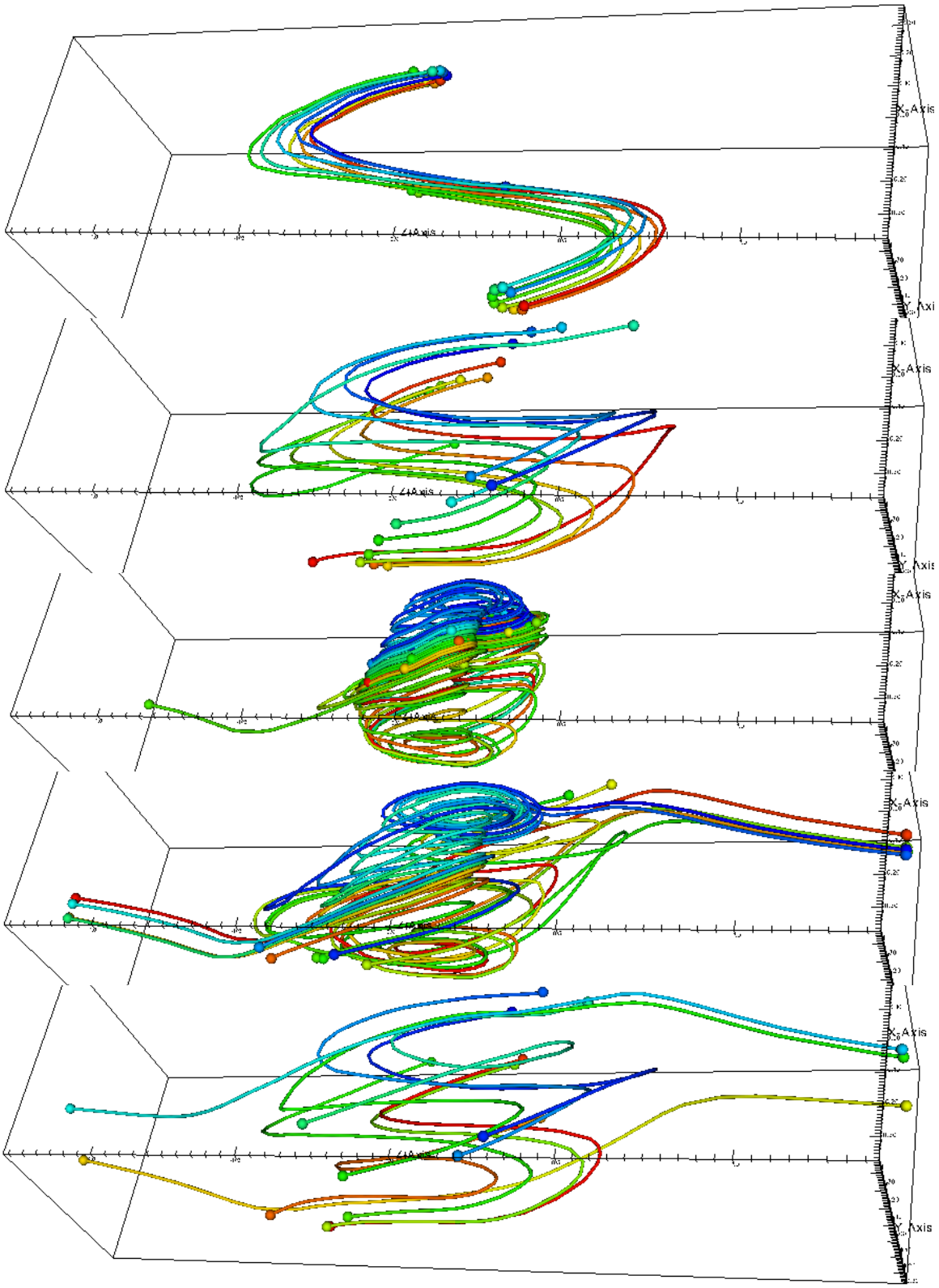

Figure 6.23: Experimental magnetic field lines from even-parity RMF driven FRC. In each plot, 10 field lines are launched from a circle of radius 0.03, 0.10, 0.20, 0.30, and 0.35 m (top to bottom)

The two sets of field line plots in *figures 6.22* and *6.23* show that many field lines enter and exit through the radial wall under the RMF antennas. The simulation has a number of field lines that transit the FRC before going past the x-point to terminate at the end walls of the simulation. In the experiment, most field lines that pass through the end of the domain wrap around the ends of the FRC to pass through the radial boundary under the RMF antenna. *Figure 6.24* shows field lines launched from the ends of the probe extent within a square grid centered at the machine axis; only one field line connects the two ends though the FRC while the rest intersect with the radial boundary under the RMF antenna.

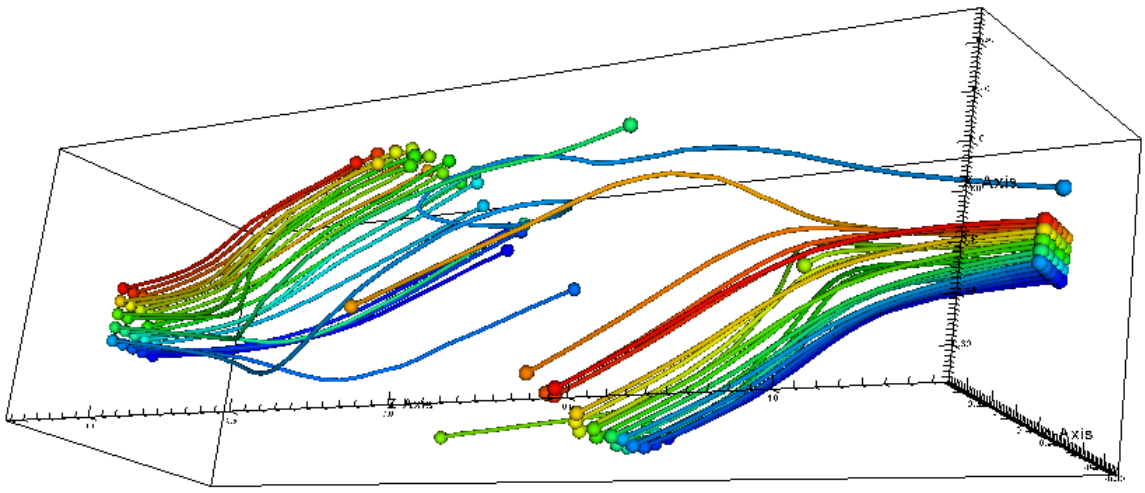

Figure 6.24: Magnetic field lines launched from the ends of the experimental domain pass through the quartz wall of the formation chamber

Section 6.8: Odd-Parity RMF driven FRC field lines

So far, I have shown the analysis of the magnetic field structure of the 122 kHz even-parity RMF driven FRC. However, the same analysis applies to the 107 kHz odd-parity FRC. The frequency spectrum of the odd-parity data, *figure 6.25*, has the same behavior seen in the even-parity case with the peak frequencies shifted because of the different RMF frequency. The dominant frequency peaks are still at the RMF frequency, now 107 kHz, and below 10 kHz. *Figure 6.25* shows the spectrum of the B_x data at $z = -28$ cm, when the probe was under the center of one half of the RMF antenna.

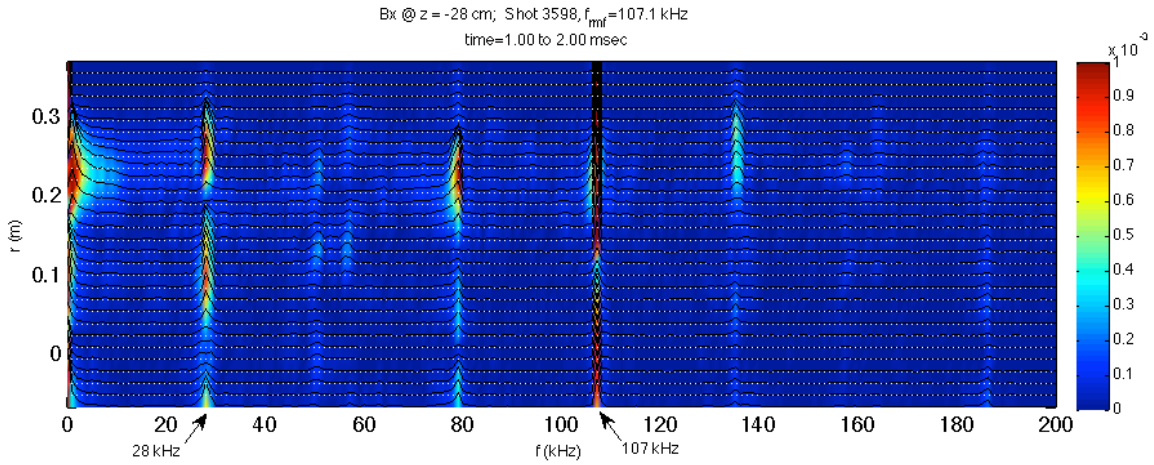

Figure 6.25: Frequency spectrum of Bx as a function of radius for the odd-parity driven FRC at z = -28 cm

The odd-parity driven FRC has a peak at 28 kHz that corresponds to the peak at 37 kHz in the even-parity case. Again, the 28 kHz signal is largest where the RMF does not penetrate. As in the even-parity formed FRC, we cannot include the 28 kHz signal in the full 3D picture of the FRC because of variability in phase and magnitude between shots.

Using the same method to correct divergence errors and extrapolate the odd-parity data in the θ direction we generate 3D plots of the magnetic field streamlines for the odd-parity driven FRC. *Figure 6.26* shows the corrected average field data from applying the 10 kHz low-pass filter. Field lines launched at the midplane from a radius of 0.04 m trace out the shape of the FRC, which is very similar to the results for even-parity in *figure 6.18*.

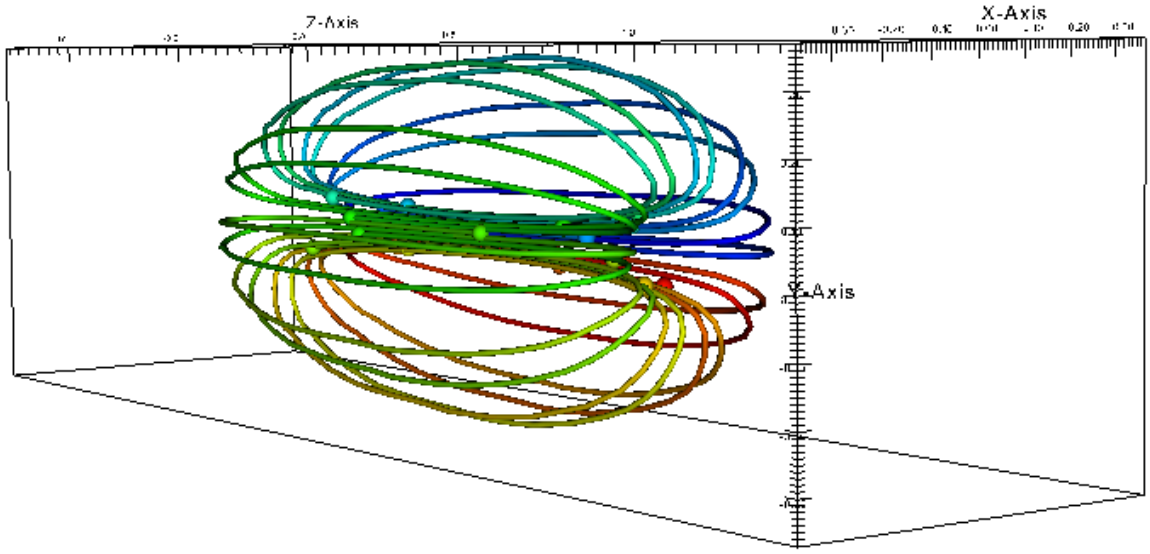

Figure 6.26: Odd-parity average field streamlines launched from the midplane at r = 0.04 m show the general shape of the FRC.

It has been theorized that the odd-parity RMF configuration allows for the possibility of maintaining magnetic field line closure[**6**]. *Figure 6.27* shows the streamline launched from (0.34, 0, 0), just inside the separatrix. Instead of having an s-shaped transit, as observed for even-parity, we have a field line that executes multiple transits of the FRC.

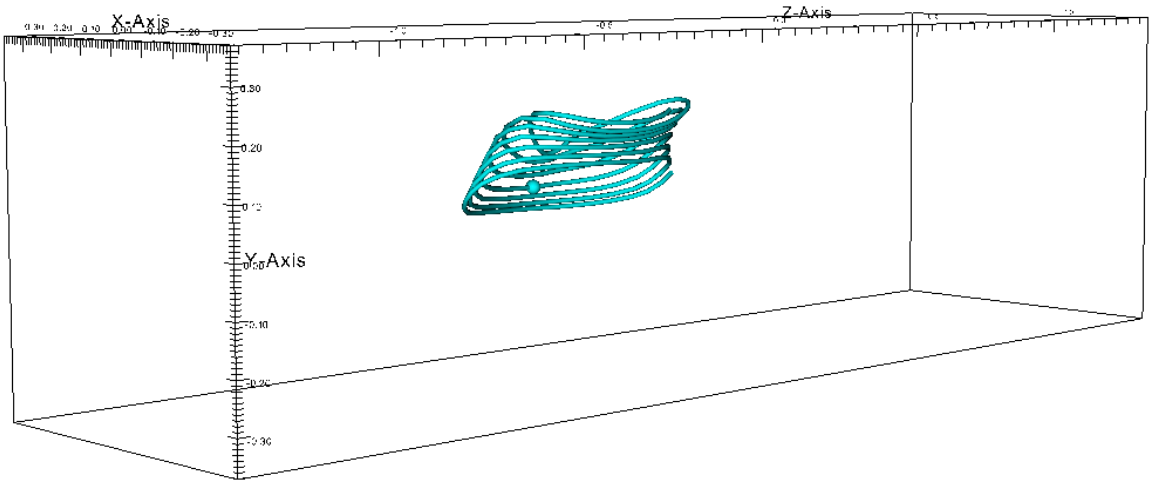

Figure 6.27: Odd-parity magnetic field streamline launched from (0.34,0,0)

If we look at 10 streamlines launched from r = 0.2 m z = 0.3 m, shown in *figure 6.28*, we do not see the typical s-shaped transit seen in the even-parity driven FRC but see the structure of an FRC.

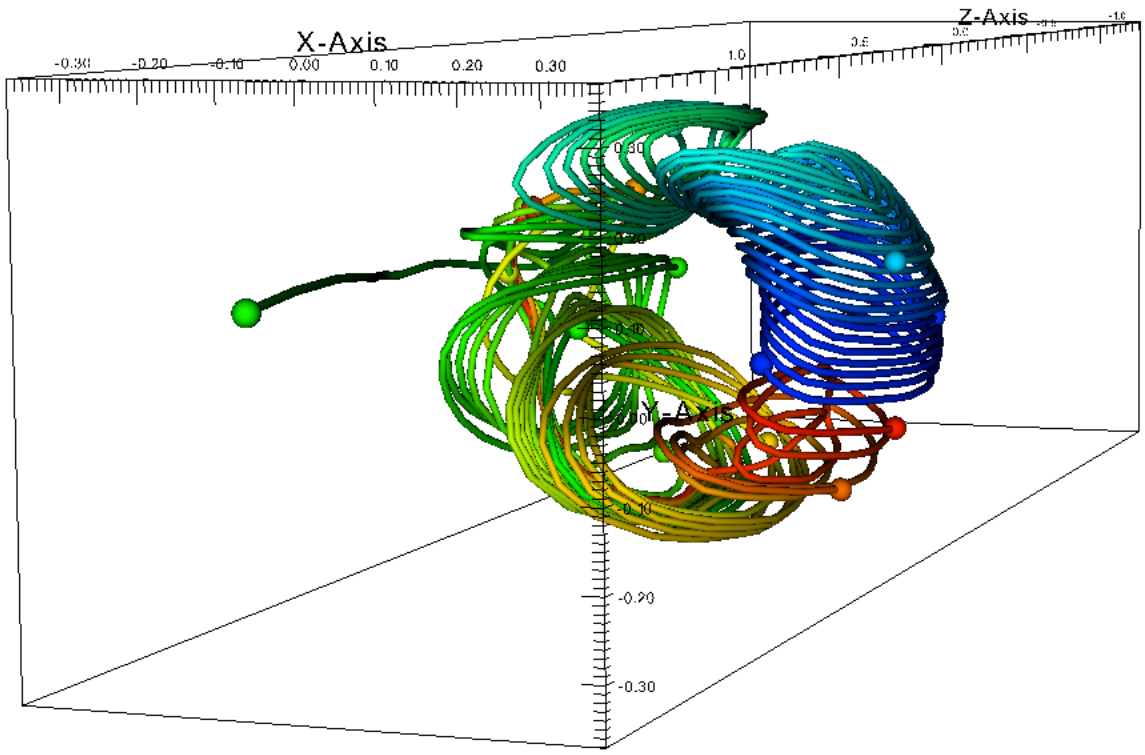

Figure 6.28: Ten odd-parity driven FRC streamlines launched from r = 0.2, z = 0.3 showing multiple transits of the FRC

The odd-parity driven FRC allows for multiple field line transits. *Figure 6.29* shows field lines launched from various radii at the midplane. The length of the lines that execute multiple transits is truncated to limit errors but many still intersect the radial boundary. It is possible that some of the field lines would eventually exit the FRC and intersect the ends of the domain like in the NIMROD simulation results. Regardless, the overall behavior of the experimental data is in agreement with the simulation, shown in *figure 6.30*.

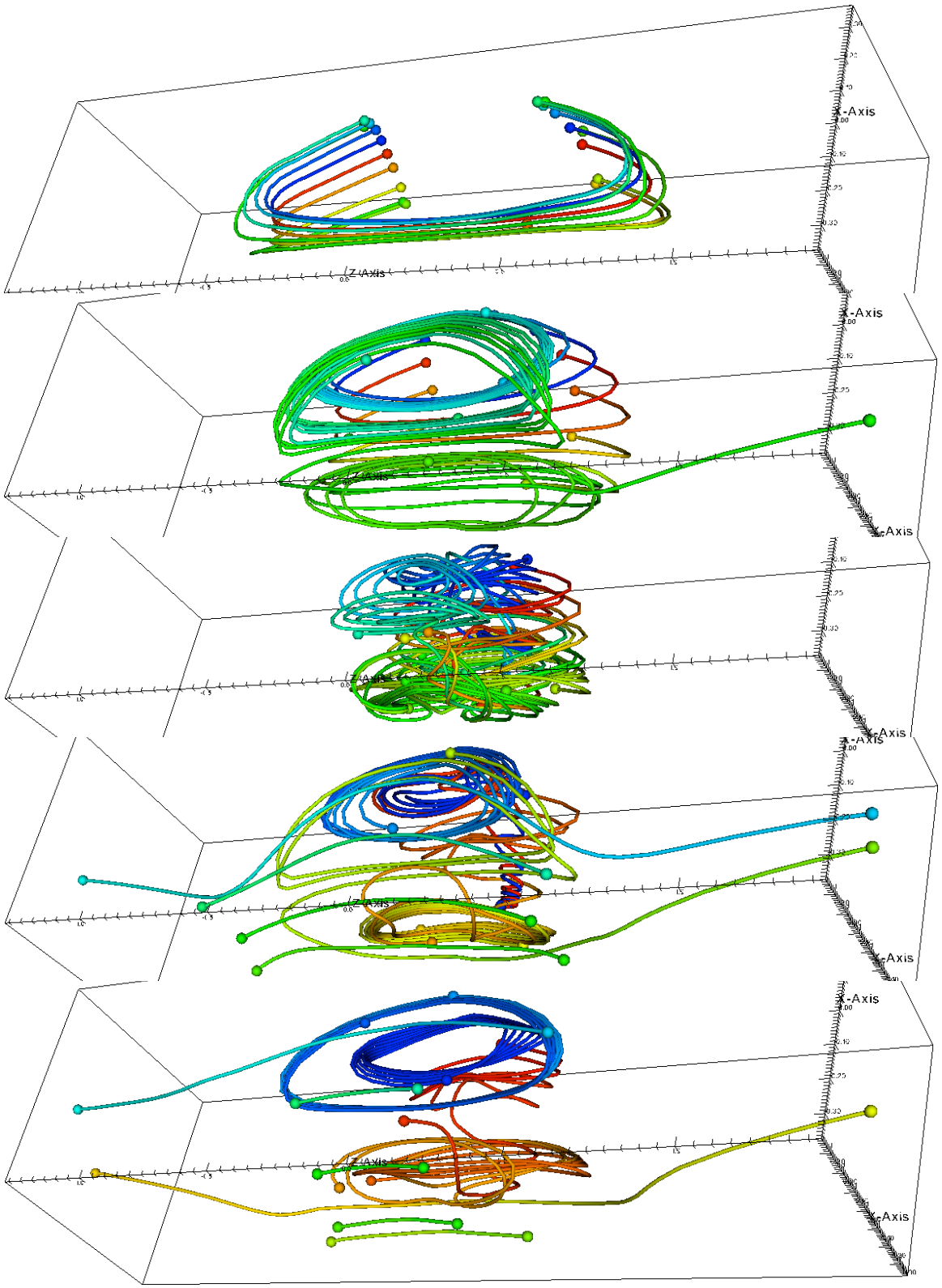

Figure 6.29: Experimental magnetic field lines from even-parity RMF driven FRC. In each plot, 10 field lines are launched from a circle of radius 0.03, 0.10, 0.20, 0.30, and 0.35 m (top to bottom)

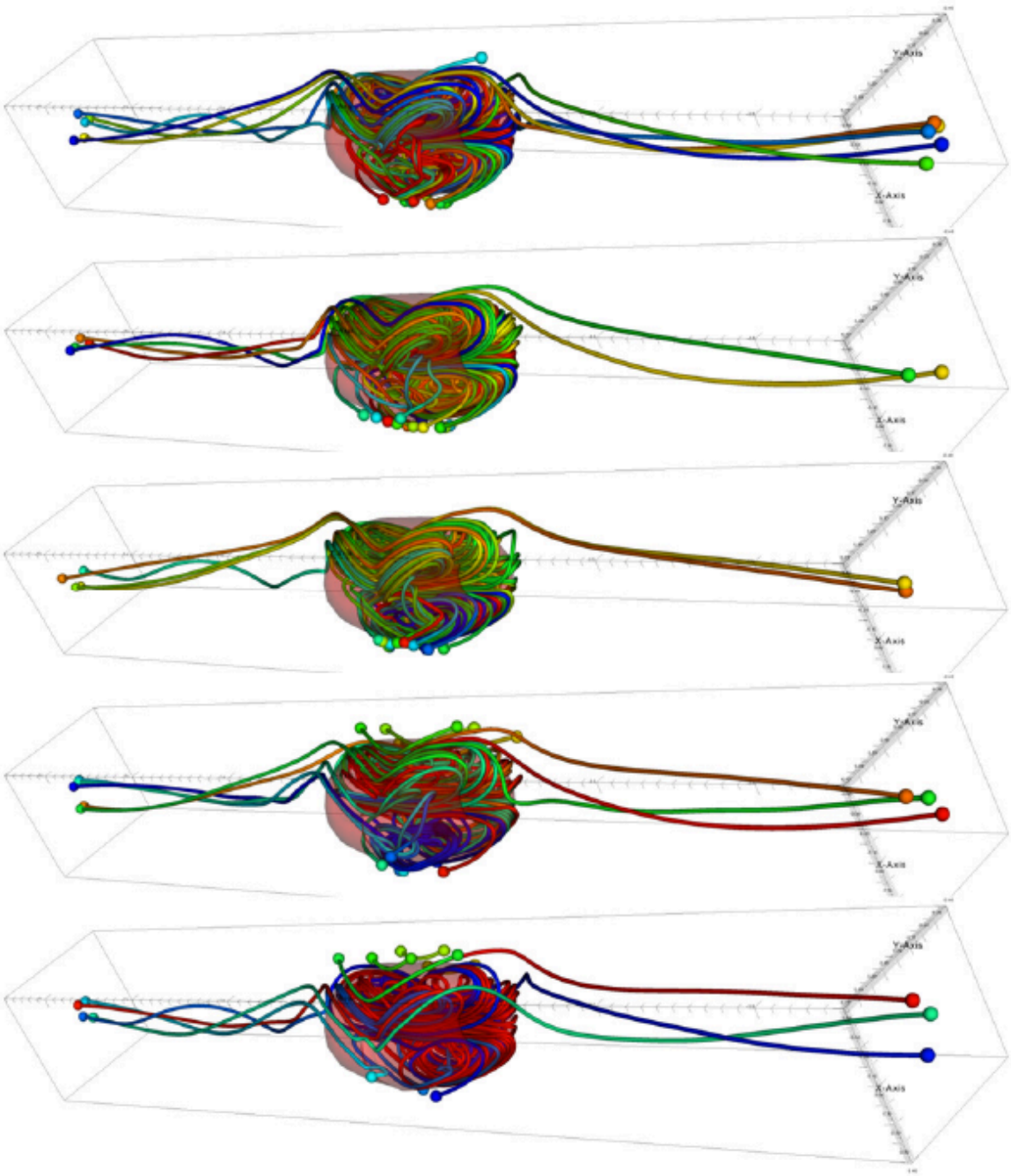

Figure 6.30: Three-dimensional images of magnetic field lines and a partially transparent pressure contour for an odd-parity NIMROD calculation. In each plot, 10 field lines are launched from a circle of radius 0.03, 0.10, 0.20, 0.30, and 0.35 m (top to bottom) [20]

There are field lines that enter and exit under the RMF antenna at the same azimuthal location. *Figure 6.*31 shows the outline of the FRC, drawn using the mean-field data with six field lines drawn at r = 0.34, z = -0.2 m. Some of these field lines exhibit a U-shaped path instead of the S-shaped path seen in even-parity. These field lines can be shallow, penetrating just past the separatrix (green), or penetrate deep into the FRC (blue and red). The yellow and light blue field lines intersect with the axial boundary and twist around the boundary of the FRC These field lines appear to be convected with the electrons as they rotate.

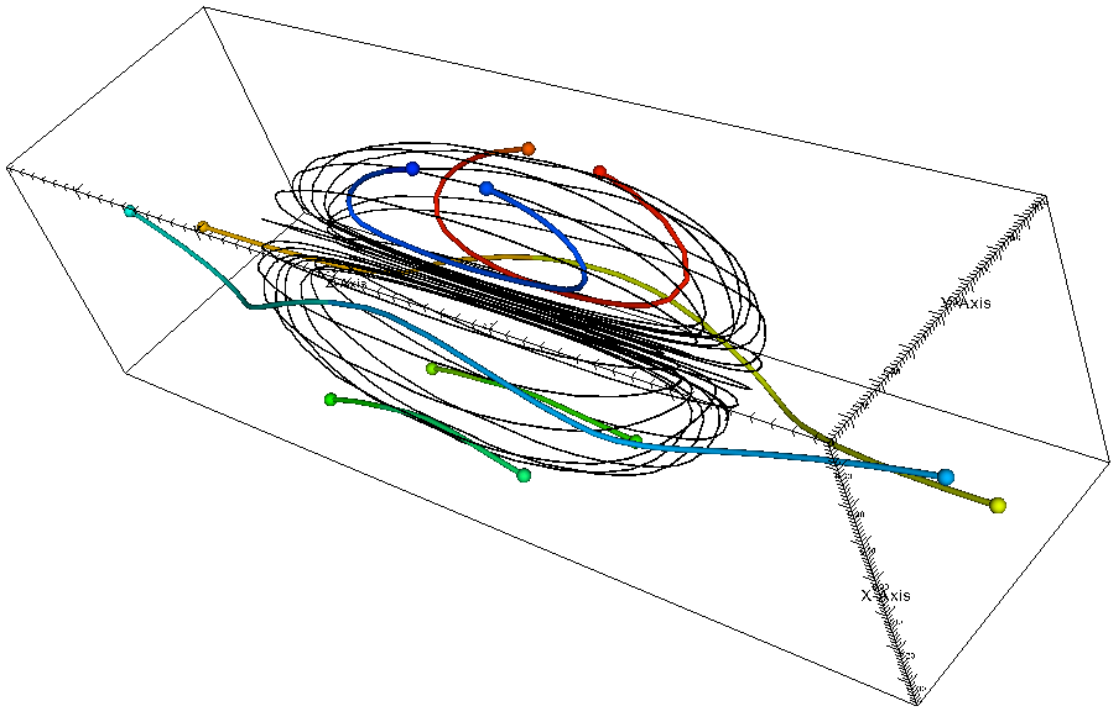

Figure 6.31: Odd-parity mean-field streamline (black) with RMF+ steady magnetic field lines (color)

As predicted, odd-parity RMF drive is better at maintaining the FRC structure. *Figure 6.32* shows multiple field lines launched from each end of the probe range. As in even-parity drive, the field lines launched at the ends, near the machine axis, intersect the radial boundary in the quartz region under the RMF antennas.

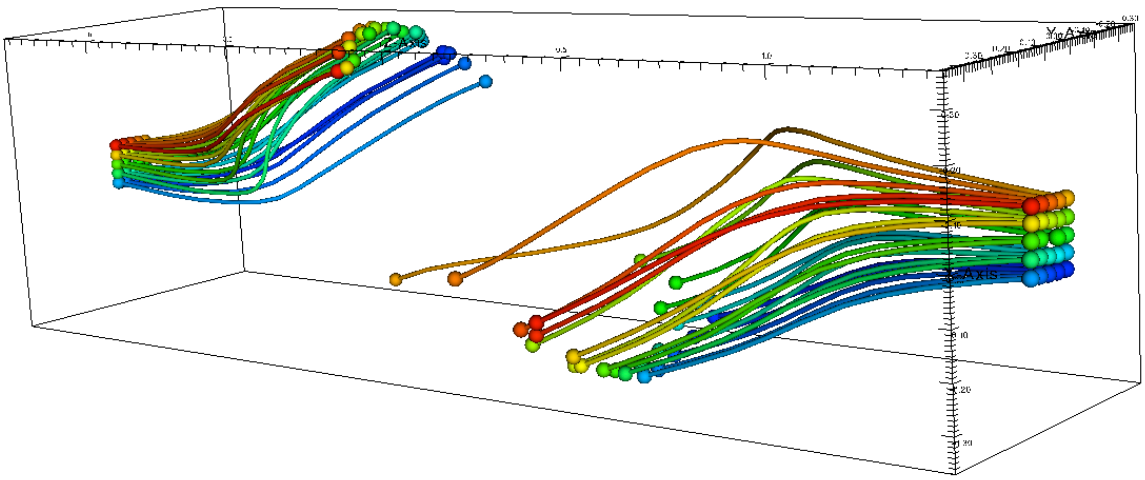

Figure 6.32: Odd-parity magnetic field lines launched from the ends of the experimental domain pass through the quartz wall of the formation chamber

The translatable three-axis probe has allowed us to visualize the full FRC and open field line region using the average and RMF components of the magnetic field. As discussed in *section 6.3,* we did not include the slowly rotating inner structure in the full 3D visualization because the structure varies in phase and frequency both in time during the FRC lifetime and between machine pulses. As theorized, the odd-parity RMF drive allows for multiple field line transits of the FRC and has a more twisted and complicated structure than does the even-parity RMF driven FRC.

Chapter 7: **LOW FREQUENCY INTERNAL STRUCTURE**

In *chapter 6*, we approximated the total magnetic field in three dimensions using the two strongest magnetic field frequency components: the average field from applying a 10 kHz low-pass filter and the RMF component from applying a 20 kHz wide band-pass filter at the RMF frequency (122 kHz for even-parity and 107 kHz for odd-parity). However, there was another peak in the frequency spectrum that could not be included in the 3D representation but which can be analyzed by looking at the data in the x – y plane as a function of axial location. The approximately 37 kHz peak in the even-parity case and 28 kHz peak in the odd-parity case are related to a phenomenon previously seen in the TCS machine called edge-drive mode[**25**]; the ~30 kHz signal corresponds to an inner structure rotating at that frequency. The edge-drive mode was described in two-dimensions using a midplane probe and a 2D r-θ MHD simulation. Using the three-axis probe on TCSU we see a fully three-dimensional mechanism with a complicated structure within the FRC that interacts with the RMF at both the outer edge and central axis of the machine. However, the similarities between edge-drive and the behavior seen in TCSU lead us to believe that we are observing the same mechanism but are able to provide a more complete description of how the RMF drives current on the inner field lines.

Section 7.1: Edge-drive mode

In previous work on the TCS machine, edge-drive mode was seen in high RMF frequency cases where the RMF did not penetrate to the magnetic field null. Only the electrons at the outer edge of the FRC are co-rotating with the RMF, resulting in a low $\zeta = 0.13$. *Figure 7.1* shows the typical radial profile measured by a two-axis midplane probe for an edge-driven FRC in TCS; the solid line is the average B_z field and the dotted line is the envelope of the 236 kHz RMF B_θ. The RMF field peaks outside of the separatrix, which is at r = 0.35 cm.

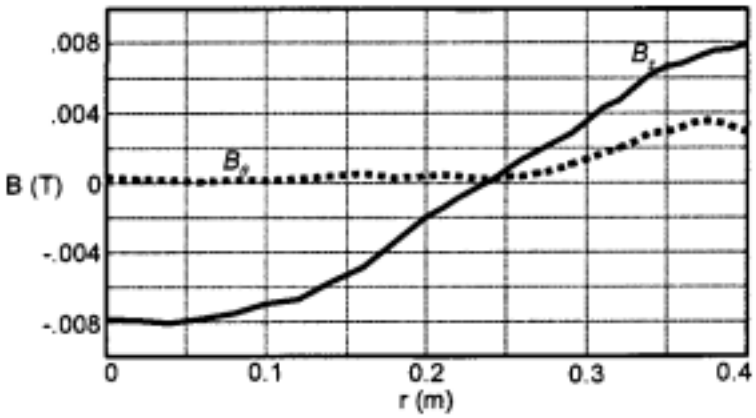

Figure 7.1: TCS experimentally measured magnetic profiles where the RMF, at the applied frequency, did not penetrate to the magnetic field null. From ref [25]

Typical magnetic field profiles from TCSU for the 122 kHz even-parity RMF are shown in *figure 7.2*; the red curve is the envelope of the 122 kHz RMF B_θ and the B_z curve is the average field from applying a 10 kHz low-pass filter. The separatrix is at r = 0.35 cm but the RMF peaks just inside the separatrix and measures 1.5 mT at the field null. The RMF is measured on the inner field lines near r = 0 indicating that some electrons near the axis are rotating at the RMF frequency. In TCSU, the typical ζ parameter is around 0.5.

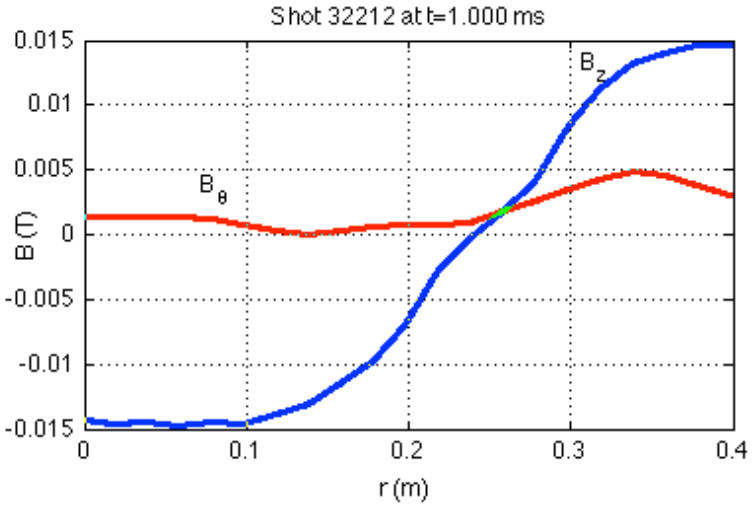

Figure 7.2: TCSU measured magnetic profiles with a small RMF magnitude at the magnetic null

The frequency spectrum of the TCS data, shown in *figure 7.3*, exhibits the same behavior seen in TCSU, shown in *figure 7.4*. The dominant features are at the RMF frequency and below 10kHz. A third frequency peak in the TCS data at 28 kHz (labeled f_{struct}) is analogous to the 37 kHz signal seen in the TCSU data. A smaller signal from the B_z probes is seen at 208 kHz (236 – 28 kHz) in *figure 7.3* or at 85 kHz (122 – 37 kHz) in *figure 7.4* . However, the small peak at $f_{RMF} + f_{struc}$ in *figure 7.4* is not apparent in the plot from TCS. The TCS internal probe shows a large signal on $B_z$ext at the RMF frequency, which is due to noise pickup.

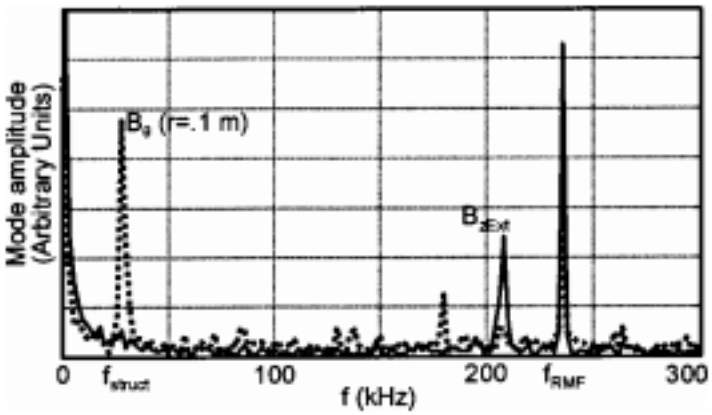

Figure 7.3: Spectral amplitude of the measured external $B_z$ext (solid line) and internal B_θ (dotted line) during the time window of 0.8 – 1.3 ms. From ref [25]

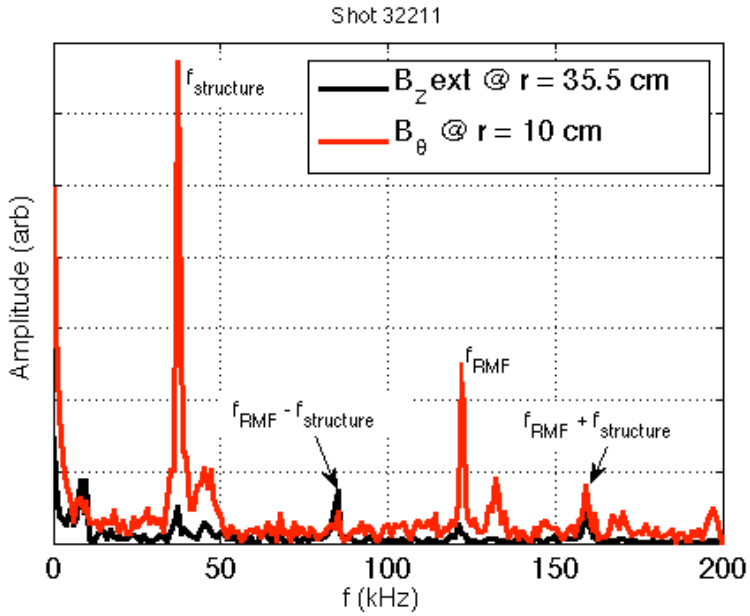

Figure 7.4: Frequency spectrum from TCSU of $B_z$ext (black) and internal B_θ (red) during the time window 1.0 – 2.0 ms

The B_θ contour maps shown in *figure 7.5* and *7.6* display the full bandwidth as a function of radius and time at the midplane for TCSU and TCS, respectively. In each figure, the oscillating bands at the outer radii are at the RMF frequency. The TCSU data in *figure 7.5*, has wide bands clearly visible around $0.8 < r < 0.18$ m, which oscillate at 37 kHz. This indicates a region where the electrons are rotating primarily at 37 kHz. The RMF frequency is again visible near $r = 0$ because the magnetic field lines that transit an s-shaped path through the FRC rotate at the RMF frequency. On either side of the 37 kHz band there is a region a few centimeters wide where the two frequencies mix.

In the TCS data presented in *figure 7.6*, the low frequency oscillation is less distinct but still visible inside $r = 0.3$ m. The 236 kHz RMF signature is present throughout and any frequency mixing is unclear.

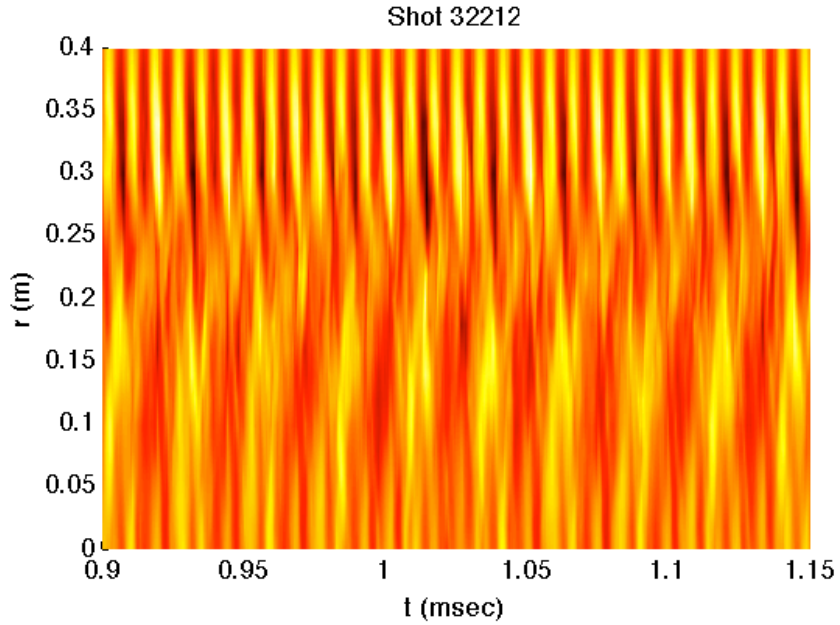

Figure 7.5: B_θ contours as a function of radius and time for 122 kHz RMF TCSU measurements taken at the midplane.

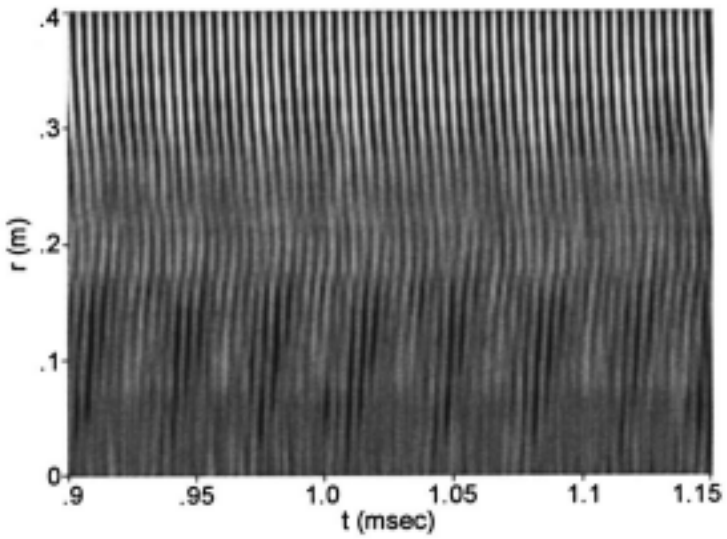

Figure 7.6: B_θ contour map as a function of radius and time as measured by the internal probe in TCS. From ref [25]

Section 7.2: Field line approximation of inner structure

The analysis of the edge-drive mode in TCS included RMF field line plots generated using the midplane probe data. The RMF frequency was isolated from the B_θ component using a 20 kHz wide band-pass filter and extrapolated in θ assuming a simple sin(θ) spatial variation. Assuming an infinitely long cylinder, the magnetic field is given in terms of the vector potential as $B_\theta = -\frac{\partial A_z}{\partial r}$ and $B_r = \frac{1}{r}\frac{\partial A_z}{\partial \theta}$, therefore,

$$A_z(r) = \int_0^r -B_\theta dr. \qquad (7.1)$$

The RMF magnetic field lines are approximated by plotting contours of A_z calculated using *equation 7.1*. Lines of constant A_z are in the direction of the magnetic field because the gradient of A_z is perpendicular to the magnetic field.

The RMF field lines shown in *figure 7.7* were calculated from the TCS midplane probe data as part of the edge-drive analysis. The RMF is excluded by the FRC and concentrated near the wall; the magnitude of the magnetic field is larger where the lines

are closer together. However, the 28 kHz inner structure is not visible because the field lines were generated using only the data at the 236 kHz RMF frequency.

Figure 7.7: RMF field lines inferred from TCS experimental data.
From ref [25]

This field line representation does not account for the large axial component of the total magnetic field. The 2D picture of the RMF field lines is a projection of the RMF field onto the r–θ plane. However, this flattened picture still illustrates how the field lines bend and twist in response to differential electron rotation.

There is not experimental data from TCS that displays the field lines with the 28 kHz structure included. However, numerical simulations were made using a two-dimensional (r – θ) MHD code tailored to the TCS experiment[**27**]. The simulation captured a separate slowly rotating internal structure that corresponds to the 28 kHz experimental data. *Figure 7.8* shows the magnetic field line plots from the simulation as the RMF makes a full rotation with respect to the inner structure. The figure is plotted in the RMF reference frame such that the RMF is vertical and the inner structure appears to rotate clockwise. As the RMF rotates, the field lines tear and reconnect, facilitating torque transfer from the edge toward the center. The simulation results do not show the RMF frequency near r = 0, which we see in the TCSU experimental data.

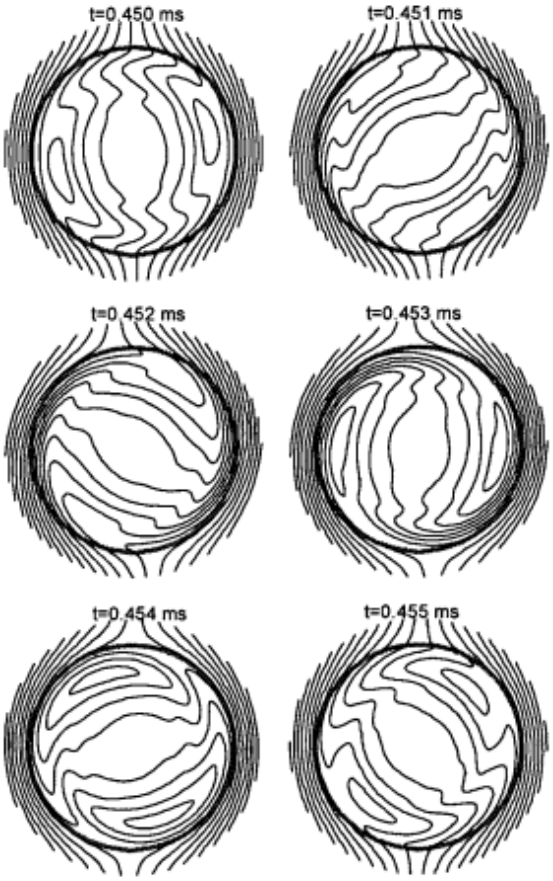

Figure 7.8: Time sequence of the calculated RMF field lines as the primary RMF makes a full rotation relative to the inner structure. The circle indicates the position of the vacuum-plasma boundary. From ref [25]

Section 7.3: Even-parity RMF with a 37 kHz structure

We can use the simplified field line representation described above to analyze the 37 kHz signal measured by the three-axis probe in TCSU. Plotting r-θ cross-sections at various axial locations sheds light on how the 37 kHz signal affects the magnetic structure. The 37 kHz signal persists during the quiescent period of the FRC from approximately 0.6 – 1.6 ms. *Figure 7.9* shows the time evolution of the frequency spectrum of the B_x probe at the midplane at r = 16 cm where the 37 kHz signal is strongest and shows the onset of the structure at 0.6 ms.

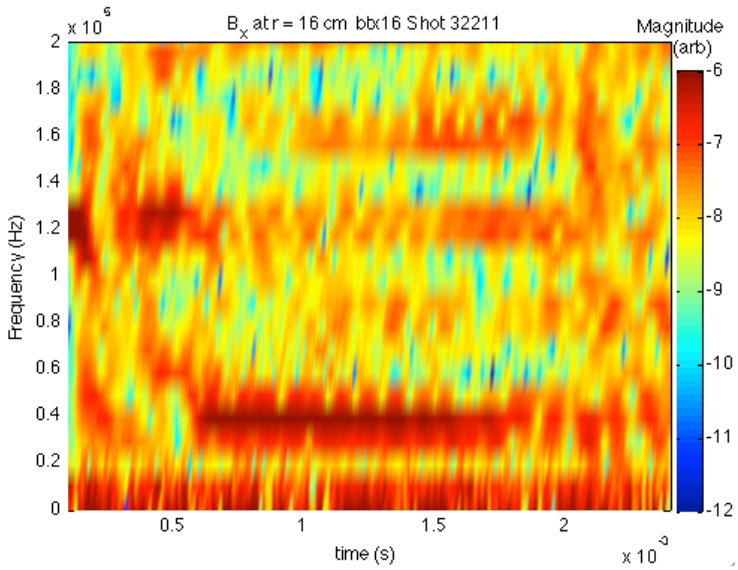

Figure 7.9: Time evolution of the frequency spectrum of B_x at r = 16 cm

Using the same method described in *chapter 6* to extrapolate the probe measurements in theta, we calculate A_z using *equation 7.1* and approximate magnetic field lines as described in *section 7.2*. The even-parity RMF field lines are drawn in *figure 7.10* for one full rotation. The color indicates the value of A_z and is added for clarity. As expected, the field lines are concentrated in the edge region where the RMF peaks. The field lines go through r = 0 indicating the presence of the RMF on axis, which was not seen in the previous work on edge-drive mode in TCS.

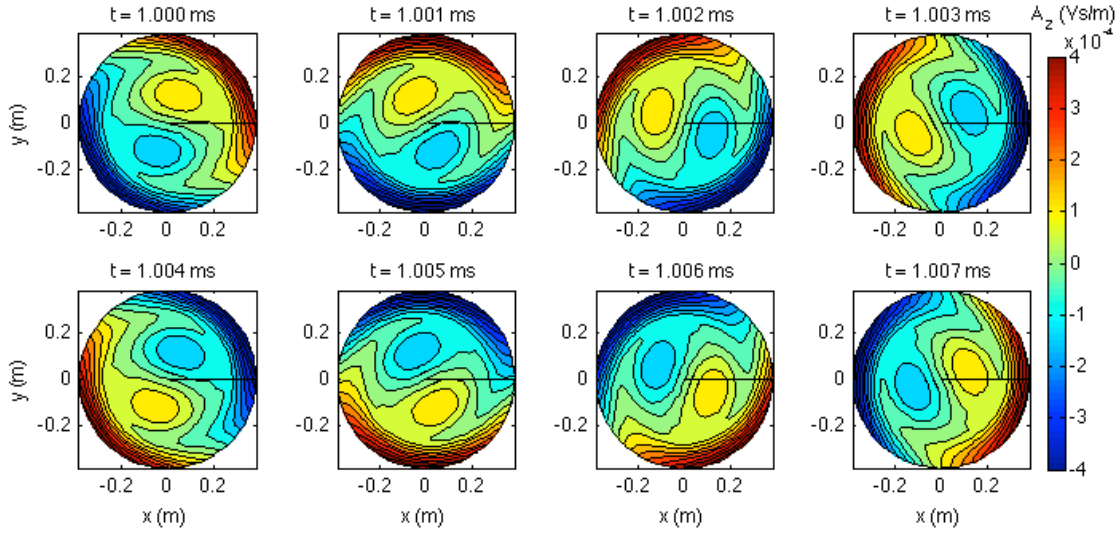

Figure 7.10: Time sequence of 122 kHZ RMF field lines for one full rotation for shot 32211.

It was shown in *section 6.3* that the 37 kHz data has a sin(θ) azimuthal dependence. We can visualize the 37 kHz signal by isolating the data using a band-pass filter centered at 37 kHz, extrapolating the data in θ and plotting contours of A_z calculated using *equation 7.1*. The field lines calculated using the data at 37 kHz are shown in *figure 7.11* for approximately half of one rotation. There is a concentration of field lines in a ring at r ≈ 0.15 corresponding to the band of data seen in *figure 7.5*.

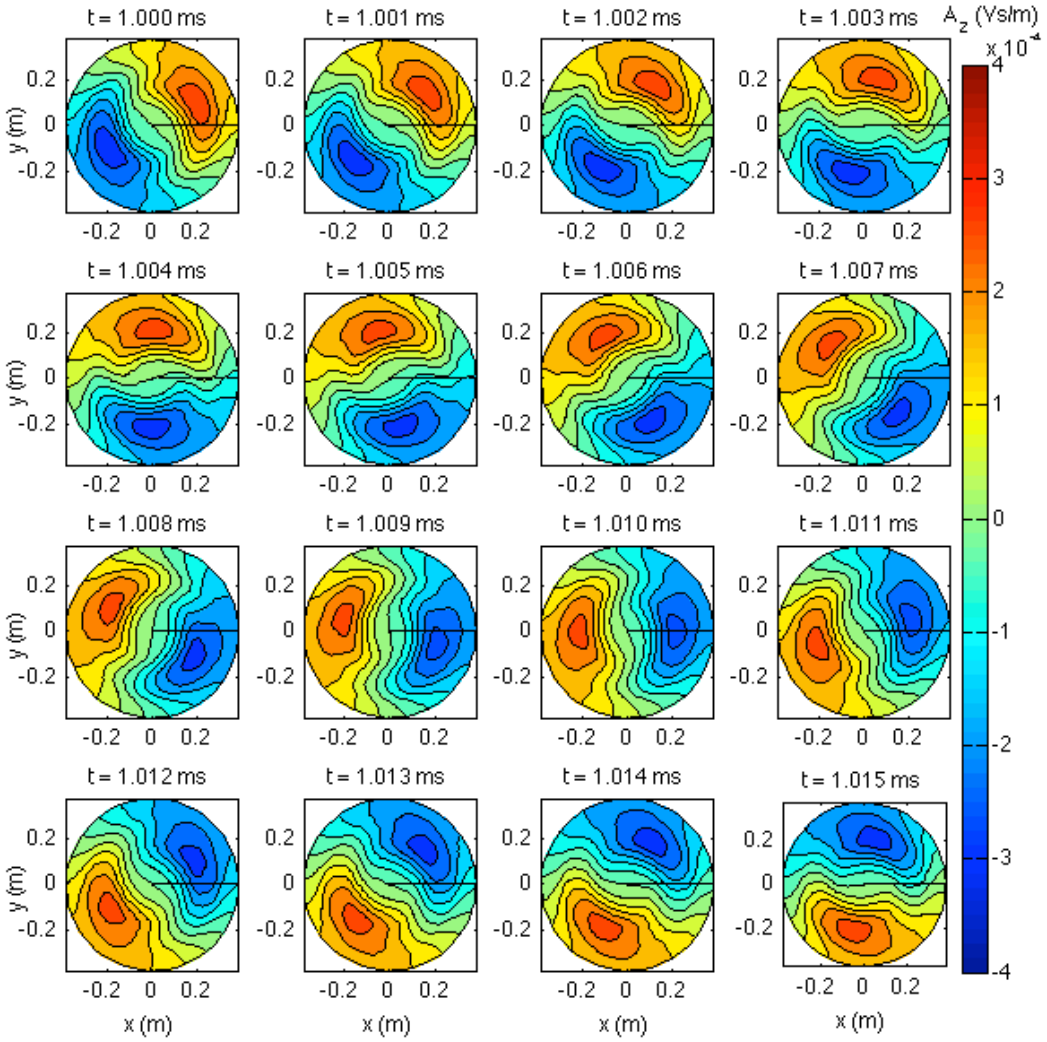

Figure 7.11: Time sequence of 37 kHz field lines for shot 32211. 13.5 μsec is approximately half of one rotation.

The 122 kHz and 37 kHz data each form field lines with a consistent structure that rotates counterclockwise. However, when the data is combined, the overall field line structure becomes complicated. *Figure 7.12* shows field lines plotted using the

combination of the 37 kHz and 122 kHz data. At 1.000 ms, the direction of A_z for 37 and 122 kHz aligns and the two structures combine constructively. After 1.000 ms, the lines begin to stretch and twist; at 1.005 there is reconnection. As the field lines bend and reconnect, the torque is transferred from the edge to the inner regions.

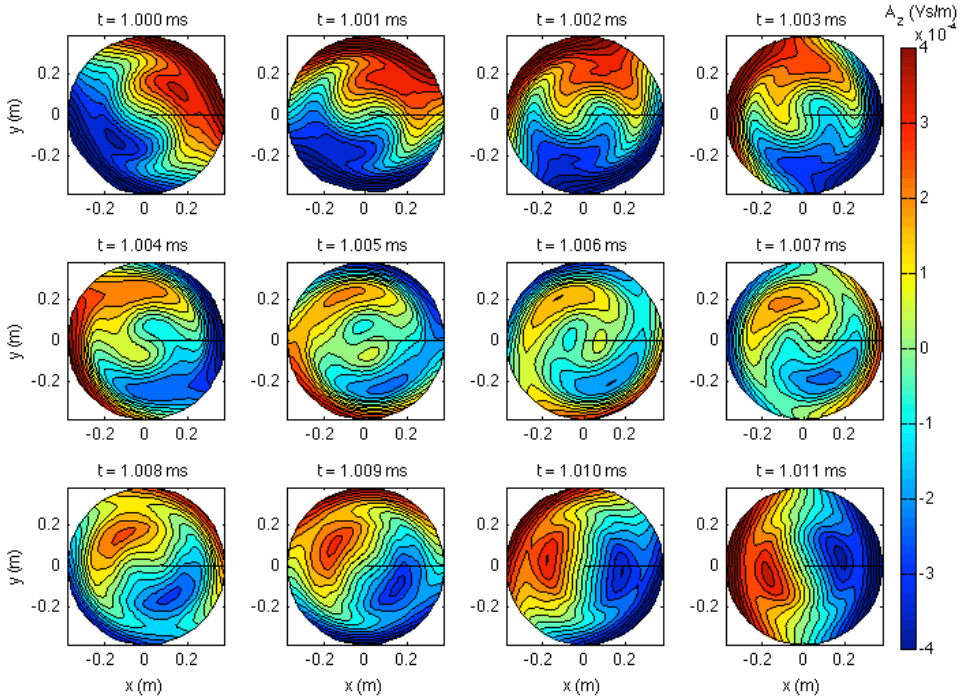

Figure 7.12: Time sequence of 37 kHz + 122 kHz rotation at the midplane starting at t = 1.000 ms

We can also look at the B_θ data directly. *Figure 7.13* shows the RMF field, the 37 kHz structure, and the two components combined at 1.005 ms, when the field lines are twisted. Again, we see the RMF concentrated at the edge with a smaller magnitude near $r = 0$. The 37 kHz signal is strongest in a ring at $r \approx 0.15$ but also has a small contribution near the field null. The combined picture shows how the central region of 37 kHz data interacts with the outer band of RMF.

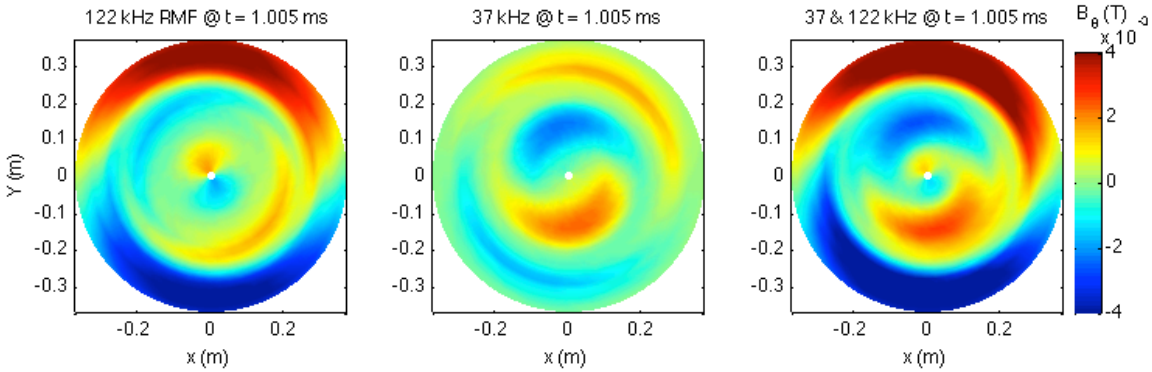

Figure 7.13: B_θ at the midplane at 1.005 ms for the RMF, 37 kHz, and combined signal.

The data presented so far has been from the midplane, z = 0, only. However, as we saw in *chapter 6*, the magnetic field structure is fully 3D. The r – z cross-section of the envelope of the 37 kHz signal shown in *figure 7.14* emphasizes the 3D nature. The white and red lines are the flux contours calculated using the average magnetic field from applying at 10 kHz low-pass filter to show the general shape of the FRC. The 37 kHz signal is concentrated around the midplane in the B_θ component but there is a comparable signal in the B_z on either side of the midplane. The 37 kHz signal does not extend farther than 0.6 m from the midplane, which is where the RMF antennas end.

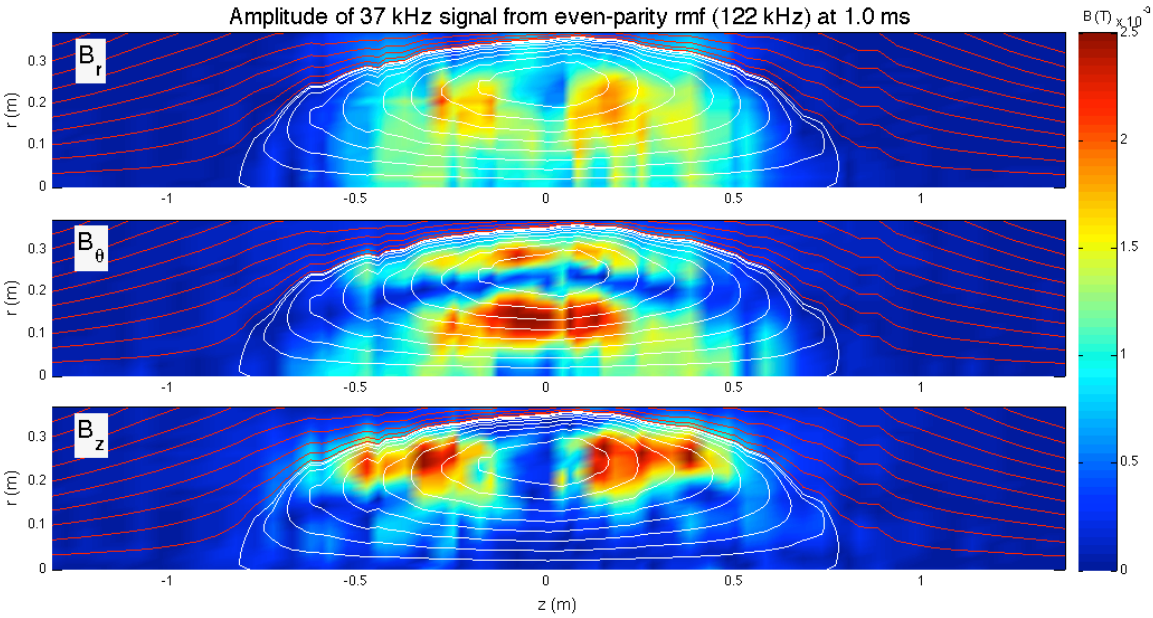

Figure 7.14: Amplitude of 37 kHz component of B_r, B_θ , and B_z at 1 ms shown in an r–z cross-section

We see in *figure 7.14* that the B_θ component of the 37 kHz structure is concentrated around the midplane but even a small 37 kHz signal deforms the RMF field line structure. *Figures 7.15* and *7.16* show the same time series of the RMF + 37 kHz component at z = -0.1 m and 0.3 m, respectively. At z = -0.1, there is still a strong 37 kHz B_θ signal and the field line structure is similar to what we see at the midplane.

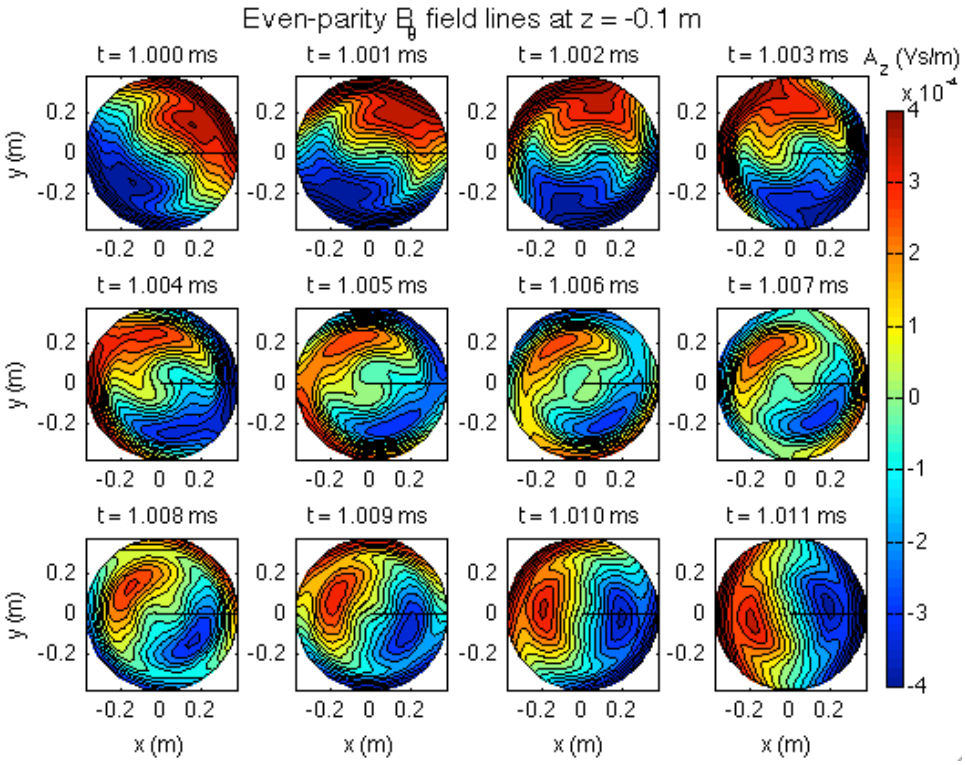

Figure 7.15: Time sequence of the RMF + 37 kHz B_θ field lines at z = -0.1 m

The strength of the 37 kHz signal is small at z = 0.3 m but still has a small effect on the field line structure. For example, at t = 1.006 ms it appears that the RMF field is fully penetrated, however, this is due to the constructive interference of the two rotating structures. At 1.001 ms, the two structures combine destructively and the magnetic field is near zero in r < 0.1 m

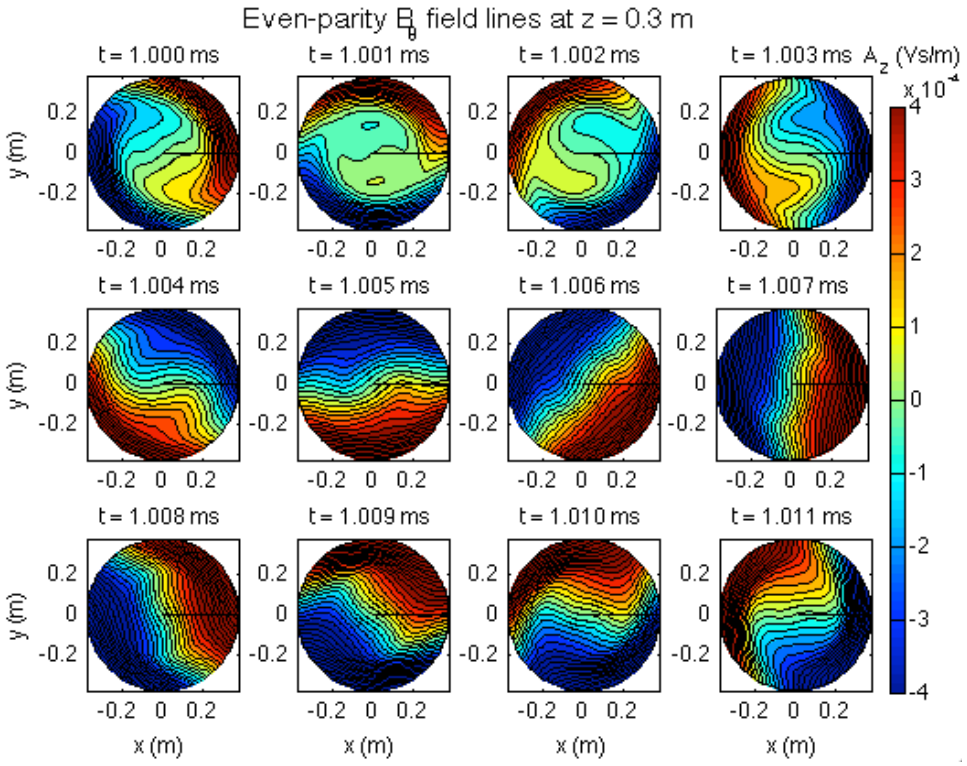

Figure 7.14: Time sequence of the field line structure formed by the RMF and 37 kHz components of B_θ.

Section 7.4: Odd-parity RMF with a 28 kHz structure

The slowly rotating structure is also seen in odd-parity RMF drive but near 28 kHz. The time evolution of the frequency spectrum at r = 10 cm, near the peak of the 28 kHz signal is seen in *figure 7.17*. The data is taken at z = -28 cm, under the center of one half of the odd-parity RMF antenna.

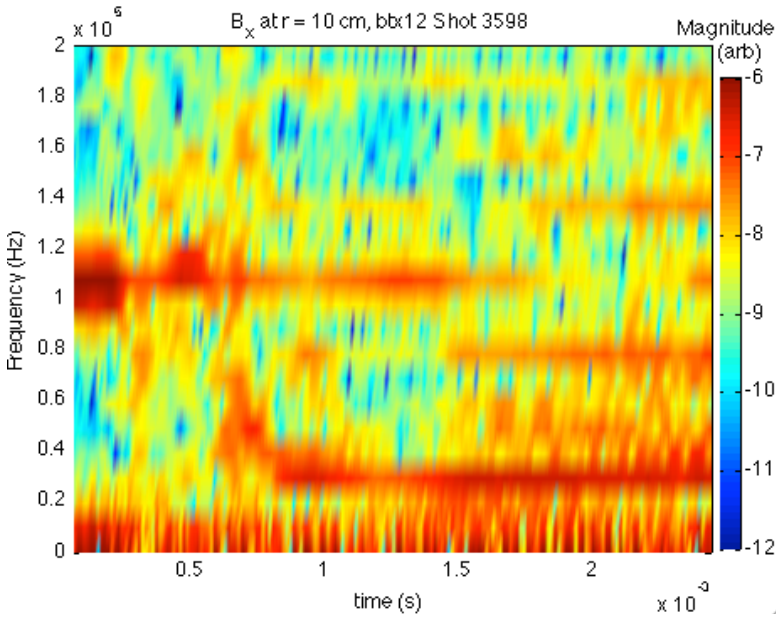

Figure 7.15: Time evolution of the odd-parity frequency spectrum at r = 10 cm

The frequency spectrum as a function of radius, averaged over the quiescent period of the FRC is shown in *figure 7.18*. The 28 kHz peak is dominant around 10 cm while the signal around 20 – 30 cm is dwarfed by the RMF signal.

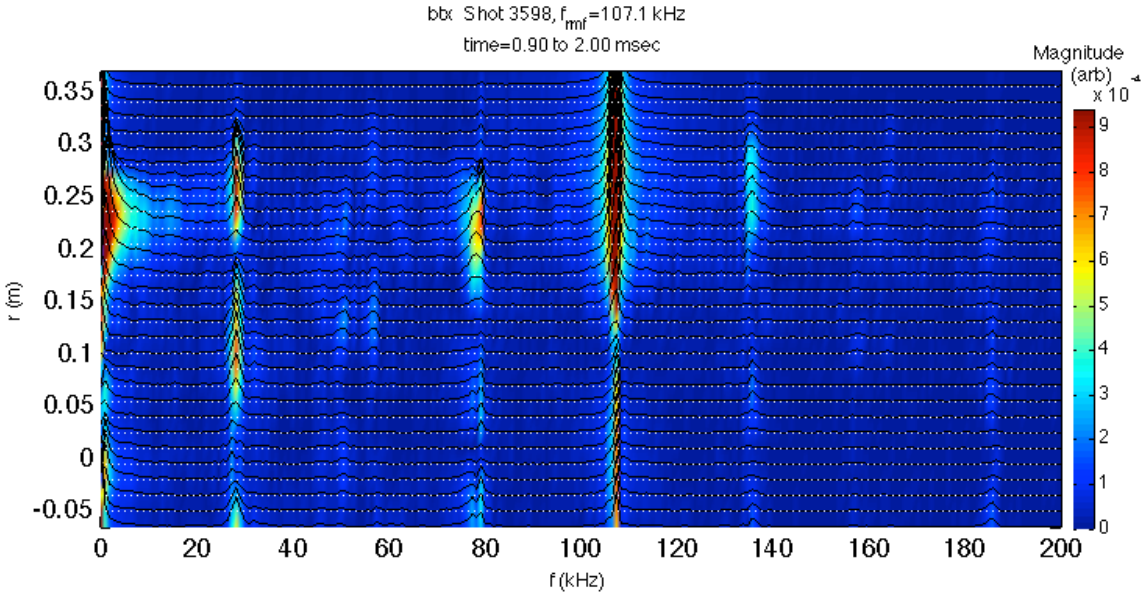

Figure 7.16: Frequency spectrum of odd-parity B_θ at z = - 28 cm during the period 0.9 – 2.0 ms.

The amplitude of the 28 kHz signal for each magnetic field component is shown in *figure 7.19*. The slowly rotating structure is concentrated in B_θ around the midplane. Unlike in the even-parity driven FRC, there is little activity in the B_z component. The magnitude of the 28 kHz signal peaks at 1.5 mT whereas the 107 kHz RMF is approximately 4 mT.

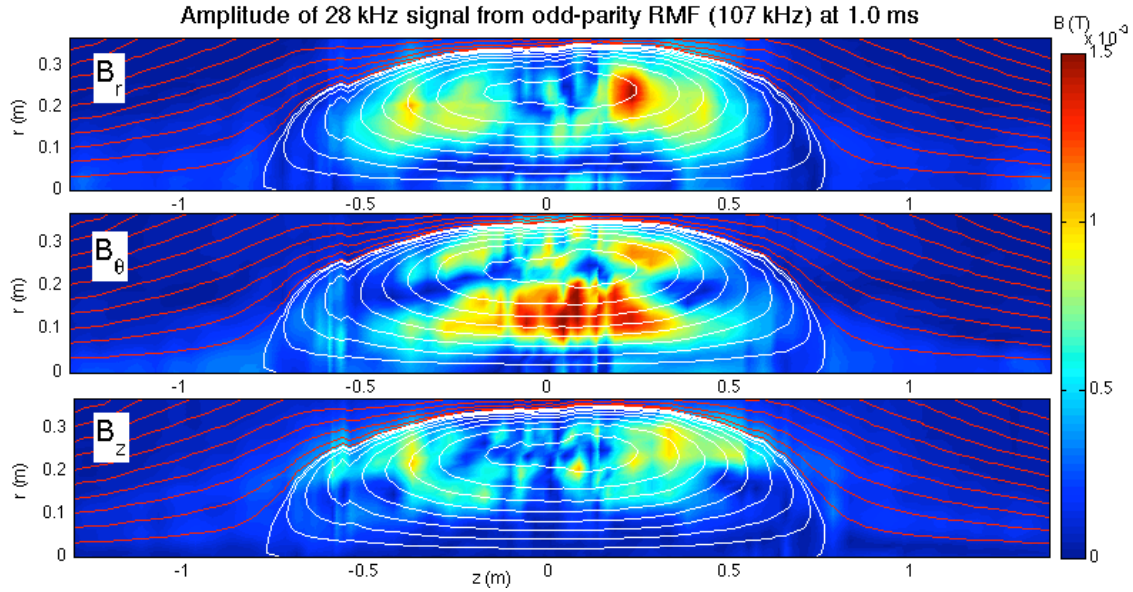

Figure 7.19: Amplitude of 28 kHz signal from odd-parity RMF driven FRC

In odd-parity, the RMF B_θ is strongest around +/- 0.3 m. The RMF lines are plotted at z = 0.28 m in *figure 7.20*, starting at 1.000 ms for one complete rotation. We see a similar RMF field line structure as for even-parity at the midplane. The 28 kHz rotating structure at z = 0.28 m is shown in *figure 7.21* for approximately half of one rotation. As in even-parity, the structure of the field lines generated using each frequency component is consistent in time.

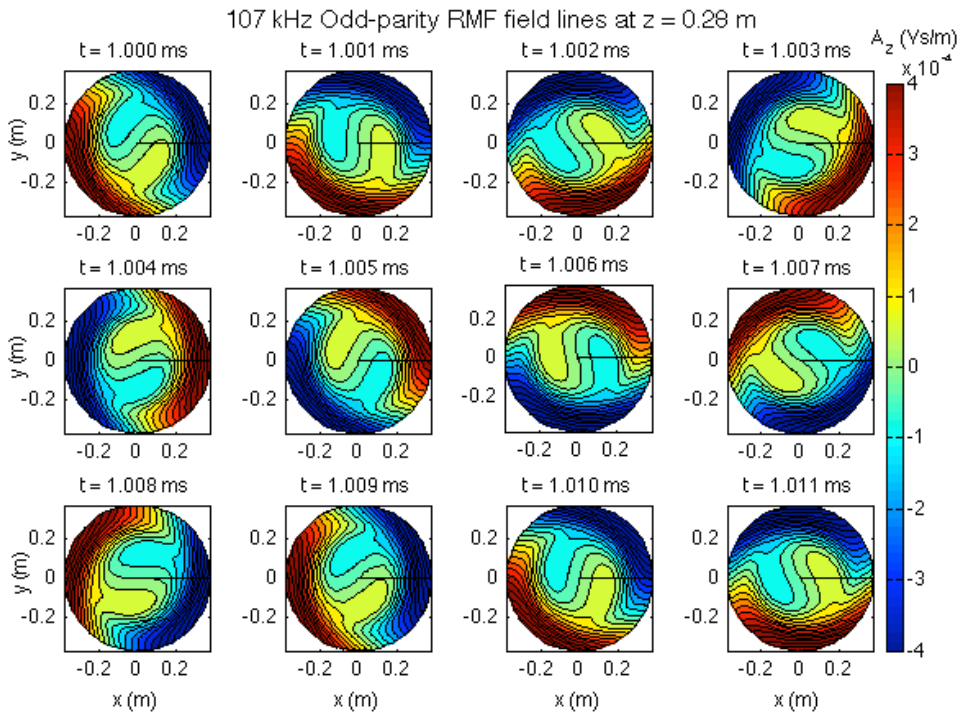

Figure 7.20: Odd-parity RMF field lines at z = 0.28 m

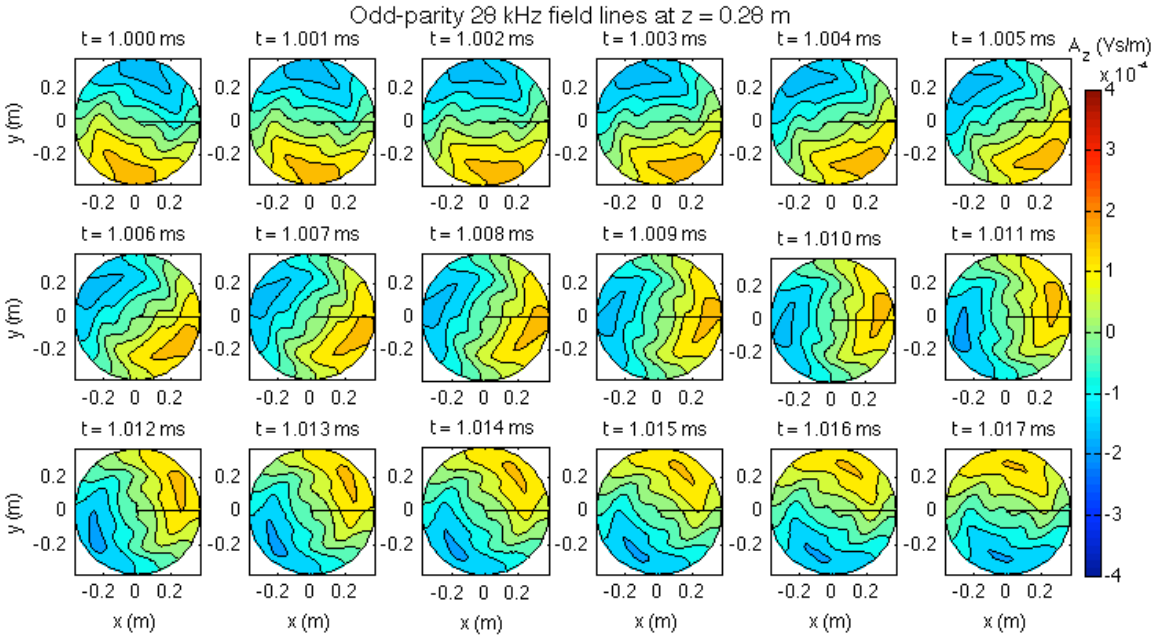

Figure 7.21: Odd-parity 28 kHz rotating structure at z = 0.28 m

The combined field structure shown in *figure 7.22* is dominated by the RMF but the field lines are twisted as the two different rotating field structures combine.

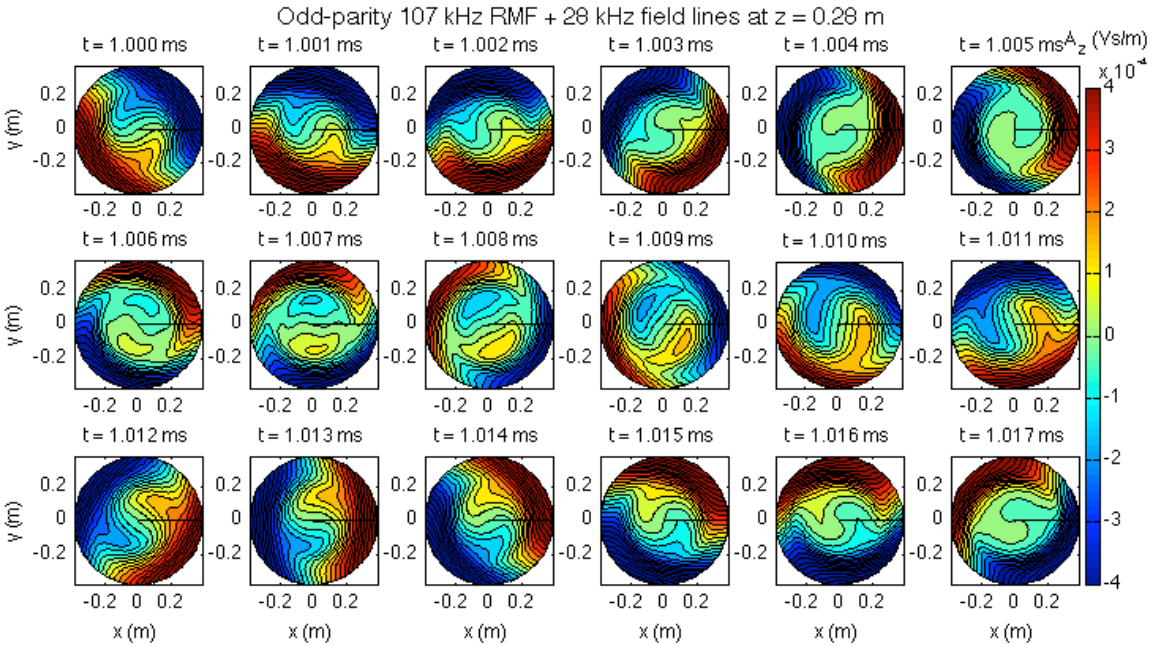

Figure 7.22: Time series of 107 kHz + 28 kHz rotating structures at z = 0.28 m.

Near z = +0.08 m, the 107 kHz and 28 kHz signals have a similar magnitude but the combined field lines shown in *figure 7.23* exhibit a similar overall structure as at 28 cm.

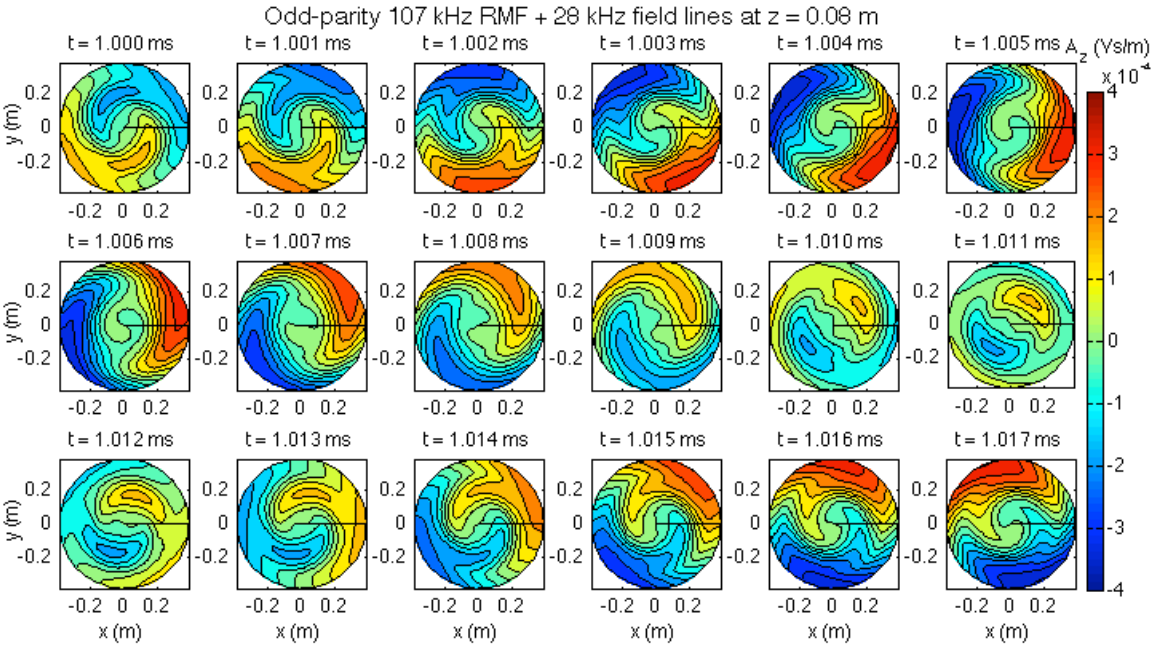

Figure 7.17: Time series of 107 kHz + 28 kHz rotating structures at z = 0.08 m.

The theory developed to describe edge-drive mode was two-dimensional but using the three-axis probe we see that the previously described effect is, in fact, fully three-dimensional. There is a region within the radius of the magnetic field null where the electrons are primarily rotating around 30 kHz. On either side of this region the electrons are primarily rotating at the RMF frequency. The magnetic field lines convect with the electrons in each region. The differential electron rotation causes the field lines to bend and stretch, facilitating current drive on the inner field lines. The complicated magnetic field line structure within the FRC could help transfer the torque applied by RMF to the inner field lines of the FRC.

Chapter 8: **MAGNETIC TORQUE MEASUREMENTS**

Using the internal magnetic probe to measure B_x, B_y, and B_z throughout the confinement region of TCSU has allowed us to develop a detailed torque model of RMF current drive. Measurements of the magnetic field are used to calculate a torque balance based on torque about the axis of the machine (torques in the θ direction) applied to the FRC volume. As before, we focus our analysis on the mean-field and RMF frequency components of the magnetic field. We calculate the torque due to the average field data by applying a 10 kHz low pass filter and the torque associated with the RMF using data at 122 kHz for even-parity or 107 kHz for odd-parity.

The majority of the RMF torque is deposited in the FRC outside of the field null. A portion of the RMF torque is transferred to a mean-field torque inside the field null, which drives current on the inner field lines. In addition to the torque transmitted radially inward there is a torque transmitted axially. Just outside the x-point there is a torque from the steady state magnetic field in the opposite direction to the RMF torque called the shorting torque that reduces the RMF drive. Inside the FRC, there is a small torque flowing axially toward the midplane, which also contributes to current drive on the inner field lines.

Section 8.1: Torque equations

The RMF exerts a torque on the electrons. The torque is transferred to the ions through resistive drag. Ion-neutral interactions limit the ion spin-up to approximately 10 kHz [**28**]. As outlined in *chapter 2,* a model was developed to describe RMF current drive is terms of the RMF torque on the FRC. The poloidal flux changes according to the balance of RMF torque and resistive torque given as:

$$\frac{d\varphi_p}{dt} = \frac{2}{n_e e r_s^2}\left(T_{RMF} - T_\eta\right), \tag{8.1}$$

where φ_p is the poloidal flux, n_e is the electron density, e is the electron charge, r_s is the separatrix radius, T_{RMF} is the RMF torque, and T_η is the resistive torque.

In the analytic torque model the RMF and resistive torques are equal to:

$$T_{RMF} = \frac{2\pi r_s^2 B_\omega^2}{\mu_o} l_a f(\xi) \tag{8.2}$$

$$T_\eta = 1.16\pi r_s^2 e n_m l_s \left(\frac{B_e}{\mu_o}\right)\langle \eta_\perp \rangle, \tag{8.3}$$

where B_ω is the RMF calculated from the current in the antenna, l_a is the antenna length, $f(\xi)$ is a factor based on ξ but computed to be approximately 0.1, n_m is the maximum density, l_s is the separatrix length, B_e is the external B_z, and $\langle \eta_\perp \rangle$ is the average perpendicular resistivity.

In steady state, the applied torque is balanced by the resistive torque. The analytical model assumes the torque is axially uniform and does not take in account the end effects from the RMF antenna. A portion of the RMF torque is applied to the open field lines that twist up to an equilibrium value, creating a toroidal field in the jet. To include these end effects we use a torque analysis based on the Maxwell stress tensor to describe the forces on the FRC.

The total electromagnetic force on the FRC volume is given by

$$\vec{F} = \iiint \left(\rho\vec{E} + \vec{j} \times \vec{B}\right) d\tau. \tag{8.4}$$

Applying Maxwell's equations ($\nabla \cdot \vec{E} = \frac{1}{\varepsilon_o}\rho$ and $\nabla \times \vec{B} = \mu_o \vec{j} + \mu_o \varepsilon_o \frac{\partial \vec{E}}{\partial t}$) and the Maxwell stress tensor (Π) yields

$$\vec{F} = \iiint \left(\nabla \cdot \vec{\vec{\Pi}}\right) d\tau - \mu_o \varepsilon_o \frac{d}{dt} \iiint \vec{S} d\tau \tag{8.5}$$

However, only the magnetic force contributes so we get,

$$\vec{F} = \iiint \left(\nabla \cdot \vec{\vec{\Pi}}_M\right) d\tau, \tag{8.6}$$

where the Maxwell stress tensor is:

$$\vec{\vec{\Pi}}_M = \frac{\vec{B}\vec{B}}{\mu_o} - \frac{B^2}{2\mu_o}\vec{\vec{I}} \tag{8.7}$$

Applying the divergence theorem gives

$$\vec{F} = \oiint \vec{\vec{\Pi}}_M \cdot \hat{n} dS \tag{8.8}$$

We are concerned with the torque about the z-axis, which is given by

$$T = \oiint r\hat{\theta} \cdot \ddot{\Pi}_M \cdot \hat{n} dS \tag{8.9}$$

This represents the total torque deposited inside the volume; it is the torque transferred through the surface and is analogous to a momentum flow through the surface. Consider a control volume around the FRC with surfaces in the radial and z directions, shown in *figure 8.1*.

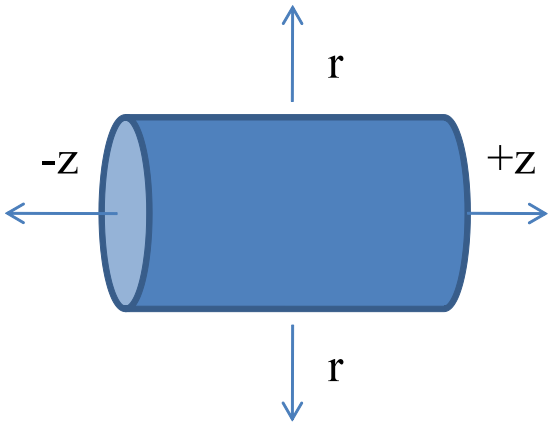

Figure 8.1: Control volume used to represent the FRC

The total torque applied to the FRC has a contribution from each surface. The torque transferred through radial wall of the cylinder is primarily due to the RMF field, i.e. T_{RMF}. Some of the RMF torque is converted to a mean-field torque that is transferred out of the control volume through the end caps. The RMF twists the open field lines that terminate on a conducting boundary creating an axisymmetric, steady state B_θ. The resultant mean-field torque is called the shorting torque, $T_{shorting}$.

The torque transfer through the radial wall is calculated from an integration over the radial surface of the control volume and is given by *equation 8.9* as,

$$\mathrm{T[r]} = \frac{r^2}{\mu_o} \iint B_r B_\theta d\theta dz \tag{8.10}$$

The shorting torque passing through each end cap is,

$$\mathrm{T[-z]} = \iint -\frac{B_\theta B_z}{\mu_o} r^2 d\theta dr \text{ and } \mathrm{T[+z]} = \iint \frac{B_\theta B_z}{\mu_o} r^2 d\theta dr \tag{8.11}$$

The RMF torque is calculated using B_r and B_θ filtered with a 20 kHz wide band-pass filter at the RMF frequency to isolate contribution from the RMF.

The expression for the RMF torque can be represented in terms of the amplitude and phase of the RMF component of the magnetic field,

$$T_{RMF} = \frac{r^2}{\mu_o}\int_{z1}^{z2}\int_{0}^{2\pi}\tilde{B}_r\cos\left(\vartheta-\phi_r\right)\tilde{B}_\theta\cos\left(\vartheta-\phi_\theta\right)d\vartheta dz \tag{8.12}$$

where $\tilde{B}$ is the amplitude of the RMF component, ϕ is the phase with respect to the peak of the signal, ϑ is the azimuthal location, and (z1, z2) is the axial extent of the control volume. *Equation 8.12* can be rewritten as

$$T_{RMF} = \frac{r^2}{2\mu_o}\int_{z1}^{z2}\int_{0}^{2\pi}\tilde{B}_r\tilde{B}_\theta\left(\cos\left(\phi_\theta-\phi_r\right)+\cos\left(2\vartheta+\phi_\theta+\phi_r\right)\right)d\vartheta dz. \tag{8.13}$$

The integral over theta is simply $2\pi\cos(\phi_\theta-\phi_r)$ and the expression for the RMF torque becomes

$$T_{RMF} = \frac{\pi r^2}{\mu_o}\int_{z1}^{z2}\tilde{B}_r\tilde{B}_\theta\cos\left(\phi_\theta-\phi_r\right)dz \tag{8.14}$$

similarly, the RMF torque transmitted axially is

$$T_Z^{RMF} = \frac{\pi}{\mu_o}\int_{0}^{r}r^2\tilde{B}_z\tilde{B}_\theta\cos\left(\phi_\theta-\phi_z\right)dr \tag{8.15}$$

Section 8.2: RMF torque

As in *chapter 6*, the amplitude and phase are calculated using the Hilbert transform[**26**]. The torque transmitted by the RMF across the radial boundary is calculated using B_r and B_θ at r = 35.5, the first probe windings outside of the 34 – 35 cm separatrix radius. This analysis focuses on the quiescent period of the FRC, from approximately 0.7 – 2.0 ms.

The even-parity RMF amplitude at the radial boundary, calculated using the Hilbert transform, is shown in *figure 8.2* as a function of axial position for t = 1.0 ms.

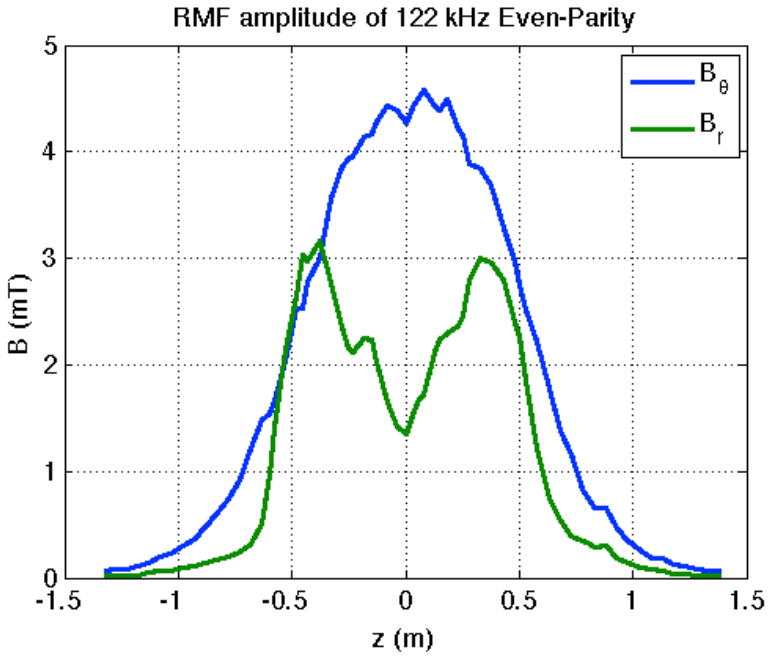

Figure 8.2: Amplitude of the even-parity RMF component of B_θ and B_r at 1.0 ms

The RMF amplitude for odd-parity, shown in *figure 8.3*, peaks at a similar magnitude but drops to zero at the midplane. This is because the antennas are split at the midplane and the RMF is in the z-direction where the antenna straps wrap around the machine azimuthally.

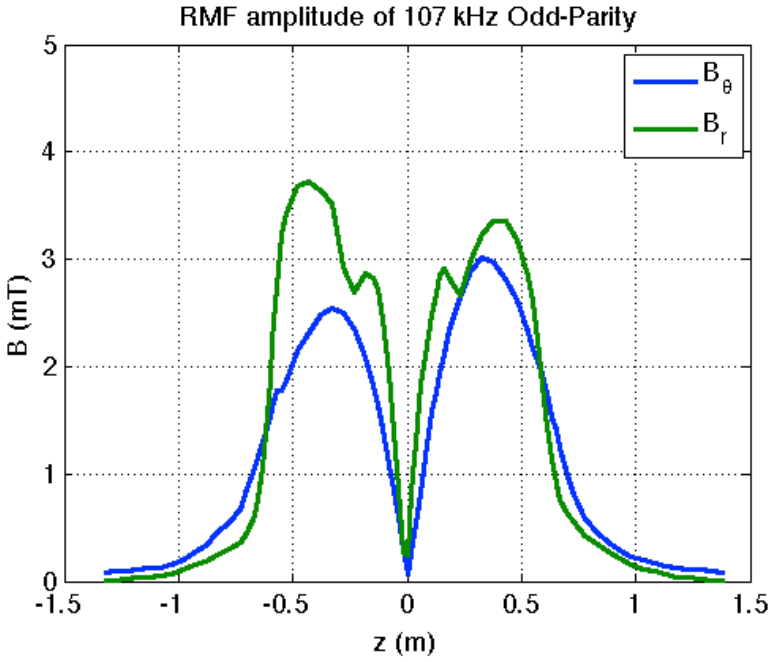

Figure 8.3: Amplitude of the odd-parity RMF components of B_θ and B_r at 1.0 ms

There is a small RMF component present past the ends of the antennas. The axial integration for the torque is done for the extent of the measured RMF signal. Shown in *figure 8.4* is RMF torque density transmitted across r = 35.5 cm for 122 kHz long mirror even-parity and 107 kHz long mirror odd-parity at 1 ms during the quiescent period of the FRC. The RMF torque is not constant along the length of the RMF antennas, which is an assumption made in the analytical model.

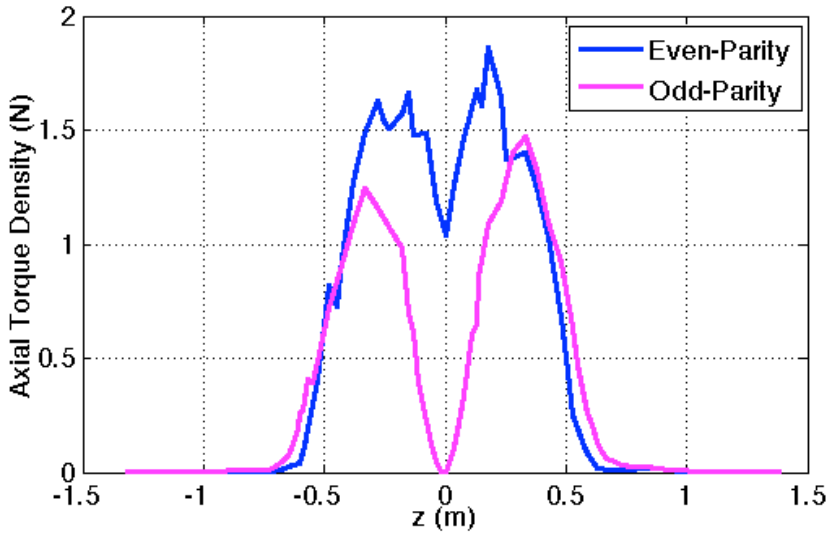

Figure 8.4: Axial dependence of RMF torque transmitted across the radial boundary at r = 35.5 cm for the even-parity and odd-parity RMF configurations

The total RMF torque shown as a function of time in *figure 8.5* is the result of the axial integration of the torque density. In steady state, RMF torque for the 122 kHz even-parity and 107 kHz odd-parity formed FRC is approximately 1.3 N-m and 0.9 N-m, respectively

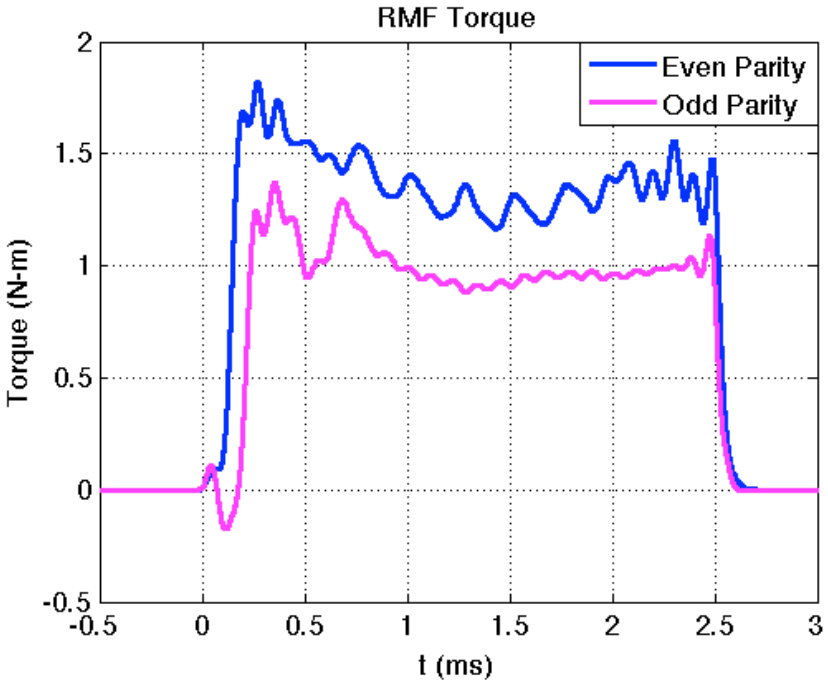

Figure 5: Total RMF torque transmitted across r = 35.5 cm for even and odd-parity

Section 8.3 Shorting torque

The open field lines terminate on a conducting boundary. Under the quartz wall in the confinement chamber, the field lines rotate with the RMF, which causes the open field lines to twist, creating an azimuthally symmetric B_θ. A portion of the RMF momentum flowing across the radial boundary does not act on the FRC but is lost out the axial ends of the control volume. In this picture, the shorting torque is the portion of the RMF torque that is converted to a mean-field torque transmitted axially away from the midplane. Again, the shorting torque is calculated at a specific axial location using,

$$T_{shorting} = \int_0^r \int_0^{2\pi} \frac{B_\theta B_z}{\mu_o} r^2 d\theta dr . \qquad (8.16)$$

The shorting torque transmitted axially near the ends of the FRC is calculated from probe measurements taken just outside the x-point. The average field component of the data is obtained by applying a 10 kHz low-pass filter. The shorting torque calculation is done for the quiescent time period when the FRC is in steady state and the length is constant.

The shorting torque is in the opposite direction of the RMF torque, reducing the total torque applied to the FRC. Shown in *figure 8.6* is the magnitude of the shorting torque from the north (+z) and south (-z) ends of the FRC for the 122 kHz even-parity RMF. Theoretically, the shorting torque should be equal on each end of the FRC but there are measured differences in each end due to asymmetries in the FRC and TCSU. Notice that the measurements used for the shorting torque are taken from slightly different locations on either side of the FRC. This is due to slight asymmetry in the FRC as well as differences in the measurement locations; there was no measurement made at z = -80 cm for 122 kHz even-parity.

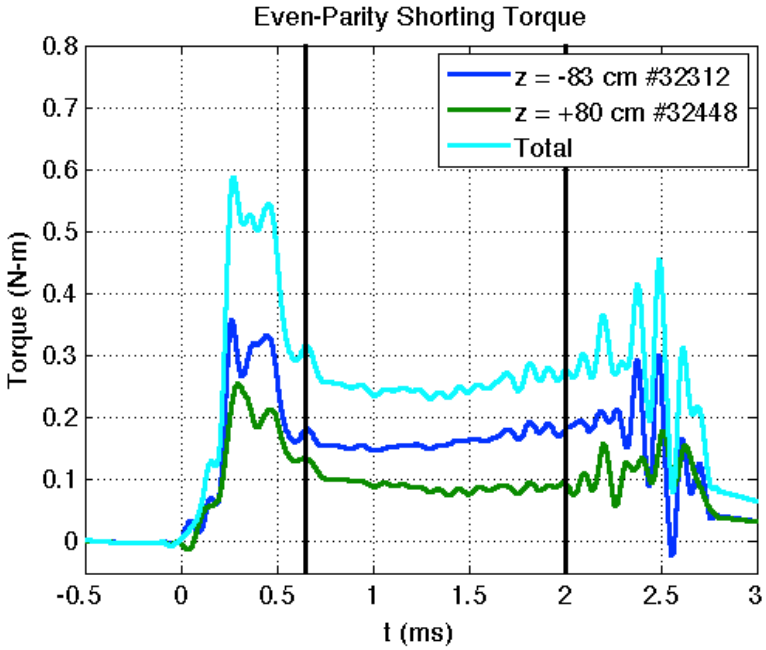

Figure 8.6: Even-parity shorting torque. The black lines indicate the boundary of the quiescent period

The black bars mark the boundary of the quiescent period of the FRC. This is defined as the time period where the length of the FRC is constant. For even-parity this starts as approximately t = 0.7 ms and ends at 2.0 ms. An n = 2 rotational instability would often develop after 2 ms.

The measurement for RMF torque is taken just outside the separatrix at r = 35.5 cm so the shorting torque is integrated out to the same radius. The shorting

torque from each end of the FRC is the torque transferred though the +z and –z surfaces of the control volume and will be used to calculate the total torque on the FRC.

The shorting torque in the odd-parity FRC is shown in *figure 8.7* and is slightly larger than in the even-parity case. The formation phase of the odd-parity RMF FRC is longer than in even-parity but the n = 2 instability would not develop; the quiescent period is approximately 0.8 – 2.2 ms.

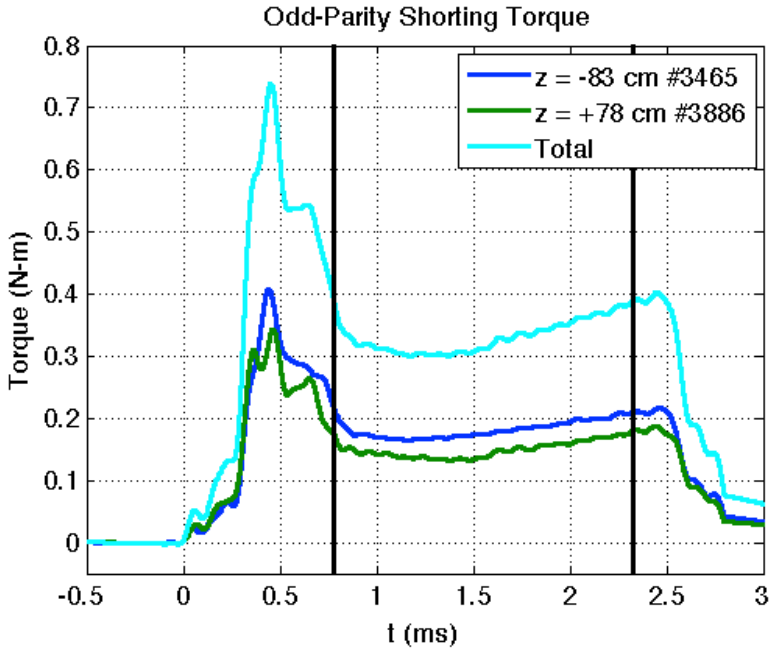

Figure 8.7: Odd-parity shorting torque

Section 8.4: Total applied torque

The total torque applied to the FRC is the RMF torque reduced by the shorting torque. Rather, the total torque deposited inside the control volume is the momentum flowing inward across the radial boundary minus the momentum flowing out across the axial boundaries of the control volume. The results from the even-parity torque calculation are shown in *figure 8.8*; the boundaries of the quiescent period are marked in black. The total torque applied by the even-parity RMF is approximately 1 N-m. The torque calculated using the analytical approximation given by *equation 8.2* is also shown

in *figure 8.8*. The estimate agrees well with the calculation using probe data of the total torque but underestimates the value of the RMF torque.

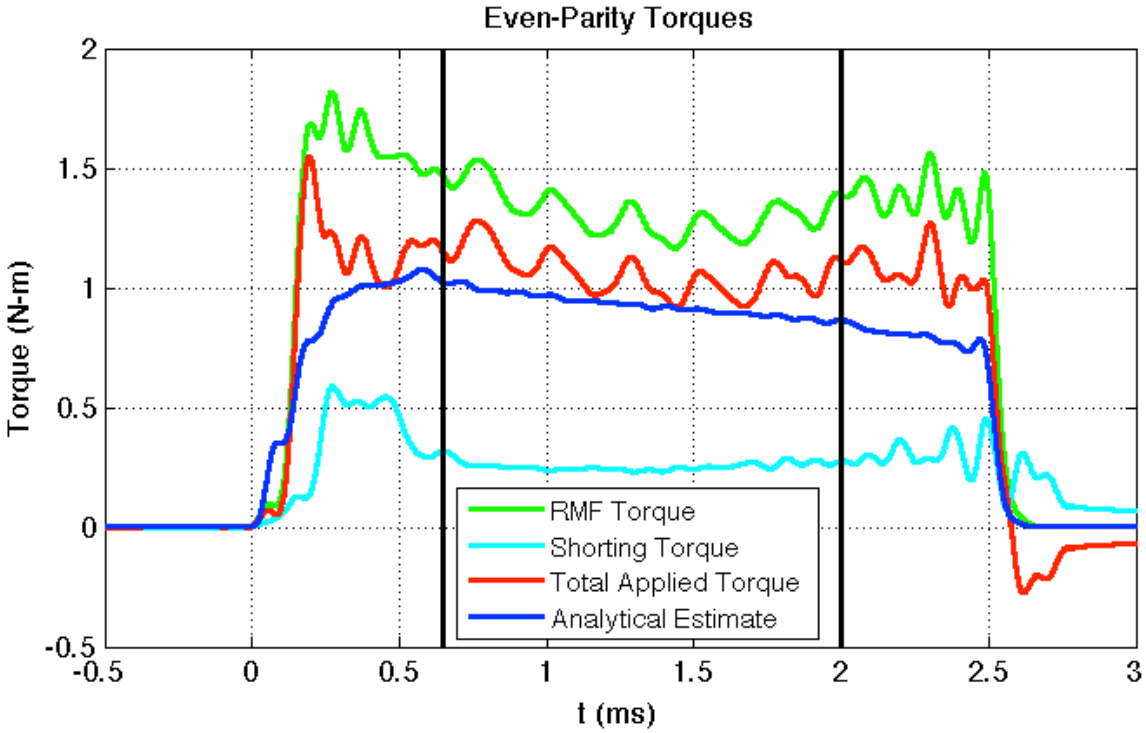

Figure 8.8: RMF torque, shorting torque, total torque, and a comparison to the 2D analytical torque model for Even-Parity RMF driven FRC

The analytical torque estimate (*equation 8.2*) uses the experimental value of B_ω that is calculated using the current measured in the RMF antenna and calibrated to the geometry of the even-parity RMF. The structure of the odd-parity RMF is sufficiently complex that we do not have an analytical estimate of the torque for the odd-parity configuration. The calculation using the three-axis probe data is the first estimate of the odd-parity torque.

The odd-parity torque balance is shown in *figure 8.9*. The odd-parity configuration provides a smaller RMF torque than in even-parity with a comparable shorting torque. The resulting total applied torque is approximately 0.6 N-m and is 60% of the applied torque for even-parity RMF.

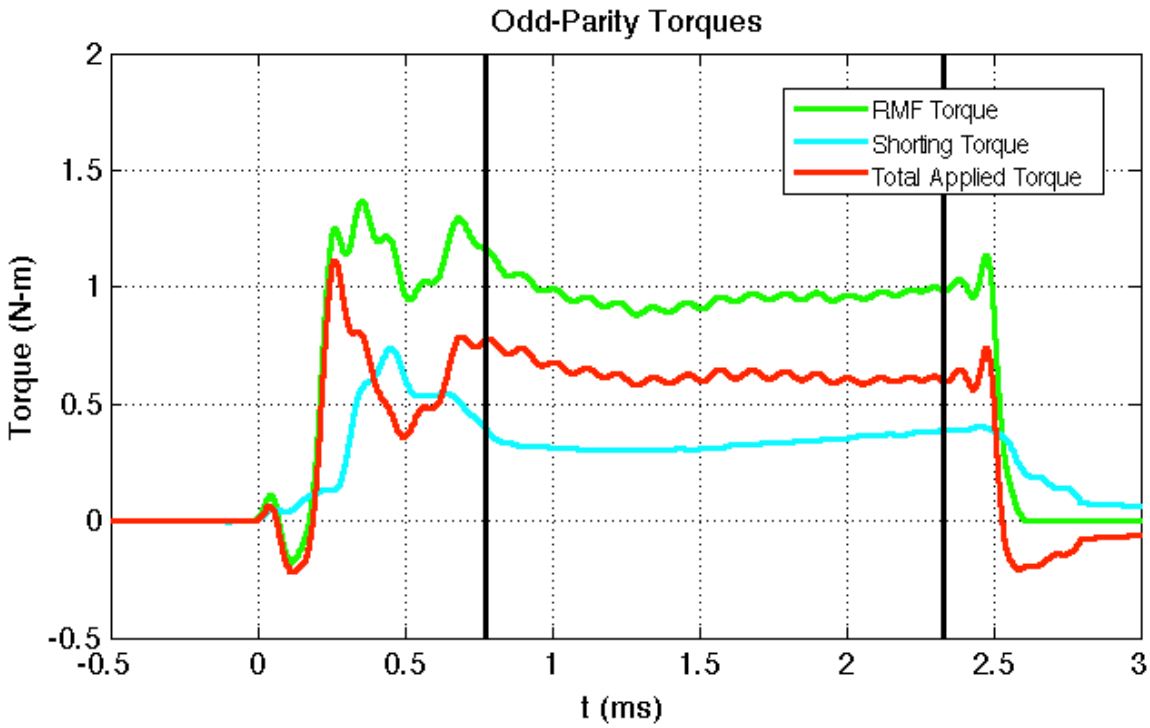

Figure 8.9: Odd-parity torques with the quiescent period marked by black lines.

Section 8.5: Even-parity torque density maps

The total integrated torque gives a picture of how the RMF acts on the bulk FRC but we can look at the r-z map of the torque density to see details of the momentum flowing through in the system. We map the magnetic torque transmitted radially and axially due to the RMF and low-frequency magnetic field components. For reference, the flux contours calculated using the average-field data are included to show the general shape of the FRC.

The RMF torque is generated under the RMF antennas that extend from -0.6 m to +0.6 m. The radial momentum flow created by the RMF is shown in *figure 8.10;* it is concentrated outside the separatrix and quickly falls off as torque is either applied to the electrons, transferred to a torque on the average field, or dissipated elsewhere. The RMF momentum flowing radially into the FRC is the driving torque and is positive.

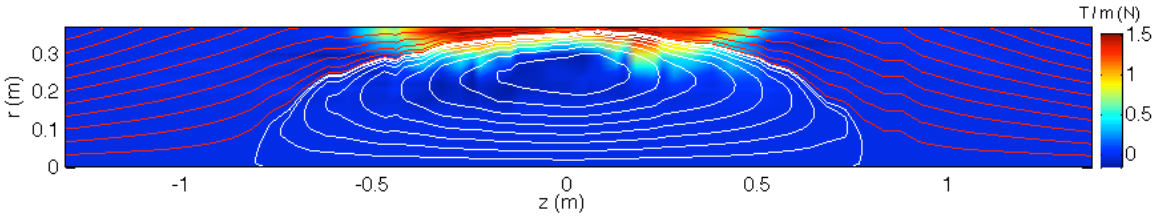

Figure 8.10: Even-parity radially transmitted RMF torque density at 1.0 ms

Figure 8.11 shows the portion of the RMF momentum that is flowing in the axial direction, away from the midplane. A positive axial flow (red) points to the right and a negative axial flow (blue) points to the left. The axial momentum flow contributes to the twisting of the open field lines.

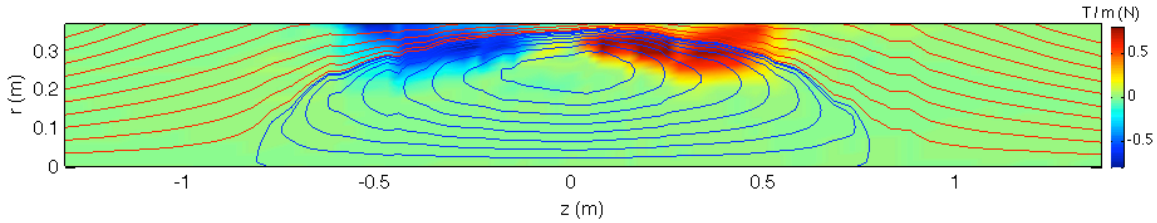

Figure 8.11: Even-parity axially transmitted RMF torque density at 1.0 ms

Combining the axial and radial torque densities yields an r-z map of the RMF momentum flow which is shown in *figure 8.12*. The RMF momentum flows inward from under the antennas; the torque is deposited where the flow of momentum changes. The majority of the RMF torque is deposited within the outer field lines of the FRC but some is applied to the open field lines.

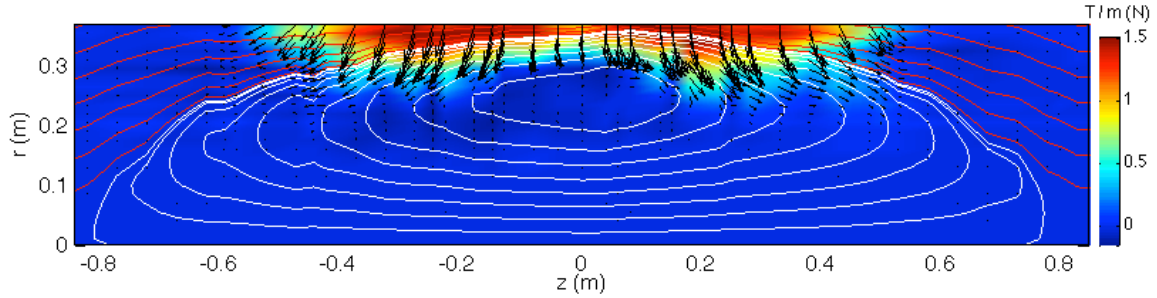

Figure 8.12: Even-parity RMF torque flow map at 1.0 ms

The radially transmitted torque density due to the average magnetic field is shown in *figure 8.13*. Some of the RMF torque transmitted radially gets transferred to a torque on the axisymmetric portion of the inner field lines.

In the open field line region we see a torque transmitted across the radial wall that increases with distance from the midplane. This increase could be due to magnetic fields generated by currents in the metal section and contributes to the twisting of the magnetic field lines in the open field line region. However, this effect is beyond the ends of the control volume and our analysis focuses on the mean-field torque activity inside the FRC.

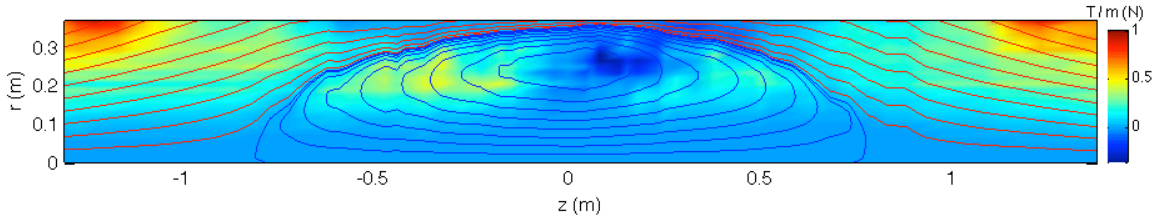

Figure 8.13: Even-parity mean-field torque density transmitted radially at 1.0 ms

The mean-field axial momentum flow, shown in *figure 8.14*, along the open field lines is attributed to the shorting torque and is in the opposite direction of the RMF applied torque. This also increases with distance from the x-point. However, the contribution of the shorting torque to the FRC torque balance is taken from the measurement of the shorting torque flowing through the ends of the control volume which are just outside the x-point of the FRC. The axial increase of the shorting torque does not change the FRC torque balance.

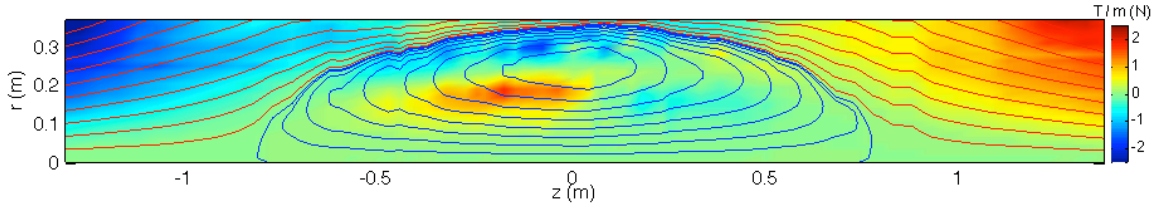

Figure 8.14: Even-parity mean-field transmitted axially torque density at 1.0 ms

The radial and axial mean-field torque transmission vectors are plotted with the axially transmitted torque in *figure 8.15*. On the outer field lines, the momentum flows away from the midplane before circling back toward the midplane on the inner field lines. The torque is transferred to the inner field line region and is deposited near the midplane.

This is a mechanism for current drive on the inner field lines. The asymmetry in the torque density matches the asymmetry in the B_θ measurements.

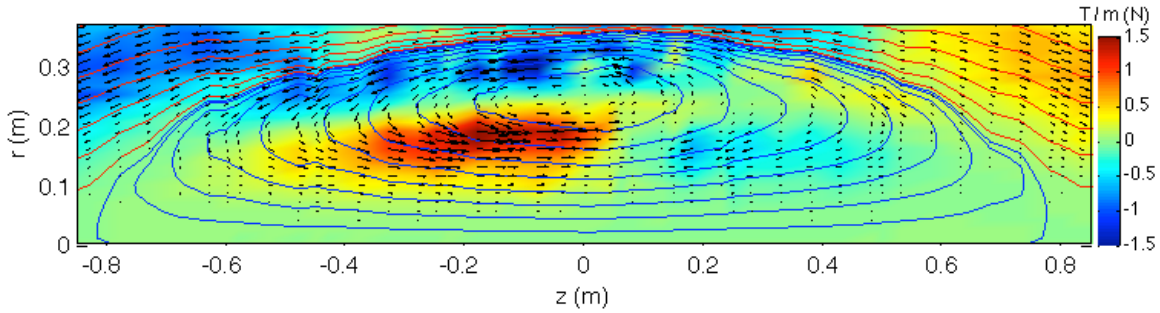

Figure 8.15: Even-parity mean-field torque vectors.

Combining the data from the RMF and mean-field components shows the overall momentum flow pattern in the FRC. A portion of the momentum flowing in under the RMF antenna is diverted to the open field lines and is lost out the ends of the control volume. Most of the RMF torque is deposited on the outer field lines but some momentum flows into the FRC, around the midplane from the outer to the inner field lines, and is deposited inside the field null to drive current on the inner field lines.

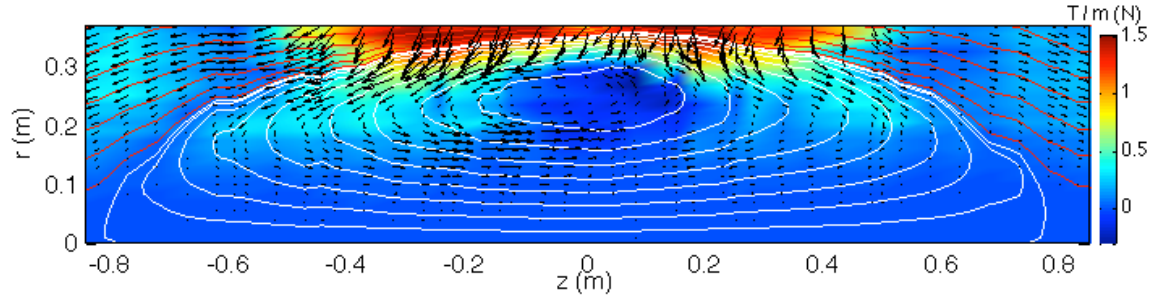

Figure 8.16: Even-parity RMF + mean-field torque density map at 1.0 ms

The RMF torque is transferred to a mean-field torque on the inner field lines. The radial distribution of the torques quantifies the torque transfer. The radially transmitted torque integrated axially along the extent of the FRC, shown as a function of radius in *figure 8.17*, demonstrates the growth of the mean-field torque (blue) as the RMF torque (black) is deposited in the FRC. The shorting torque (green) is integrated from 0 to r and

is the torque transmitted through the end-wall of a cylindrical control volume of radius r, length l_s. The total (magenta) shows the torque transferred through the wall of a cylinder of radius r, length l_s.

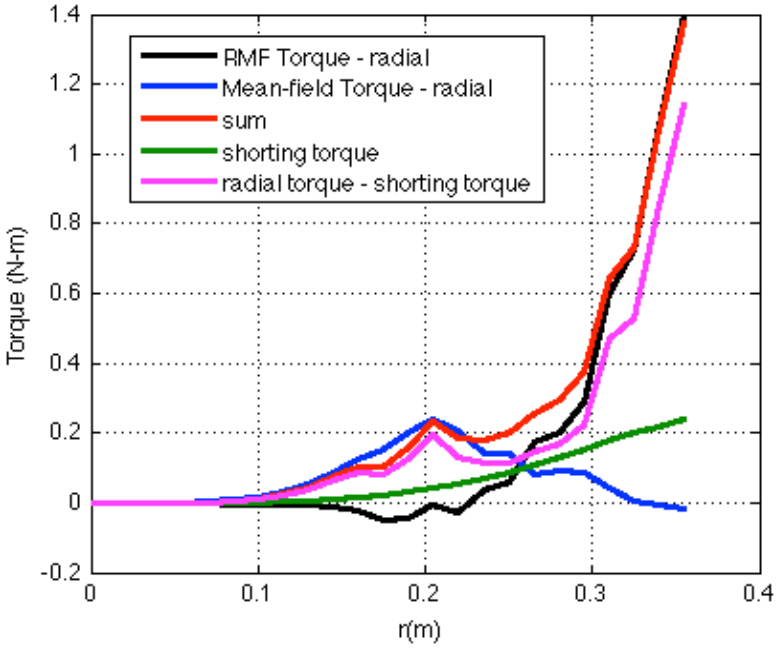

Figure 8.17: Even-parity torques as a function of radius

Section 8.6: Odd-parity torque density maps

The odd-parity radially transmitted RMF torque in *figure 8.18* exhibits similar behavior to the even-parity configuration but the torque drops to zero at the midplane where the RMF is in the z-direction. The torque goes negative near the field null on either side of the axial midplane meaning that it is pointing out radially.

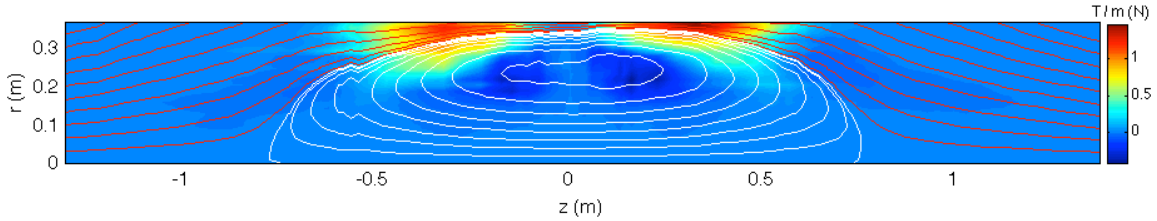

Figure 8.18: Odd-parity radially transmitted RMF torque density at 1.0 ms

The axially transmitted torque, shown in *figure 8.19*, has a four-lobed structure similar to what we saw in the plots of the average odd-parity B_θ in *figure 5.14*. On the outer field lines there is a small torque flowing away from the midplane but there is flow toward the midplane just inside the field null radius. On the open field lines, there is a small torque flow toward the midplane, opposite of what was measured in the even-parity driven FRC.

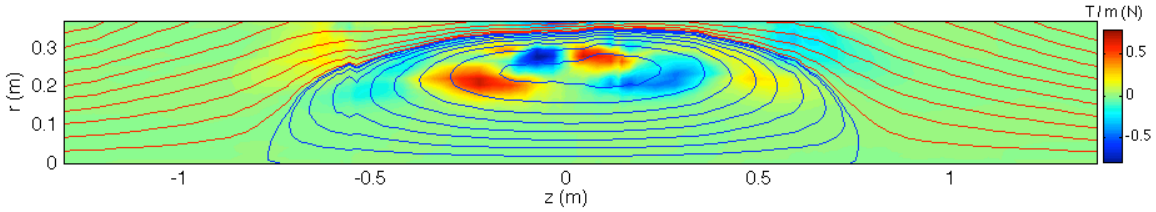

Figure 8.19: odd-parity axially transmitted RMF torque density at 1.0 ms

As in even-parity, the RMF torque quickly drops to zero outside the RMF antennas so the RMF torque flow in *figure 8.20* is confined to the FRC. It is clear that the radial flow is much larger than the axial torque flow. The torque flows radially inward and is deposited to the outer field lines. It appears that a small circulating flow deposits some torque on either side of the magnetic null.

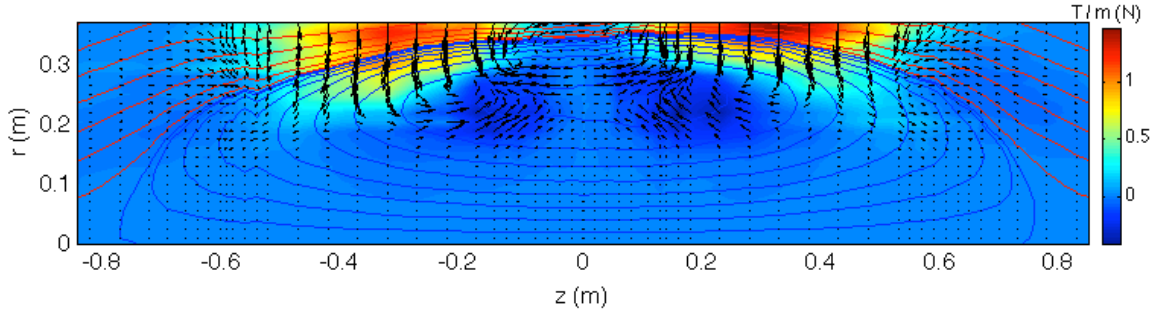

Figure 8.20: Odd-parity RMF torque flow at 1.0 ms. The color is the radially transmitted torque.

In the case of even-parity antennas the axial RMF flow was away from midplane at the ends of the FRC but in this case, the axial flow of the RMF torque at +/- 0.6 m is toward the FRC. However, as in the even-parity case, part of the RMF torque is applied to the open field lines and a portion transferred to the mean-field torque on the inner field lines of the FRC.

Figure 8.21 shows the odd-parity the mean-field radially transmitted torque; within the FRC the torque concentrated around the center of each antenna at +/- 0.3 m. As in even-parity, there is a large torque past 1 m transmitted through the radial boundary.

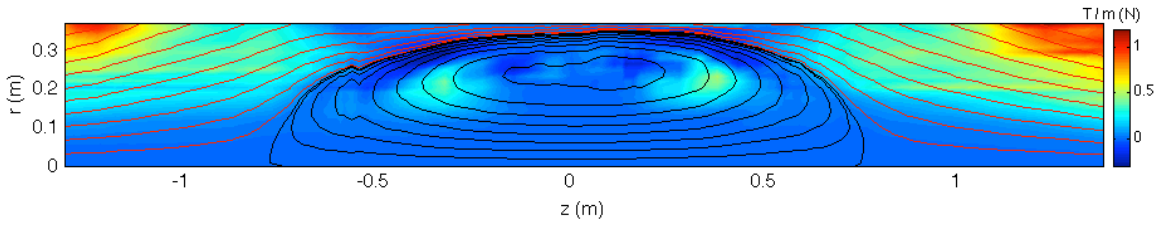

Figure 8.21: Odd-parity mean-field torque transmitted radially at 1.0 ms

There is also a large torque on the open field lines transmitted axially, seen in the open field line region in *figure 8.22*. Again, the structure of the torque inside the FRC matches the measurement of B_θ.

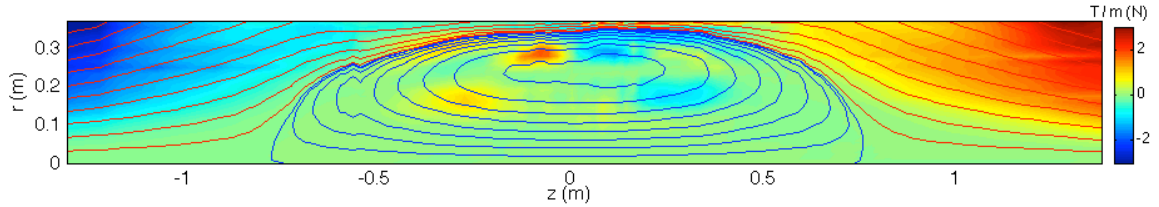

Figure 8.22: Odd-parity mean-field torque transmitted axially at 1.0 ms

The torque vectors in *figure 8.23* shows the mean-field torque being deposited on either side of the midplane on the inner field lines, outer field lines, and at the separatrix.

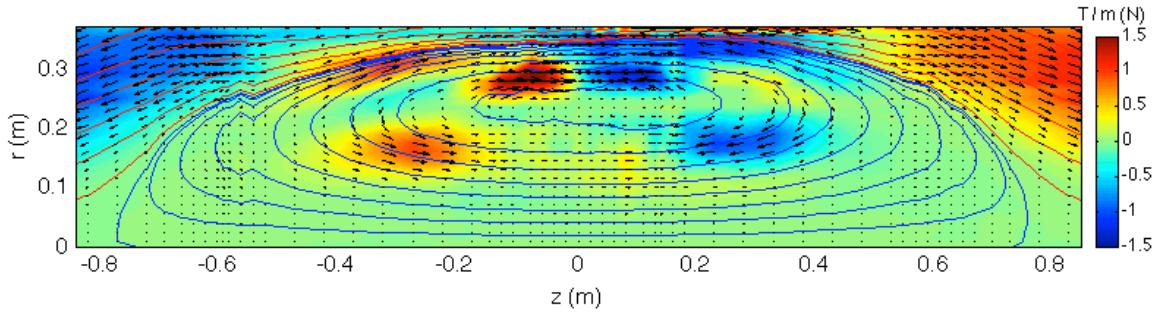

Figure 8.23: Axially transmitted mean-field odd-parity torque with axial/radial torque vectors at 1.0 ms

The total momentum flow vector map for odd-parity drive in *figure 8.24* shows similar behavior as in the even-parity case. While most of the momentum flows inward toward the FRC, there is a flow directed away from the midplane associated with the shorting torque. The pattern within the FRC shows the momentum flowing toward the midplane with activity on the inner field lines showing a portion of the momentum flowing up toward the field null radius.

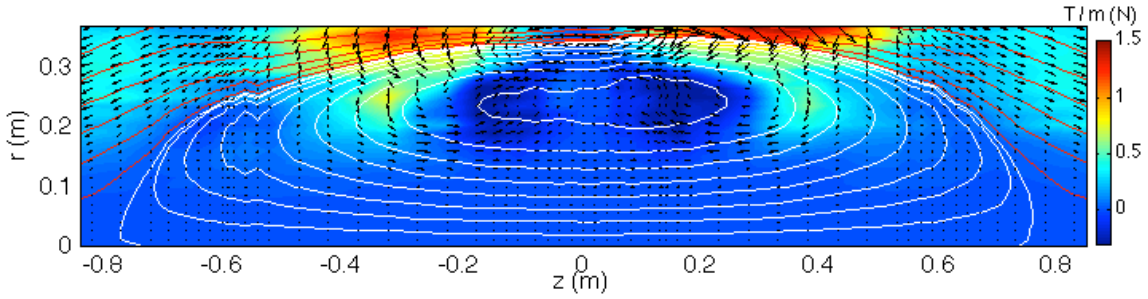

Figure 8.24: RMF + mean-field torque density with momentum flow vectors

The radial profiles of the torque for odd-parity show similar behavior as in even-parity. However, within r = 0.28, the curve of the total torque (radial – shorting) is flat at zero. Within r = 0.28, there is little net momentum flow.

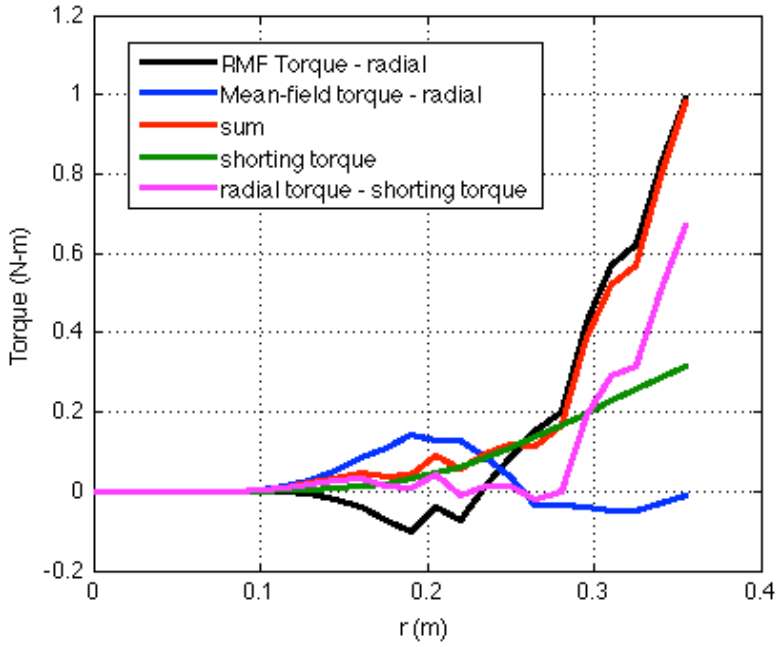

Figure 8.25: Odd-parity torques as a function of radius

Using the radial and axial torque flow data we can see the full picture of how the torque is transmitted through the system. Most of the RMF torque is deposited on the outer field lines of the FRC; some RMF torque is converted to a mean-field torque that is deposited on the inner field lines; some of the RMF torque is lost to the open field lines. The odd-parity RMF configuration has more efficient current drive than the even-parity RMF configuration.

Section 8.7: Resistivity estimate

We can estimate the average cross-field resistivity by comparing the 3D torque calculations to the resistive torque estimate from the 2D model given in *equation 8.3*. Previous estimates of the resistivity based on the analytical model yielded an average cross-field resistivity of 75 μΩ-m for the FRCs driven with the even-parity RMF antenna configuration. Using the data from the even-parity three-axis probe scan we calculate the resistivity based on the analytical model and see an average resistivity of about 70 μΩ-m, which agrees with previous estimates. Replacing the analytical estimate of the RMF

torque with our more detailed torque measurements gives a resistivity that agrees with the analytical model. Remember that the analytical model underestimated the RMF torque measured by the probe but was a close approximation to the total applied torque. *Figure 8.26* shows the average cross field resistivity as a function of time for the quiescent period of the even-parity RMF driven FRC compared to the analytical estimate to the results using the probe data.

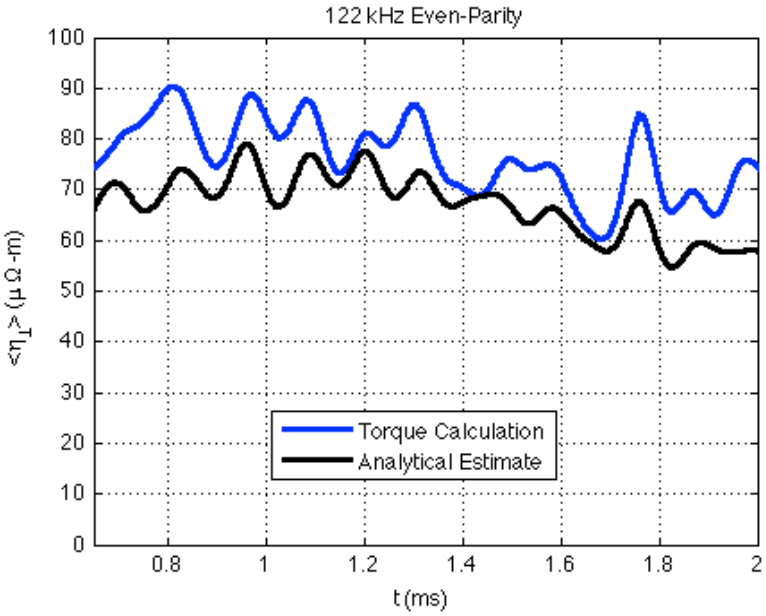

Figure 8.26: Resistivity for even-parity compared to analytical model approximation

The analytical estimate of the resistivity does not apply to the odd-parity case. Using the three-axis probe and the torque model we have an estimate of the average resistivity for odd-parity RMF drive. The resistivity is shown as a function of time for the quiescent period of the FRC in *figure 8.27*. As in the even-parity case, the total applied torque is compared to the equation for resistive torque used in the analytical model.

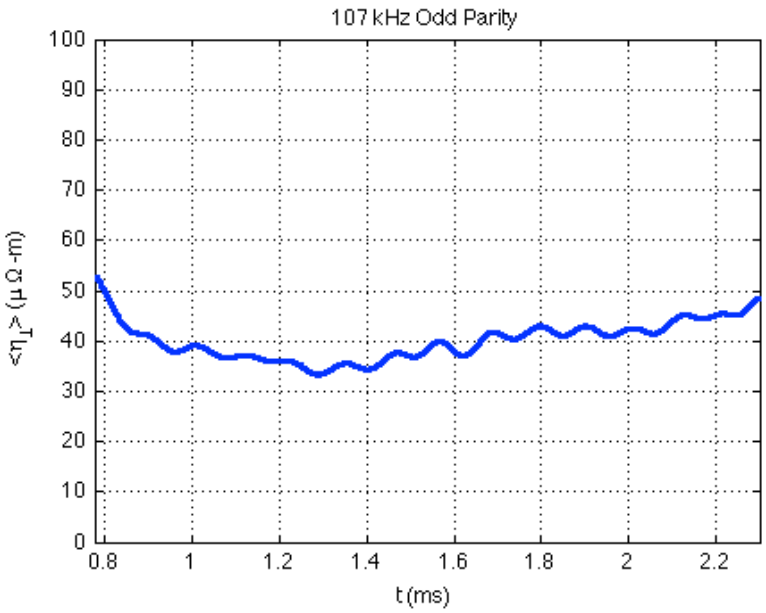

Figure 8.27: Resistivity as a function of time for odd-parity RMF

The average resistivity in the odd-parity driven FRC is 40 μΩ-m, approximately half of the resistivity measured in the even-parity case.

Chapter 9: **SUMMARY AND CONCLUSIONS**

The simple closed geometry of an FRC makes it an attractive mechanism for fusion energy. An FRC quickly decays unless the poloidal flux is externally maintained. A transverse rotating magnetic field (RMF) has been shown to sustain an FRC for as long as the RMF is powered. The RMF drives a steady electron current through a $\langle v_z \times B_r \rangle$ Lorentz force and puts a net torque on the electrons in an FRC. The torque applied by the RMF is transferred to the ions through election-ion collisions. However, the spin-up of the ions is limited and a resistive torque balances the applied torque to create a steady state poloidal flux.

The RMF current drive opens the closed flux surfaces of an FRC making it difficult to achieve high electron temperatures. A second RMF configuration called odd-parity, where the sign of the rotating field flips across the midplane, has the potential to maintain closed flux surfaces. The odd-parity configuration was briefly studied in TCS.

The physics of RMF current drive has been described using an analytical model that does not account for axial variation or end effects of the RMF antennas. This model, however, provides the framework for our understanding of current drive, accounting for RMF antenna effects as well as plasma behavior in the open field line region.

A fully translatable three-axis magnetic probe was installed on TCSU to measure all three magnetic field components in the r-z plane in the open field line region and along the entire length of the FRC. The three-axis probe was absolutely calibrated in conjunction with external flux loops, axial B_z probes, and a two-axis midplane internal magnetic probe. The magnetic diagnostics were used with the interferometer and other TCSU diagnostics to find a baseline stable, repeatable FRC for each RMF configuration. Scans were made by moving the three-axis probe 5 cm or less between shots that matched the baseline. As shown in *figure 5.1*, the overall plasma parameters for the even- and odd-parity FRCs were similar, highlighting the underlying differences in the magnetic structure and current drive physics.

Measurements of the magnetic field in the r-z plane confirmed, for the first time, the steady toroidal field inside the FRC that flips sign across the midplane. The internal toroidal field indicates the presence of a circulating current flowing radially inward at the

midplane and circling around the ends of the FRC. This circulating current aids in current drive on the inner field lines.

To understand 3D effects, we extrapolate the data in the r-z plane azimuthally focusing on the mean-field data and data at the RMF frequency. The mean-field data is azimuthally symmetric while the RMF data has a simple sinusoidal dependence in θ. Combining the extrapolated data from each position we form a 3D picture of the magnetic field streamlines. Many streamlines which pass through the even-parity driven FRC exhibit an s-shaped orbit; the field lines pass through the quartz vacuum boundary, wrap around the end of the FRC, travel down the machine axis, and wrap around the other end of the FRC before exiting under the quartz wall. These s-shaped field lines rotate with the RMF frequency. The short field lines preclude the possibility of good electron energy confinement. The 3D reconstruction of the field lines also revealed many field lines which pass under the RMF antenna and through the ends of the probe domain, making contact with a conducting boundary. The RMF twists these field lines, affecting the plasma behavior in the jet.

The three-axis probe data was used to directly measure the torque on the FRC. The majority of the RMF torque is applied to the FRC to drive the electron current. A portion of the RMF torque is applied to the open field lines, which twist to create a steady state toroidal field in the open field line region. Approximately 20% of the RMF torque is applied to the open field lines instead of driving current in the FRC. The total torque applied to the FRC is the RMF torque reduced by the torque lost to the open field lines. The analytic torque model underestimates the RMF torque but it was found to be a close approximation of the total torque applied to the even-parity driven FRC. This result validates the conclusions of previous analysis that used the analytical model.

The r-z maps of the torque density presented in *chapter 8* highlight the transfer of RMF torque to the mean-field torque, especially on the inner field lines of the FRC. The RMF does not penetrate past the field null but a portion of the RMF torque is transferred to a mean-field torque which aids in current drive on the inner field lines. A slowly rotating structure, just inside the field null, aids in the current drive on the inner field lines. The details of this mechanism are complicated but it appears that electrons rotating at 30 – 35 kHz assist in the transfer of RMF torque from the outer field lines to a mean-

field torque on the inner field lines. This activity is present in both even- and odd-parity RMF configurations.

The odd-parity RMF driven FRC exhibits four-lobed internal toroidal field structure indicating a more complicated electron current pattern. The 3D magnetic field structure does not show the short s-shaped field lines seen in the even-parity case but clearly shows field lines that execute multiple transits of the FRC before exiting the domain. As in the even-parity case, there are multiple field lines that extend between the RMF antenna and the conducting boundary. The amount of RMF torque lost to the open field line region is approximately the same in the even- and odd-parity configurations. However, odd-parity delivered approximately 20% less RMF torque. The total torque applied by the odd-parity RMF configuration was 60% of the torque applied in the even-parity case. The plasma parameters were similar so the difference in torque implies that the resistivity is lower in the odd-parity case. Balancing the total applied torque with an estimate of the resistive torque yields a resistivity of approximately 75 μΩ-m for even-parity and 35 μΩ-m for odd-parity.

The odd-parity configuration generates an FRC with longer field lines than in even-parity and affirms the possibility of maintaining closed flux surfaces with a large B_e/B_ω ratio. Using a smaller applied torque and lower antenna current, odd-parity RMF achieves similar plasma parameters as the even-parity case.

The work done with the translatable three-axis magnetic probe has greatly expanded our understanding of both even- and odd-parity RMF driven FRCs.

BIBLIOGRAPHY

[1] M. Tuszewski, *Field Reversed Configurations,* Nucl. Fusion 28, 2033, 1988

[2] L. C. Steinhauer, *Review of field-reversed configurations*, Phys. Plasmas **18**, 070501 (2011)

[3] K.E. Miller, et. al., *The TCS upgrade: Design, construction, conditions, and enhanced RMF FRC performance,* Fusion Science and Technology, **54**, 948 (2008)

[4] H. A. Blevin and P. C. Thonemann, *Plasma confinement using an alternating magnetic field,* Nucl. Fusion Suppl. Part I 55 (1962)

[5] I. R. Jones, *A review of rotating magnetic field current drive and the operation of the rotamak as a field-reversed configuration (Rotamak-FRC) and a spherical tokamak (Rotamak-ST),* Phys Plasmas **6**, 1950 (1999)

[6] S. A. Cohen and R. D. Milroy, *Maintaining the closed magnetic-field-line topology of a field-reversed configuration with the addition of static transverse magnetic fields*, Phys. Plasmas **7**, 2539 (2000)

[7] I. R. Jones and W. N. Hugrass, *Steady-state solutions for the penetration of a rotating magnetic field into a plasma column*, Journal of Plasma Physics **26**, 441 (1981).

[8] W. N. Hugrass, *The Influence of the Spatial Harmonics on the Rotating Magnetic Field Current Drive*, Australian Journal of Physics **39**, 513 (1986).

[9] P. Watterson, *Analytical solutions for the current driven by a rotating magnetic field in a spherical plasma*, Journal of Plasma Physics **46**, 271 (1991)

[10] A.L. Hoffman, *Rotating magnetic field current drive of FRCs subject to equilibrium constraints,* Nucl Fusion **40**, 1523, (2000)

[11] H.Y. Guo, A. L. Hoffman, and R.D. Milroy, *Rotating magnetic field current drive of high-temperature field reversed configurations with high zeta scaling,* Phys. Plasmas **14**, 112502 (2007)

[12] H.Y. Guo and A. L. Hoffman, *Sustainment of elongated field reversed configurations with localized rotating magnetic field current drive,* Phys. Plasmas **11**, 1087 (2004)

[13] L. C. Steinhauer, *End-shorting and electric field in edge plasmas with application to field-reversed configurations,* Phys. Plasmas **9**, 3851 (2002)

[14] A.I.D. Macnab, R.D. Milroy, C.C. Kim, and C.R. Sovinec*, Hall magnetohydrodynamics simulations of end-shorting induced rotation in field-reversed configurations,* Phys Plasmas **14**, 092503 (2007)

[15] C. L. Deards, A. L. Hoffman, and L. C. Steinhauer, *Measurements accounting for the impediment of ion spin-ip in rotating magnetic field driven field reversed configurations*, Phys. Plasmas, **18**, 112511 (2011)

[16] D. D. Ryutov, J. Kesner, M. E. Mauel, *Magnetic field perturbations in closed-flield-line systems with zero toroidal magnetic field*, Phys. Plasmas **11**, 2318 (2004)

[17] H. Y. Guo, A. L. Hofman, and L. C. Steinhauer, *Oberservations of improved conginement in field reversed configurations sustained by antisymmetric rotating magnetic fields*, Phys. Plasmas **12**, 062507 (2005)

[18] C.R. Sovinec, et al., *Nonlinear magnetohydrodynamics simulation using high-order finite elements*, J. Comp. Phys. 195, 355 (2004)

[19] R.D. Milroy, C.C. Kim, and C.R. Sovinec, *Extended magnetohydrodynamic simulations of field reversed configuration formation and sustainment with rotating magnetic field current drive,* Phys. Plasmas, **17**, 062502 (2010)).

[20] R. D. Milroy, *A comparison of NIMROD simulations of RMF current drive with 3-axis probe data from the TCSU experiment*, ICC conference proceedings, August, 2011, Seattle, WA http://iccworkshops.org/icc2011/proceedings.php

[21] I.H. Hutchinson, *Principles of Plasma Diagnostics 2nd Edition,* Cambridge University Press, 2002

[22] M. Tuszewski, *Excluded flux analysis of a field-reversed plasma*, Physics of Fluids, **24**, 2126 (1981)

[23] K.E. Miller, K.M. Velas, D.E. Lotz, *Miniature Magnetic Field Probes For Use in High Temperature Plasmas*, APS-DPP 2009 Poster, Atlanta, GA

[24] K.M. Velas*,* J.A. Grossnickle, A.L. Hoffman, K.E. Miller, R.D. Milroy, *Internal magnetic field measurements in the TCSU RMF current drive experiment,* J. Fusion Energy **29**, 580-583 (2010).

[25] R. D. Milroy and K. E. Miller, *Edge-drive rotating magnetic field current drive of field-reversed configurations*, Phys. Plasmas **11** 633 (2004)

[26] Oppenheim, Alan V., Robald W. Schafer, with John R. Buck. *Discrete-Time Signal Processing 2nd Edition*,. New Jersey: Prentice-Hall Inc., 1999. Page 796

[27] R. D. Milroy, *A magnetohydrodynamic model of rotating magnetic field current drive in a field-reversed configuration*, Phys. Plasmas **7**, 4135 (2000)

[28] C. L. Deards, *Factors affecting ion spin-up in the translation, confinement, and sustainment upgrade experiment,* PhD. Thesis, 2010